OPTIMAL RADAR WAVEFORM DESIGN FOR IMPROVED TARGET RANGE RESOLUTION AND TRACKING PERFORMANCE IN A COOPERATIVE RADAR-COMMUNICATION SYSTEM

Thesis

Submitted in partial fulfillment of the requirements for the degree of

DOCTOR OF PHILOSOPHY

by

ASHOKA CHAKRAVARTHI M

DEPARTMENT OF ELECTRONICS AND COMMUNICATION ENGINEERING

NATIONAL INSTITUTE OF TECHNOLOGY KARNATAKA,

SURATHKAL, MANGALORE - 575025

MARCH 2024

Life changing quotes

Be humble. Don't forget where you started from, even if you are a professional in your field.
– Sri. Mahipathi Venkateswarlu

Across professions, consistency is a direct product of work ethic.
– Harsha Bhogle

DECLARATION

by the Ph.D. Research Scholar

I hereby declare that the Research Thesis entitled **OPTIMAL RADAR WAVEFORM DESIGN FOR IMPROVED TARGET RANGE RESOLUTION AND TRACKING PERFORMANCE IN A COOPERATIVE RADAR-COMMUNICATION SYSTEM** which is being submitted to the **National Institute of Technology Karnataka, Surathkal** in partial fulfillment of the requirements for the award of the Degree of **Doctor of Philosophy** in **Electronics and Communication Engineering** is a *bonafide report of the research work carried out by me.* The material contained in this Research Thesis has not been submitted to any University or Institution for the award of any degree.

(187EC002, Ashoka Chakravarthi M)

Department of Electronics and Communication Engineering

Place: NITK, Surathkal.

Date: 27-03-2024

CERTIFICATE

This is to *certify* that the Research Thesis entitled **OPTIMAL RADAR WAVEFORM DESIGN FOR IMPROVED TARGET RANGE RESOLUTION AND TRACKING PERFORMANCE IN A COOPERATIVE RADAR-COMMUNICATION SYSTEM** submitted by **ASHOKA CHAKRAVARTHI M**, (Register Number: 187EC002) as the record of the research work carried out by him is *accepted as the Research Thesis submission* in partial fulfillment of the requirements for the award of the degree of **Doctor of Philosophy**.

27/03/2024

Prof. John D'Souza

Research Guide

Dr.Pathipati Srihari

Research Guide

Prof. Neelawar Shekar Vittal Shet

Chairman - DRPC

Acknowledgment

My Ph.D. study involved many people in its journey. Foremost I would like to express my sincere gratitude to my research guides **Dr. John D'Souza**, Professor, Department of Electronics and Communication Engineering (ECE) and **Dr. Pathipati Srihari**, Associate Professor, Department of Electronics and Communication Engineering (ECE), NITK, Surathkal, allowed me to pursue Ph.D. I greatly acknowledge their invaluable guidance, support, and encouragement received throughout my research work. I deeply realize that for me, they are not only research guides who always reminds me to keep on the right track but also people with kind hearts and humanity.

I sincerely thank my Research Progress Assessment Committee (RPAC) members **Prof. Ashvini Chaturvedi**, Professor and Former Head of the Department, ECE, and **Dr. Srinivasarao Kola**, Associate Professor in the Department of MACS, for their invaluable suggestions and constant encouragement to improve my research work.

I sincerely thank the Doctoral Thesis Assessment Committee (DTAC) Members **Dr. Raghavendra B.S.**, ECE Dept, and **Prof. Lakshman Nandagiri**, WROE Dept, NITK for your valuable suggestions. My special thanks to **Dr. Nithin V. George**, Dept. of Electrical Engineering, IIT Gandhinagar, Indian Referee for making his time and conducting the viva voce examination in the offline mode.

I sincerely thank **Prof. Neelawar Shekar Vittal Shet**, Professor and Head of the Department (HOD), ECE, **Prof. T. Laxminidhi**, Professor and Former HOD, ECE, **Prof. U. Shripathi Acharya**, Professor, Former HOD, ECE, **Prof. Muralidhar Kulkarni**, Former Professor, Department of ECE, **Dr. Prashantha Kumar H.**, Associate Professor, Department of ECE, and **Dr. Prabhu K**, Associate Professor, Department of ECE for their technical and moral support during my

research work. I extend my sincere thanks to the teaching faculty of the Department, ECE for their support during my study.

My appreciation goes to all my current and former research group members **Dr. Bethi Pardhasaradhi**, **Dr. Gunnery Srinath**, **Dr. Purushottama T. L.**, **Mr. Bobbili Naga Balarama Reddy**, **Mrs. Kumuda D K**, **Mrs. Aswitha K Shetty**, **Mrs. Achala. G** and my co-scholars **Mr. Mahesh Kumar T.N.**, **Shajahan Abbobacker**, **Mr. Pokala Sudhakar Reddy**, **Mr. P. Venkateswarlu** for their stimulated discussion throughout my stay at NITK. Further, I extend my sincere thanks to all teaching staff and non-teaching staff of the Department of ECE for their support during my research work.

Finally I express heartfelt thanks and deepest appreciation to my life partner **Mrs. Mahipathi Bharathi**, my lovely little boy **Sri Karthikeya**, my proud parents **Sri. Mahipathi Venkateswarlu**, **Smt. Mahipathi Ravi Kumari**, my beloved brother **Mr. Mahipathi Naga Phanindra Kumar**, my sister-in-law **Mrs. Mahipathi Vijaya Sree**, and kids **Joshvika Sree and Sithara**, my sweetest sister **Mrs. Byra Siva Nagalakshmi**, my brother-in-law **Mr. Byra Rajasekhar** and my nephew **Byra Darahas** for their love, support, and encouragement to carry out my research work.

I firmly believe that without family members, surely, this research work would not have been possible. I also thank my well-wishers, who directly or indirectly are the reason behind my decision to take a different path rather than a job.

Place: Surathkal Ashoka Chakravarthi M

Date:

Abstract

The widespread usage of the Radio Frequency (RF) spectrum for wireless and mobile communication systems generated a significant spectrum scarcity. To tackle this issue, the spectral cooperation between radar-sensing and communication systems research has received a surge of interest in recent times. The Cooperative Radar-Communication System (CRCS) provides a framework to simultaneously utilize the allocated radar spectrum for both sensing and communication purposes. In addition, waveform design plays a vital role in the development of various configurations of a CRCS.

Based on the literature survey, most approaches used to design a radar waveform are locally optimum. In addition, designing a globally optimized radar waveform for a cooperative scenario has been a challenging task for accomplishing the convergence of radar-sensing and communication functionalities without degrading the performance at either end. To overcome this challenge, the first objective of this research investigation proposes a novel global optimization-based Spatial Branch and Bound (SBnB) approach to optimize the phase coefficients of a Non-Linear Frequency Modulated (NLFM) radar waveform in a CRCS framework. The simulation results reveal that the proposed SBnB radar waveform design approach provides improved performance compared to the existing radar waveform design approaches.

Further, the state estimation-based optimal radar waveform design for improving tracking performance is hardly reported in the CRCS framework. Thus, the second objective of this research work proposes a novel measurement model, based on communication residual components for various waveforms, using the Fisher Information Matrix (FIM) to evaluate the radar system performance in the CRCS framework. The radar waveforms considered in this investigation are rectangular pulse, triangular pulse, Gaussian pulse, Linear Frequency Modulated (LFM) pulse, LFM-Gaussian pulse, and Non-Linear Frequency Modulated (NLFM) pulse. Thereafter, the Kalman filter is deployed to estimate the target kinematics (range and range rate) of a single linearly moving target for the aforementioned radar waveforms. In the simulated results, the range and range rate estimation errors are quantified by the Root Mean

Square Error (RMSE) and they are validated with the Posterior Cramer-Rao Lower Bound (PCRLB).

Furthermore, another contribution reported in this thesis is to exploit the communication waveform along with the radar waveform to improve the target state estimation performance in a CRCS. An LFM pulse radar waveform, an NLFM pulse radar waveform, and a Quadrature Amplitude Modulated (QAM) communication waveform are considered for this investigation and analyzed the target state estimation performance. At a given epoch, the target position is estimated by considering the range and range rate as a measurement in an Iterative Least Squares (ILS) framework. After that, the Kalman Filter (KF) estimates the target dynamics by taking the output of the ILS as a measurement model. Besides, the target estimated position is quantified with the RMSE and they are validated with the PCRLB.

Overall the results attained in this research work signify the importance of radar waveform optimization in a CRCS. In addition, the superiority of the optimized NLFM radar waveform is very well exhibited in terms of range resolution, radar estimation rate, and target state estimation performance. Moreover, the major contributions done in this thesis added profound knowledge in the radar waveform optimization, and target tracking areas.

Contents

List of Figures vii

List of Tables xi

Abbreviations and Nomenclature xiii

1 Introduction 1

1.1 Background 1

1.1.1 Evolution of Cooperative Radar-Communication System (CRCS) 3

1.1.2 Applications of Joint Radar-Sensing and Communication . . . 5

1.2 Literature Survey 8

1.2.1 Waveform Design for a CRCS 8

1.2.2 Radar Sensor-Centric Approaches 9

1.2.3 Target Tracking 10

1.2.4 Waveform Design for Target Tracking 11

1.3 Motivation 12

1.4 Research Objectives 13

1.5 Proposed Methodology for Each Identified Research Objective 13

1.5.1 Constraint-based Radar Waveform Optimization 13

1.5.2 Optimal Waveform Selection for Target State Estimation . . . 14

1.5.3 Communication-aided Radar Target State Estimation 14

1.6 Contribution of the Thesis 15

1.7 Overview 15

2 Constrained Radar Waveform Optimization for a CRCS 17

2.1 Problem Formulation 17

2.1.1 NLFM Radar Waveform Optimization 20
2.2 Radar Waveform Design Approaches for a CRCS 22
2.2.1 MEEV Approach 22
2.2.2 PRC-CRLB Approach 23
2.2.3 M-PRC-CRLB Approach 23
2.2.4 SBnB Approach 23
2.2.5 Energy Constraint 27
2.3 Significance of Various Performance Metrics in Optimum Waveform Design 27
2.3.1 Threshold SNR 27
2.3.2 NLFM Phase Polynomial Order 28
2.3.3 Peak-Side-Lobe-Ratio (PSLR) 29
2.3.4 Integrated-Side-Lobe-Ratio (ISLR) 29
2.3.5 Radar Estimation Rate 29
2.3.6 Communication-Data Rate 30
2.3.7 Spectral efficiency: 30
2.3.8 Ambiguity Function 31
2.4 Results and Analysis 32
2.4.1 Optimal Waveform Shape of an NLFM signal 32
2.4.2 Effect of Threshold SNR 34
2.4.3 Effect of Order of Phase Polynomial 38
2.4.4 Effect of Energy Constraint on the Proposed Optimization Problem 40
2.4.5 Performance Analysis of Designated Optimum Radar Waveform Design Approaches 42
2.4.6 Waveform Analysis Using Ambiguity Function 44
2.5 Summary 47

3 Optimum Waveform Selection for Target State Estimation in a CRCS 49

3.1 Problem Formulation 49
3.2 Radar Sensor Characterization 53
3.3 Target Tracking 61

3.3.1 Measurement and State Model 63
3.3.2 Filtering 64
3.3.3 Posterior Cramer-Rao Lower Bound (PCRLB) 65
3.4 Results and Analysis 65
3.4.1 Scenario Generation 66
3.4.2 Track filtering 66
3.5 Summary 72

4 Communication-Aided Target State Estimation in a CRCS 73
4.1 Problem Formulation 73
4.2 Characterization of a radar sensor 77
4.2.1 Calculation of Fisher Information Matrix ($\mathbf{J}$) 78
4.2.2 Calculation of Measurement Noise Covariance Matrix ($\mathbf{N}(\mathbf{\Theta_k})$) 83
4.3 Target Tracking 88
4.3.1 Converted Measurements based on Iterative Least Square . . . 89
4.3.2 Tracking 91
4.3.3 Posterior Cramer-Rao Lower Bound (PCRLB) 93
4.4 Simulation Results and Analysis 94
4.4.1 Simulation Scenario 94
4.4.2 ILS performance 94
4.4.3 Kalman Filter performance 94
4.5 Summary 98

5 Conclusions and Future Research Directions 101
5.1 Conclusions 101
5.2 Future Research Directions 103

Bibliography 105

List of Publications 115

List of Figures

1.1 Current RF spectrum environment 1
1.2 Upcoming dynamic RF spectrum environment 2
1.3 Basic Cooperative Radar-Communication System Model 4

2.1 Cooperative radar-communication system model 18
2.2 Flowchart for solving (2.11) 26
2.3 Time domain representation of an NLFM signal with a phase polynomial order (N=6) and a low threshold SNR (-80 dB) 34
2.4 Time domain representation of an NLFM signal with a phase polynomial order (N=6) and a high threshold SNR (50 dB) 34
2.5 Optimized radar waveform spectrum for an NLFM signal with a phase polynomial order (N=6) and a low threshold SNR (-80 dB) 35
2.6 Optimized radar waveform spectrum for an NLFM signal with a phase polynomial order (N=6) and a high threshold SNR (50 dB) 35
2.7 Autocorrelation of optimized NLFM radar waveform for a low threshold SNR (-80 dB) 36
2.8 Autocorrelation of optimized NLFM radar waveform for a high threshold SNR (50 dB) 36
2.9 Impact of the phase polynomial order on side-lobe levels at a low threshold SNR (-80 dB) 39
2.10 Impact of the phase polynomial order on side-lobe levels at a threshold SNR (0 dB) 39
2.11 Impact of the phase polynomial order on side-lobe levels at a high threshold SNR (50 dB) 39
2.12 Energy constrained optimal NLFM radar waveform spectrum 41

2.13 Energy constrained optimal NLFM radar waveform autocorrelation function 41
2.14 Radar estimation rate versus threshold SNR 42
2.15 Communication data rate versus threshold SNR 43
2.16 Ambiguity surface plot with a phase polynomial order (N=6) and a low threshold SNR (-80 dB) 45
2.17 Ambiguity surface plot with a phase polynomial order (N=6) and a high threshold SNR (50 dB) 46

3.1 Cooperative radar-communication system model 50
3.2 Optimal waveform selection based on tracking scenario 53
3.3 Generating a scenario for a single radar-sensor, single communication transmitter 66
3.4 Comparison of range and range rate for rectangular and NLFM waveforms 67
3.5 Comparison of range measurement error for selected waveforms . . . 69
3.6 Comparison of range rate measurement error for selected waveforms . 70
3.7 Analyzing estimated range measurement error for various designated waveforms 71
3.8 Analyzing estimated range rate measurement error for various designated waveforms 72

4.1 System model for cooperative spectrum sharing between radar and communication systems 74
4.2 Tracking framework for CRCS 89
4.3 Convergence of ILS approximation 95
4.4 Comparison of PRMSE with the PCRLB for both the waveform combinations in a CRCS framework 95
4.5 Comparison of Resultant PRMSE and RMSE for both the waveform combinations in a CRCS framework 96
4.6 Comparison between LFM and NLFM radar waveforms in terms of positional RMSE in a CRCS environment 97

4.7 Comparison between LFM and NLFM radar waveforms in terms of overall RMSE in a CRCS environment 97

List of Tables

1.1 Summary of radar sensor-centric waveform design approaches in a CRCS 11

2.1 Convergence time analysis for different chirp order 25
2.2 Comparison of spectral efficiency for various waveform design approaches 31
2.3 List of MATLAB functions used for various waveform design approaches 32
2.4 Specifications used for optimum waveform design 33
2.5 Effect of threshold SNR on the side-lobe levels 37
2.6 Effect of phase polynomial order on the side-lobe levels 40
2.7 Effect of energy constraint on the SBnB approach 41
2.8 Performance analysis of various optimum waveform design approaches 43
2.9 Comparison of PSLR values of various waveform design approaches using ambiguity function 45

3.1 Parameters considered for evaluating the measurement noise covariance matrix 62
3.2 Standard deviation of range and range rate measurements for various waveforms. 63

4.1 Parameters considered for evaluating the measurement noise covariance matrix 84

Abbreviations and Nomenclature

Abbreviations

5G	Fifth Generation
BLUE	Best Linear Unbiased Estimator
CRCS	Cooperative Radar-Communication System
CRLB	Cramar-Rao Lower Bound
CSI	Channel State Information
CV	Constant Velocity
ECM	Electronic Counter Measurements
EKF	Extended Kalman Filter
FCC	Federal Communications Commission
FIM	Fisher Information Matrix
GNN	Global Nearest Neighbour
ILS	Iterative Least Square
IMM	Interacting Multiple Model
ISLR	Integrated SideLobe Ratio
ITS	Intelligent Transportation Systems
JRC	Joint Radar Communication
JRCS	Joint Radar-Communication System

KF	Kalman Filter
LFM	Linear Frequency Modulated
LTE	Long Term Evolution
MATLAB	MATrix LABoratory
MEEV	Minimum Estimation Error Variance
MIMO	Multiple-Input-Multiple-Output
MINLP	Mixed Integer Non-Linear Programming
NLFM	Non-Linear Frequency Modulated
NR	New Radio
PAPR	Peak-to-Average-Power-Ratio
PCRLB	Posterior Cramer-Rao Lower Bound
PDA	Probabilistic Data Association
PKF	Particle Kalman Filter
PRC	Power Ratio Constraint
PSLR	Peak-to-SideLobe-Ratio
PSP	Principle of Stationary Phase
QAM	Quadrature Amplitude Modulated
RF	Radio Frequency
RMS	Root Mean Square
RMSE	Root Mean Square Error
SBnB	Spatial Branch and Bound
SDR	Semi Definite Relaxation

SIC	Successive Interference Cancellation
SINR	Signal-to-Interference-Noise-Ratio
SLC	Spectral Leakage Constraint
SNR	Signal-to-Noise-Ratio
TPC	Threshold Point Constraint
UKF	Unscented Kalman Filter
US	United States
WiFi	Wireless Fidelity

Nomenclature

$\Phi^2_{\text{s.l.}}$	Time-offset between the auto-correlation main-lobe and peak side-lobe
T_{temp}	Absolute temperature
$L(\tau, \omega)$	Likelihood function
R_{est}	Radar estimation rate
$\delta_{\text{constraint}}$	Parameter which decides the size of the feasible solution set
γ	Signal-to-residual noise ratio
α	Receiver estimation parameter vector
$\mathbf{\Theta}_k$	Waveform parameter vector
$\mathbf{J}$	Fisher information matrix
$\mathbf{N}(\mathbf{\Theta_k})$	Measurement noise covariance matrix
$\mathbf{T}$	Transformation matrix
$\mathbf{y}$	Measurement vector of the tracking system

ω	Doppler frequency
Φ	The random phase shift
$\sigma^2_{\tau,\text{proc}}$	Variance of the range fluctuation process noise
τ_{pre}	Predicted target delay
τ	Target round trip time delay
a	Overall target cross-section, antenna and propagation gain
B	Bandwidth of the radar waveform
b	Total gain of the antenna and communication signal transmission loss
B_{rms}	RMS bandwidth of the NLFM waveform
c	Speed of light
E_t	Total available transmitted energy of the radar waveform
E_R	Energy of the target return
H	Measurement transition matrix
k_B	Boltzmann constant
N	NLFM phase polynomial order
$n_{\tau,\text{proc}}(t)$	Range fluctuation process noise
R	Distance from the target to the radar sensor
R_{comm}	Communication system data rate
t_s	Sampling time interval
v_0	Doppler shift
$X(k)$	State vector at k^{th} time instant

$\bar{E}_r$	Average received signal energy
η_0	Phase noise spectral density
$\Lambda(\cdot)$	Likelihood ratio
ω_c	Carrier frequency
σ^2_{estm}	Global estimation error variance
σ^2_{CRLB}	The fundamental lower bound on the estimated error variance
τ_c	Total delay experienced by the received communication signal
$N(f)$	Receiver thermal noise power spectral density
$n(t)$	Thermal noise present in the receiver
$N_{\text{resi}}(f)$	Residual noise power spectral density
P_{r}	Radar transmitted power
p_d	Probability of target detection
p_{fa}	Probability of false alarm
P_{c}	Transmitted power of the communication signal
p_l	Coefficients of the NLFM phase polynomial

Chapter 1

Introduction

1.1 Background

It is a well-known fact that a major portion of the Radio Frequency (RF) spectrum has been allocated to various application-oriented services. Further, due to the proliferation of connected devices and wireless applications, there is a massive demand for more RF spectrum. Hence the RF spectrum has become very much congested. In contrast, the RF spectrum designated for radar applications is underutilized. To combat the spectrum scarcity problem, researchers are looking to exploit the available radar spectrum by sharing it with wireless communication systems. This has spurred people across the globe to focus on shared spectrum access, which controls the in-band interference between radar and communication systems (Griffiths et al. 2015). Sensing

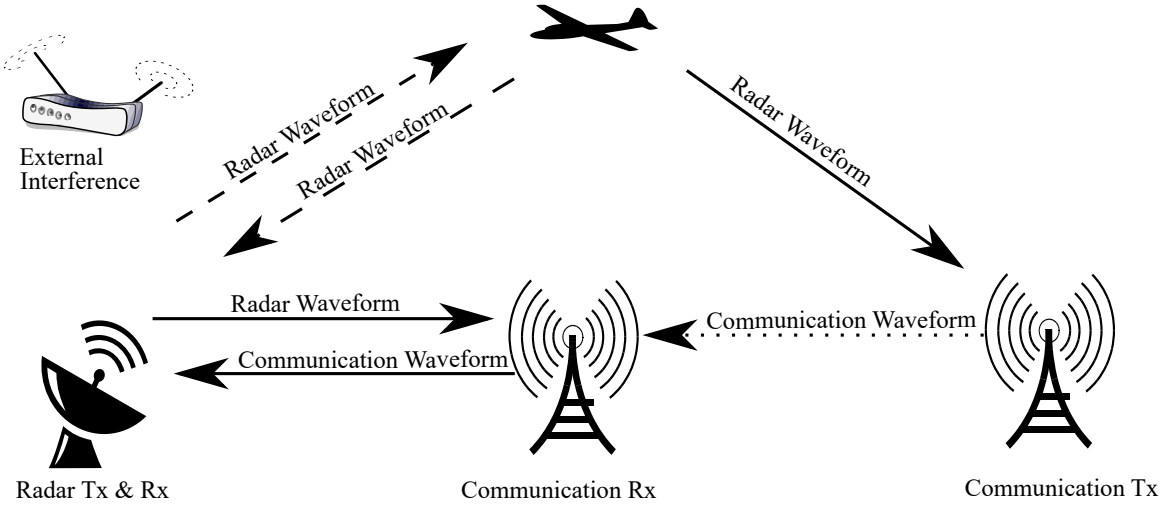

Figure 1.1: Current RF spectrum environment

and communication are the two significant functionalities of radio technology, which

are self-designed and rely on various functions and bands of frequencies. Sensing is responsible for target detection and tracking, whereas communication is considered for transferring information among users. A radar sensor transmits a known signal toward a desired target for sensing purposes. Whereas, the communication system transmits an unknown signal by assuming that the channel has already been estimated. In the coexisted radar-communication scenario, the radar sensor signal can be utilized for the communication channel estimation. A general RF spectral congestion scenario is demonstrated in Figure 1.1, here both radar sensing and communication systems are carrying out their operations in the presence of external interference. Further, both communication and radar systems are operating in the same frequency band or adjacent frequency bands. However, there is mutual interference between both radar and communication systems, when they operate in the same spectral band. In the

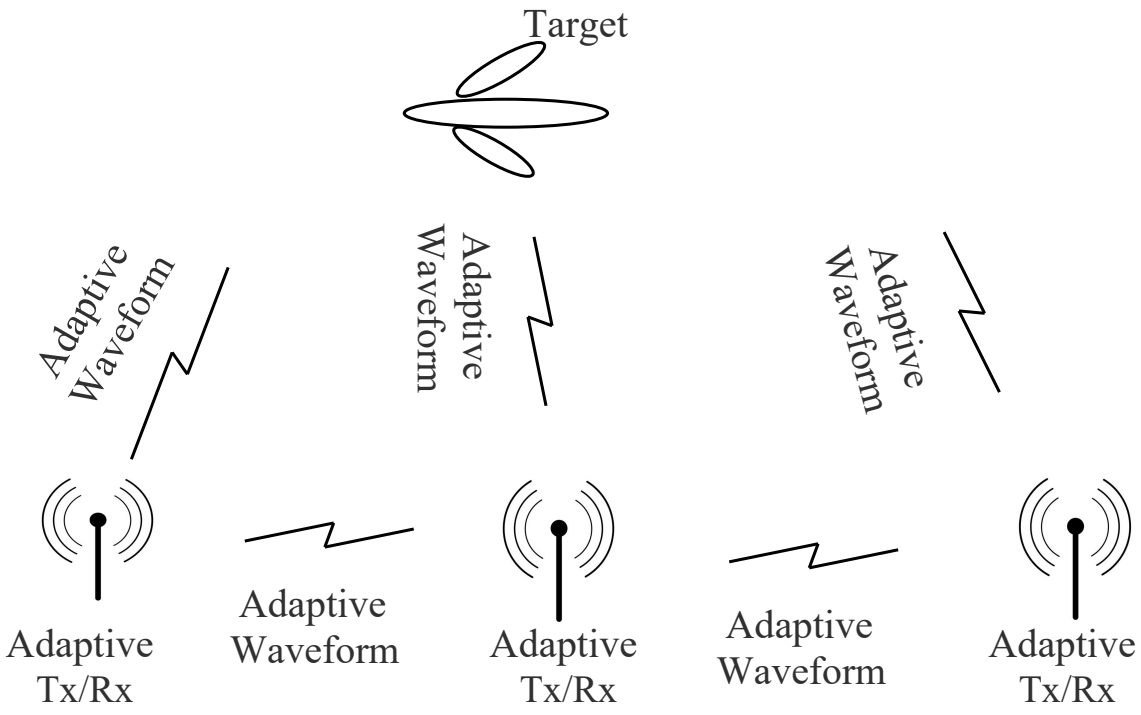

Figure 1.2: Upcoming dynamic RF spectrum environment

future, upcoming RF systems are very much in need of spectral resources. Hence one possible solution is the convergence of RF wireless systems. According to (Paul et al. 2016), an upcoming RF spectral environment is depicted in Figure 1.2, where all the users are adaptive to the spectral environment. Further, both radar and communication systems are cooperative with each other. As the users are dynamic in the above

scenario, they are capable enough to avoid mutual interference. Furthermore, radar and communications users can change their frequency band and work to attain the required radar estimation rate (Bliss 2014) and communication data rate.

1.1.1 Evolution of Cooperative Radar-Communication System (CRCS)

Radar bands are the best candidate to be shared with different communication systems due to a broad chunk of the spectrum being accessible at radar frequencies (Griffiths et al. 2015). Moreover, the sensing mechanism is going to play a pivotal role in upcoming wireless technologies like 6G, Intelligent Transport Systems (ITS) (Ma et al. 2020), smart homes (Huang et al. 2020), and different location-oriented applications (Zhang et al. 2020). These aforementioned applications rely on efficient sensing and communication capabilities. Due to this motive, researchers are intended to focus on Radar-Communication Spectrum Sharing (RCSS) (Liu et al. 2020).

Radar and Communication systems both are independent systems and they have been developed separately. But, there are some similarities in both systems, especially in the receiver section (Zhou et al. 2022). In the past few years, we had seen the proliferation of vibrant academic and industrial interest toward the convergence of sensing and communication functions. In addition to that, government organizations like the Defense Advanced Research Projects Agency (DARPA) (Evans 2016a) started funding to ensure a better quality of military radar and military communications. As a consequence, a large amount of work has been carried out based on different design strategies, a variety of scenarios, and cooperation between the radar and communication systems. According to the literature survey (Liu et al. 2020), RCSS approaches have been categorized into co-existence, cooperation, and co-design.

In the coexistence category, both radar and communication transmitters are active, and both access the radar spectrum (Zheng et al. 2019). Further, both radar and communications transmitters treat one another as interferers. However, the major drawback is to combat mutual interference to accomplish a reasonable performance for both radar and communication systems (Chiriyath et al. 2019). Initially, researchers preferred opportunistic spectrum sharing to achieve spectral coexistence (Saruthirathanaworakun et al. 2012). In this approach, communication users are permitted

to transmit when the band of frequencies is not engaged by radar. However, it is possible only when both systems are not operating at the same time. To overcome this, a null-space projection (NSP) scheme was proposed in (Sodagari et al. 2012), where a radar beam pattern is required to aim waves onto the null space of the interference channel connecting the radar transmitter and communication transmitter. Because of NSP, the mutual interference between two sub-systems can be minimized. In (Khawar et al. 2015a), and (Mahal et al. 2017) the NSP scheme was considered to combat mutual interference between MIMO radar and communication systems. However, it results in radar system performance loss. It is always difficult to maintain optimal beamform for the estimation of target detection and target tracking. Later a novel approach was introduced in (Babaei et al. 2013) for relaxing the null steering precoder to enforce allowable interference on the information system. To overcome

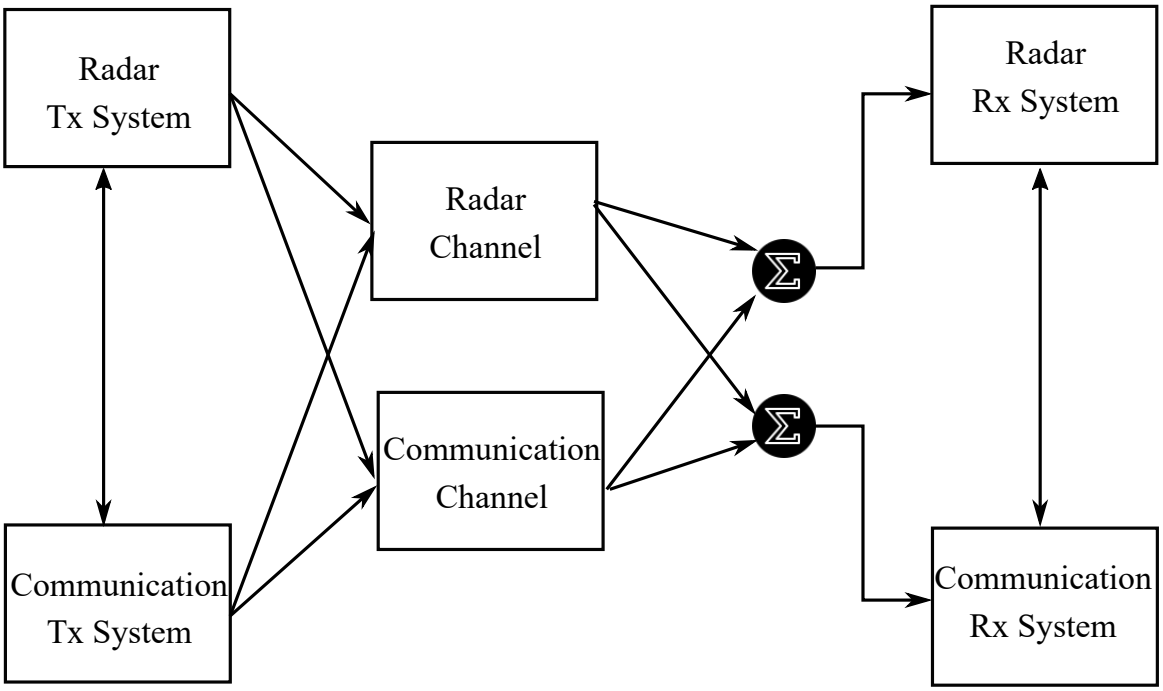

Figure 1.3: Basic Cooperative Radar-Communication System Model

the mutual interference problem in the coexisted radar-communication systems, a cooperative spectrum-sharing approach was proposed in Paul et al. [2016]. In the cooperation category, Channel State Information (CSI) is exchanged between radar and communication systems and it assists each other to avoid mutual interference (Chiriyath et al. 2019). The general cooperative scenario block diagram is depicted

in Figure 1.3. Further, a fusion center was considered in (Li and Petropulu 2017) to exchange the information between both the sub-systems to enhance the performance of the cooperative joint radar-communication system. According to (Li and Petropulu 2017), pilot signals can be utilized to estimate the channels and share CSI with the subsystem. Apart from that, many methods have been proposed in (Mishali and Eldar 2010), and (Cohen et al. 2018) to sense the environment without transmitting a pilot signal or without coordination between subsystems. To share the spectral resources efficiently and accomplish RF convergence, a meticulous understanding of the principal performance limits of cooperative spectrum sharing is desired (Chiriyath et al. 2017).

1.1.2 Applications of Joint Radar-Sensing and Communication

The Radio Frequency (RF) spectrum sharing between communication and radar systems has been inspired by the necessity for the coexistence of radar and communication systems. This section demonstrates the various applications related to the convergence of sensing and communication functions.

A Autonomous systems

The mm-wave band (30GHz-300GHz) is more suitable for autonomous applications, where both sensing and communication operations are involved. Primarily mm-band is traditionally allocated to automotive radars for vehicle collision prevention and it is also used by high-level image resolution radars (Choi et al. 2016). However, this band can be used by wireless communication users to perform short-range communication (Kenney 2011) and for Long Term Evolution (LTE) technology (Choi et al. 2016). Further, this band is proposed for Vehicle-to-Vehicle (V2V) communication for the development of autonomous cars (Tsugawa and Kato 2010). As both sensing and communication applications are interconnected, researchers are strongly motivated to develop joint radar-communication systems for autonomous systems (Sturm and Wiesbeck 2011).

B Air-Traffic-Control (ATC) systems

In these systems, radar sensing and communication play a pivotal role in air-traffic management (Paul et al. 2016). Especially in commercial flights, where radar is utilized for object detection and tracking, and communication system is used for pilot and ATC system coordination. Initially, L-band (1GHz-2GHz) and S-band (2GHz-4GHz) are utilized for ATC radar systems. Recently, these bands are allocated to LTE and 5G new radio wireless technologies (Hessar and Roy 2016). Thus there is a coexistence between radar and communication systems.

C Military Radar and Communication (MRC) systems

In general, the S-band (2GHz-4GHz) and C-band (4GHz-8GHz) are used for military applications like Low-Probability-Intercept (LPI) radar, Unmanned Aerial Vehicles (UAV) utilized for various covert operations such as track and rescue, reconnaissance, and Electronic Countermeasures (ECM) (Schneiderman 2011), (Bogdanowicz 2017). However, all the applications require both sensing and communication functionalities. Moreover, Shared Spectrum Access for Radar and Communications (SSPARC) program was keen to allocate a part of the C-band for wireless communication users (Evans 2016b). With the rapid growth in the usage of wireless applications, there will be huge pressure on military radar bands for spectrum-sharing purposes (Griffiths et al. 2015). The feasible coexisting military radar and communication applications are namely, LPI communication, passive radar, UAV communication and sensing, and dual-function RF system.

D Healthcare and Monitoring systems

These systems utilize the Industrial Scientific and Medical (ISM) band and Wireless Medical Telemetry Service (WMTS) frequency band (1.35GHz-1.45GHz) for healthcare and monitoring purposes. To monitor the health condition of a patient, bio-sensors are biologically embedded into the human body. Bio-sensors measure the data from the human body and then the data is transmitted to an external signal-processing device for further action (Liu et al. 2020). Further, cloud-based approaches were developed to convey the bio-sensing data to external devices (Fortino and Pathan 2014). Thus there is a possibility to combine both sensing and communication func-

tions. An experimental study was conducted in (Hakozaki and Shinoda 2002), where a tactile bio-sensor element communicates via skin layers to the external device for further signal processing. However, still, there is a lot of scope for research in this area.

E Imaging and Communication Systems

The upper millimeter (mm) wave frequency band (52.6 GHz-114.25 GHz) (Raghavan et al. 2020) has been allotted for fine-resolution image sensing and also supports large throughput-based wireless communications (Paul et al. 2016). For example, Google has introduced a project by the name Soli, which performs accurate human gesture detection by utilizing 60 GHz millimeter wave radar (Gu et al. 2016), (Ren et al. 2021). Further, this mm-wave radar can be interfaced with 5G smartphones and tablets for further device-device communication (Rappaport et al. 2011). Thus Google has given the motivation to look for a smart radio which can perform both sensing and communication operations on a unique hardware platform.

F Light-based sensing and communication systems

With the proliferated development of wireless technologies, the RF spectrum is scarce in nature. This has made researchers think about light-based systems that avoid spectrum congestion issues (Langer and Grubor 2007). A new technology Li-Fi (Light Fidelity) was developed in (Bellè et al. 2013), which is analogous to Wi-Fi systems. The Li-fi technology was developed to fulfill the user requirements like high throughput and fast data transmission (Elgala et al. 2011). In addition, optics is also a very fast-growing technology used for remote sensing applications (Wehr and Lohr [1999]). Subsequently, lidar is used for surveillance of wetlands (Lang et al. 2010) and optics-based remote sensing is used for sea level monitoring (Brock and Purkis 2009). Here also there is a feasibility for the coexistence of Lidar and Li-Fi systems.

G RFID systems

A Radio Frequency Identification (RFID) system contains a reader, an antenna array of a reader, and tags. Firstly, the reader sends a sensing signal toward the tag, then the tag modulates the signal and reverts it back to the reader. The reflected signal

consists of a special signature created according to the change in the tags antenna load (Decarli et al. 2013). Communication is the principal operation of the RFID technology, as the tag is reflecting some valid information concerning health and identity (Farris et al. 2014). RFID technology has also been deployed for radar target detection (Yen et al. 2007) and target localization (Decarli et al. 2013). Thus RFID system is a kind of cooperative radar-communication system as the RFID sensing is accomplished by setting up a cooperative communication link between the tag and reader.

All these applications motivated us to work towards the modeling of a cooperative radar-communication system.

1.2 Literature Survey

1.2.1 Waveform Design for a CRCS

The primary step in developing a Cooperative Radar Communication System (CRCS) is to identify a suitable waveform and its characteristics (Sturm and Wiesbeck 2011). In (Hassanien et al. 2016), the radar waveform is considered for both sensing and communication operations in a CRCS. By using radar waveform for both radar and communication systems, the allocated spectrum would be utilized very efficiently. However, the aforementioned approach introduces problems like data-dependent ambiguities and high Peak-to-Average-Power-Ratio (PAPR) requirements (Sturm and Wiesbeck 2011). In addition, both communication and radar systems have distinct waveform requirements. In contrast to the previous approach, two different waveforms are considered for both sensing and communication functions in (Chiriyath et al. 2019). Whenever two separate waveforms are considered for both radar and communication systems, several constraint-based radar waveform design methods have been proposed (Patton et al. 2012). With reference to (Bică and Koivunen 2018), (Chiriyath et al. 2019), the waveform design approaches for a CRCS are categorized into the radar sensor-centric method and communication-centric method. In the radar sensor-centric approach, the radar waveform is optimized to improve the performance of a CRCS, whereas, in the communication-centric approach, the communication waveform is optimized to improve the performance of a CRCS. However, in our research

work, a radar-sensor-centric approach is considered.

1.2.2 Radar Sensor-Centric Approaches

An adaptive radar waveform was first projected onto the null space between the radar and communication systems to avoid mutual interference in a CRCS (Sodagari et al. 2012). Subsequently, a Null Space Projected (NSP) constrained optimal Multiple-Input-Multiple-Output (MIMO) radar waveform was designed in (Khawar et al. 2014) to avoid mutual interference in a CRCS. Later, a spectrally constrained optimal radar waveform was designed in (Aubry et al. 2014) to reduce the interference to neighboring communication users in a CRCS. Further, the radar waveform was optimized based on maximizing the SINR subject to the Energy Constraint (EC), Maximum Allowable Interference Energy Constraint (MAIEC), and Similarity Constraint (SC). Whereas in (Khawar et al. 2015b), a radar waveform was designed using an antenna array by considering the NSP and imposing the constraint on interference power received at the MIMO cellular base stations to further mitigate the mutual interference in a CRCS. Further, an optimal radar waveform was designed based on maximizing the Signal-to-Interference-Noise-Ratio subject to MAIEC, Radar Waveform Energy Constraint (RWEC), and SC to further enhance the performance of a CRCS (Aubry et al. 2015). Furthermore, an Interference Protection Criteria (IPC) at the communication receiver was defined in (Govoni 2016) to improve the military radar performance in a CRCS without any interference to communication users. Later, a radar waveform is optimized based on EC, MAIEC, and SC to specifically improve the performance of a radar system in a CRCS (Aubry et al. 2016b). On the other hand, a Small Singular Value Space Projection Method (SSVSPM) was proposed in (Mahal et al. 2017), where a radar precoder was designed to avoid interference with neighboring communication users in a CRCS. In (Paul et al. 2016), a Linear Frequency Modulated (LFM) radar waveform is developed based on a polynomial spectral mask to jointly maximize both the radar estimation rate and communication data rate in a cooperative scenario. In (Huang et al. 2017, a Radar Environmental Map (REM) was utilized to restrict the radar waveform spectrum such that the radar band is allowed for cooperative transmission. In (Qian et al. 2018), an optimum MIMO radar waveform was designed based on maximizing the Signal-to-Interference-Noise-Ratio (SINR)

at the radar receiver subjected to Constant Modulus Constraint (CMC), Similarity Constraint (SC), Energy Constraint on the Communication waveform (ECC), and Communication Rate Constraint (CRC), in a CRCS. Whereas in (Bică and Koivunen 2018), the radar waveform was optimized to estimate the parameters of a radar target in the CRCS environment. Further, the optimization was carried out by considering CRLB as an objective function subject to the Radar Transmitted Power Constraint (RTPC), MAIEC, and Sub-carrier Power Ratio Constraint (SPRC). Later, a unique estimation error variance approach was proposed in (Chiriyath et al. 2019), to optimize the Non-Linear Frequency Modulated (NLFM) radar waveform spectrum for improving the performance of both radar and communication systems in a CRCS. In this approach, Cramer-Rao-Lower-Bound is considered the objective function and is minimized subject to the Threshold Point Error Variance Constraint (TPEVC) and Spectral Leakage Constraint (SLC). In all the previous contributions, the formulated optimization problem is non-convex, which obtains only a locally optimum solution. A quick summary of all the radar sensor-centric approaches is listed in Table 1.1.

1.2.3 Target Tracking

Target tracking is an important aspect of a radar-sensing system to estimate the trajectory of a radar target within a surveillance space. The major blocks present in the target tracking system are track-filtering and data association. Track-filtering is the process of finding the target trajectory (i.e., target position, target velocity) of a track based on sensor measurements (i.e., target range, azimuth angle, and elevation angle) that have been allocated to the track (Richards et al. 2010). Data association is the process of associating the measurement to a particular track (Richards et al. 2010). The Kalman Filter (KF) predicts the target state at the time instant of the most recent radar measurement based on the present target state. It gives an optimal state estimate subject to linearity and Gaussian distribution (Bar-Shalom et al. 2004). Subsequently, various types of Kalman Filters like extended, unscented, and particle filters were considered to deal with the issue of non-linearity (Bar-Shalom et al. 2010). In the context of data association, traditional association approaches like Nearest Neighbour (NN) and Global Nearest Neighbour (GNN) are used to extract a unique measurement out of all accessible measurements present in the validation

Table 1.1: Summary of radar sensor-centric waveform design approaches in a CRCS

Ref. No	Objective function	Constraints	System performance	Year
Sodagari et al. [2012]	Minimizing the CRLB	NSP	Target direction estimation	2012
Khawar et al. 2014	Matching of desired radar beam pattern	Constant envelope, NSP	Transmitted beam pattern and Mean Square Error (MSE)	2014
Aubry et al. 2014	Maximizing the SINR	EC, MAIEC, SC	Radar target detection and tracking	2014
Khawar et al. 2015b	Minimizing the interference due to MIMO radar users at the cellular basestation	NSP	Radar transmit beam pattern	2015
Aubry et al. 2015	Maximizing the SINR	MAIEC, RWEC, SC	Energy Spectral Density (ESD) of radar waveform	2015
Govoni 2016	Maximizing SIR	IPC at the communication receiver	Power Spectral Density (PSD) of radar and communication signals	2016
Aubry et al. 2016b	Maximizing SINR	EC, MAIEC, SC	SINR and ESD of radar waveform	2016
Mahal et al. 2017	Minimum difference between the precoded and original radar signal.	Interference power constraint	MSE of radar waveform and BER of communication waveform	2016
Paul et al. 2016	Maximizing information rate	Polynomial spectral mask	Radar estimation rate and communication rate.	2016
Huang et al. 2017	Maximizing SINR	EC, MAIEC, SC	ESD and auto-correlation characteristics	2017
Qian et al. 2018	Maximizing SINR	CMC, ECC, CRC	SINR of both radar and communication systems	2018
Bică and Koivunen 2018	Minimizing CRLB	RTPC, MAIEC, SPRC	Target estimation error variance	2018
Chiriyath et al. 2019	Minimizing CRLB	TPEVC, SLC	Radar estimation rate and communication rate	2019
Mahipathi et al. 2023	Minimizing CRLB	TPEVC, PRC	Radar estimation rate and communication rate	2023

gate (Sinha et al. 2012). Alternatively, to ensure a linear combination of all the radar measurements within the validation gate, a Probabilistic Data Association (PDA) approach is presented in (Bar-Shalom et al. 2009). When it comes to tracking management, the general approaches are quality-based track maintenance and logic-based track maintenance (Jiang et al. 2014).

1.2.4 Waveform Design for Target Tracking

The traditional method of designing the target tracking system is to consider the sensor and tracking sub-systems as entirely separate entities (Bar-Shalom and Fortmann 1988). Authors in (Kershaw and Evans 1997) accomplished significant performance enhancement for a tracking system, by integrating the waveform optimization block (sensor) into a target tracking system. In addition, adaptive waveform design schemes have been proven to greatly enhance the target tracking system performance (Kershaw and Evans 1994). Further, information about the target environment is assessed

based on previous measurements and is utilized to modify the waveform for the subsequent signal transmission to achieve optimal tracking performance (Sira et al. [2008]). The adaptive waveform selection for radar target tracking was initially introduced in (Kershaw and Evans 1994), where the tunable waveform specifications were identified for tracking in a unidirectional clutter-free environment. Subsequently, the adaptive waveform selection schemes were presented to improve target tracking performance in a cluttered environment (Kershaw and Evans 1997). In addition, the adaptive waveform selection schemes were further analyzed for enhancing the target tracking performance in a two-dimensional scenario under a wide-band environment (Sira et al. 2007). The target tracking the performance of various waveforms was analyzed using the statistically estimated steady-state error (Rago et al. 1998). Subsequently, a stochastic-approximation-based particle filter is applied in (Sira et al. 2004) to optimize the waveform parameters to reduce the tracking error variance. A benchmark problem was presented in (Blair et al. 1998), to track the moving targets in the existence of Electronic Counter Measurements (ECM) and false alarms. A review on waveform agile target tracking was presented in (Sira et al. 2009). Further, it also explained the significance of dynamic waveform selection for tracker requirements. In another communication, (Satapathi and Pathipati 2017), a systematic method based on waveform agile sensing is presented, to improve the performance of benchmark target tracking in the existence of hefty interference. Later, an improved target estimation performance is achieved by exploiting the target returns from a communication transmitter (Gunnery et al. 2021). Recently, radar target tracking performance is analyzed in the presence of in-band communication interference in a radar-communication system (Srinath et al. 2022).

1.3 Motivation

Based on the literature review, in the radar waveform optimization, the local minimum problem, and global optimization-based approaches are needed to be explored. Further, to improve the radar estimation rate, without sacrificing the communication data rate, an efficient global optimization approach is very much needed. Therefore, a Spatial Branch and Bound (SBnB) framework is proposed in our work to

design a globally optimized non-linear Frequency Modulated (NLFM) radar waveform. Specifically, the SBnB approach performs global optimization to determine the phase coefficients of an NLFM waveform to achieve desired radar waveform spectrum.

Further, optimal waveform selection and track filtering for improving the tracking performance are hardly reported in the CRCS framework. Hence, an optimal waveform selection strategy is proposed for enhancing the target state estimation performance in a CRCS. In addition, exploitation of the communication waveform along with the radar waveform for target state estimation in a CRCS environment is hardly noticed in any of the previous works. This has motivated us to work on communication-based target tracking in the CRCS configuration.

1.4 Research Objectives

Based on research gaps identified in the literature survey, the following research investigation has been proposed. The major focus of this research is to develop a novel framework to optimize the radar waveform such that the performance of a cooperative radar-communication system can be improved. In addition, a novel measurement model is introduced to analyze the target state estimation performance in a cooperative radar communication system. The proposed three objectives are

- To propose a globally optimized radar waveform for improving the performance of the cooperative radar-communication system.
- To perform an optimum waveform selection for a better target tracking performance in the cooperative radar-communication system.
- To analyze a communication-aided target state estimation in a cooperative radar-communication system.

1.5 Proposed Methodology for Each Identified Research Objective

1.5.1 Constraint-based Radar Waveform Optimization

A Modified PRC-CRLB (M-PRC-CRLB) radar waveform design approach is presented as an alternative local optimization approach by relaxing the spectral leakage

constraint. Further, a global optimization-based Spatial Branch and Bound (SBnB) framework is proposed to improve the performance of a CRCS. Furthermore, a comprehensive performance evaluation is carried out in the range domain, for an NLFM waveform based on the proposed and existing approaches for all phase polynomial orders using PSLR and ISLR metrics. Moreover, the Doppler performance is also analyzed for an optimized NLFM waveform.

1.5.2 Optimal Waveform Selection for Target State Estimation

The measurement noise covariance matrix is derived for various waveforms to characterize the sensor behavior in the presence of communication residual components for the Cooperative Radar-Communication System(CRCS). Further, the Kalman Filter (KF) is applied to estimate the trajectory of a linearly moving target with the obtained measurements for different waveforms using the novel measurement model for the CRCS. Furthermore, the proposed work conducts the performance validation of a radar sensor for various designated waveforms namely rectangular pulse, triangular pulse, Gaussian pulse, LFM pulse, LFM-Gaussian pulse, and NLFM pulse by the PCRLB limit.

1.5.3 Communication-aided Radar Target State Estimation

The proposed work introduces a communication-aided measurement noise model for improving the target state estimation. Measurement noise covariance matrix is evaluated for both the waveform combinations i.e., NLFM radar waveform and QAM communication waveform, LFM radar waveform, and QAM communication waveform to characterize the active radar sensor behaviour. Further, at a given epoch, the target position is estimated by considering the range and range-rate measurements in an iterative least squares framework. Furthermore, the ILS is tuned with the waveform-assisted noise measurement model. Thereafter, the Kalman Filter (KF) is deployed to estimate the time-varying target dynamics by taking the output of the ILS as a measurement model. Moreover, the state estimation errors are validated with the PCRLB.

1.6 Contribution of the Thesis

This research investigation mainly focuses on the problems identified in a cooperative radar-communication system. The thesis contribution solves significant problems like radar waveform optimization, waveform selection for target tracking, and communication-aided target tracking. The major contributions of the thesis are listed below:

1. We have proposed a Spatial Branch and Bound (SBnB) framework to globally optimize the radar waveform such that the performance of a CRCS can be improved.

2. We have presented a novel measurement model based on the communication residual component to estimate the target state for various waveforms in a CRCS. Further, the state estimation errors for various waveforms are validated with the PCRLB.

3. We have analyzed the communication-aided target state estimation for the LFM and NLFM radar waveforms in a CRCS.

1.7 Overview

The remainder of the thesis is structured as follows. Chapter 2 demonstrates the constraint-based radar waveform optimization for a cooperative radar communication system. This chapter proposes the Spatial Branch and Bound (SBnB) optimization framework to improve the performance of a CRCS. Subsequently, Chapter 3 presents the optimal waveform selection scenario for performing target state estimation in a CRCS. This chapter focuses on the influence of the communication residual component on the radar system performance. Further, Chapter 4 introduces a communication-aided novel measurement model to analyze the target tracking performance in a CRCS. Eventually, the thesis ended with the conclusions and future directions.

Chapter 2

Constrained Radar Waveform Optimization for a CRCS

This chapter presents a constraint-based Non-Linear Frequency Modulated (NLFM) radar waveform optimization in a CRCS environment. In addition, the significance of the Spatial Branch and Bound (SBnB) framework in designing a globally optimized radar waveform for improving the performance of a CRCS is elucidated.

2.1 Problem Formulation

A Cooperative Radar Communication System (CRCS) model is shown in Figure 2.1. In this system model, both the radar and communication systems coexist spectrally and temporally. Moreover, the proposed model is informative and can be expanded to more intricate scenarios by utilizing it as a building block to set up real-world scenarios like Intelligent Transportation Systems (ITS) (Singh et al. 2021). In Figure 2.1 only a single radar with a target and one communication transmitter has been considered. Further, the JRC node acts as a radar transmitter/receiver and communication receiver. Subsequently, both radar and communication systems transmit separate waveforms and a radar-centric approach (Aubry et al. 2016a) is considered in this investigation. Here, the joint radar-communication receiver is capable of simultaneously estimating the target measurements (delay, Doppler, azimuth angle, and elevation angle) of the radar and estimating the data rate of a communication signal. In this work, the following assumptions are made:

- A radar-centric approach is considered to design a constant modulus waveform for a CRCS framework.

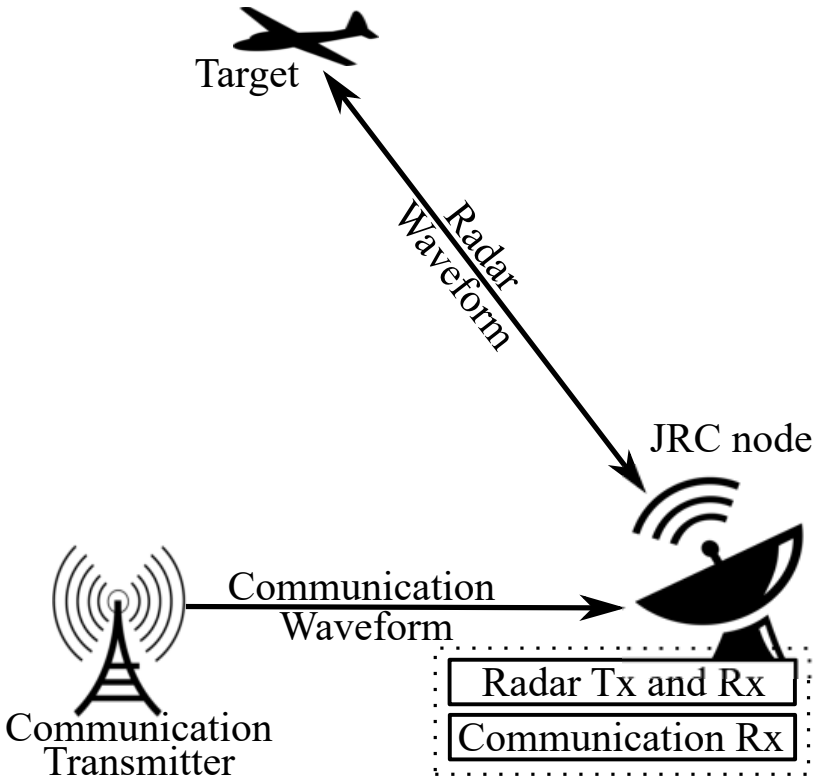

Figure 2.1: Cooperative radar-communication system model

- Radar system is a mono-static single-input single-output (SISO) pulsed system. Further, the radar target is assumed to be stationary during the monitoring time.

- Radar detection and acquisition of the target have already been ensured and the ambiguities between successive radar pulses are ignored.

- Radar target cross-section is well approximated. Further, the effect of clutter on radar performance is excluded.

Moreover, the Successive Interference Cancellation (SIC) receiver model (Bliss 2014) is considered. In the SIC receiver model, the communication system performance relies on the radar waveform spectrum (Chiriyath et al. 2016c). The SIC receiver model mitigates the interference between radar and communication systems. An elaborated discussion on the SIC receiver model is presented in (Mahipathi et al. 2021). In the SIC receiver model, the composite radar-communication signal $y(t)$ at the receiver is given by (Chiriyath et al. 2019),

$$y(t) = b\sqrt{P_{\mathrm{c}}}\, r(t) + n(t) + \sqrt{P_{\mathrm{r}}}\, a \cdot\ s(t-\tau)\,, \tag{2.1}$$

after deducting the predicted radar return from (2.1), the received signal at the communication receiver becomes,

$$\tilde{y}(t) = b\sqrt{P_{\mathrm{c}}}\, r(t) + n(t) + \sqrt{P_{\mathrm{r}}}\, a[s(t-\tau) - s(t-\tau_{\mathrm{pre}})]\,, \tag{2.2}$$

where b represents the total gain of the antenna and communication transmission loss, P_{c} denotes the communication power, $r(t)$ denotes the communication signal received, and the thermal noise in the receiver is represented by $n(t)$, P_{r} denotes the radar transmitted power, a indicates the total target antenna gain, transmission and cross-section gain, $s(t-\tau)$ represents the actual target return, $s(t-\tau_{\mathrm{pre}})$ represents the predicted radar return and τ_{pre} is the predicted target delay. The noise and residual component together is given by (Chiriyath et al. 2016c),

$$\begin{aligned} n_{\mathrm{int+n}}(t) &= n(t) + n_{\mathrm{resi}}(t) \\ &= n(t) + \sqrt{\|a\|^2 P_{\mathrm{r}}}\, n_{\tau,\mathrm{proc}}(t)\, \frac{\partial s(t-\tau)}{\partial t}, \end{aligned} \tag{2.3}$$

where $n_{\tau,\mathrm{proc}}(t)$ represents the range fluctuation process noise with variance $\sigma^2_{\tau,\mathrm{proc}}$. The noise component's residual power spectral density is given by,

$$\begin{aligned} N_{\mathrm{int+n}}(f) =& N(f) + N_{\mathrm{resi}}(f) \\ =& k_B\, T_{\mathrm{temp}}\, \Pi_B(f) \\ &+ (4\pi^2)\, \|a\|^2\, P_{\mathrm{r}}\, \sigma^2_{\tau,\mathrm{proc}}\, \|S(f)\|^2\, f^2, \end{aligned} \tag{2.4}$$

where $N(f)$ represents the receiver thermal noise power spectral density, $N_{\mathrm{resi}}(f)$ represents the residual noise power spectral density, k_B denotes the Boltzmann constant, T_{temp} represents the absolute temperature, and $\Pi_B(f)$ is a rectangular spectrum in the range $\frac{-B}{2}$ to $\frac{B}{2}$. Here, the effect of residual noise spectral density is very high compared to thermal noise spectral density on the communication system performance. Therefore, we considered only residual noise spectral density to estimate the communication system performance.

Further, we have chosen an efficient spectral water filling algorithm (Cover and Thomas 2006, Gallager 1968) to optimize the communication power spectrum with respect to the residual noise power spectral density. From (2.4), it is clear that the residual noise spectral density relies on the radar waveform spectral shape. Hence, it is essential to optimize the radar waveform spectrum to achieve desired radar performance without sacrificing the performance of a communication system.

2.1.1 NLFM Radar Waveform Optimization

Modern radar systems desire the waveform to be a constant modulus. To ensure the constant modulus attribute of the radar waveform, the NLFM phase polynomial is considered as follows

$$\mathrm{s(t)} = e^{i\pi\left(\sum_{l=1}^{N} p_l t^{2l}\right)}, \tag{2.5}$$

here $p_l \in \mathrm{R}, \forall l$ denotes phase coefficients and N indicates the NLFM phase polynomial order. The phase polynomial is expressed in even-powered terms to ensure the shape of symmetry in the frequency domain. Here, the radar is a pulsed radar and the pulses are shaped through Non-Linear Frequency Modulation (NLFM) (Blunt and Perrins 2019). Further, the radar duty factor of 0.01 and pulse width of 25.6 μs has been chosen based on the earlier studies (Chiriyath et al. 2017) and (Chiriyath et al. 2019). Furthermore, the peak power is taken as 100 kw and the average power will be 1 kw, sufficient to provide enough energy per pulse.

The radar waveform spectral shape plays a key role in modeling a Cooperative Radar-Communication System (CRCS) (Chiriyath et al. 2016c). However, the radar waveform spectral shape specifically relies on the phase coefficients of an NLFM waveform. Hence, the objective is to globally optimize the phase coefficients (p_l) of an NLFM waveform to achieve adaptive spectral characteristics (adaptive RMS bandwidth) for both radar and communication applications.

Primarily, an optimal radar waveform is designed to minimize the global estimation error variance. To achieve that, it is necessary to minimize the CRLB at the threshold point (Chiriyath et al. 2019). An estimator's threshold point is the radar SNR value at which the estimator's performance deviates from the CRLB owing to non-local estimation errors (Kay 1993). The CRLB for range estimation in a radar system is provided by (Richards et al. 2010),

$$\mathrm{CRLB} = \frac{1}{8\pi^2 B_{\mathrm{rms}}(\bar{p})^2 \mathrm{TB(SNR)}}, \tag{2.6}$$

here 'TB' denotes Time-Bandwidth product and 'B_{rms}' is the RMS bandwidth. It is represented as,

$$B_{\mathrm{rms}}(\bar{p})^2 = \frac{\int f^2 \left\|S(f)\right\|^2 \mathrm{df}}{\int \left\|S(f)\right\|^2 \mathrm{df}}, \tag{2.7}$$

for any specified SNR, an optimum radar waveform is designed based on the threshold point at that specified SNR and has minimal estimation error variance. Threshold

Point Constraint (TPC) is used to eliminate all radar waveforms with higher SNR values above the threshold point. Thereafter, based on the feasible solution set, an optimal radar waveform is determined to minimize the CRLB. The TPC (Chiriyath et al. 2019) is expressed as,

$$\frac{\sigma^2_{\text{estm}}}{\sigma^2_{\text{CRLB}}} \leq \delta_{\text{constraint}}, \tag{2.8}$$

here σ^2_{estm} represents the global estimation error variance, σ^2_{CRLB} represents the fundamental lower bound on the estimated error variance, and $\delta_{\text{constraint}}$ is a parameter, whose value decides the size of the feasible solution set. To share the radar band with communication users, a Power Ratio Constraint (PRC) is introduced in (Mahipathi et al. 2021). This PRC constraint shares the available radar waveform spectral energy uniformly and it also reduces the range-domain ambiguities. The PRC is expressed as,

$$(S(f))^H \odot (S(f)) \leq \frac{1}{\text{N}}\|\text{S(f)}\|^2\text{PRC} \tag{2.9}$$

Where, $S(f)$ is the spectrum of the input signal, $(S(f))^H$ represents the Hermitian transpose of $S(f)$, $\odot$ indicates the elementwise vector/matrix product, N represents the total number of samples and PRC is the power ratio constraint. The PRC is defined as:

$$PRC = \frac{\max|S(f)|^2}{\frac{1}{N}\|S(f)\|^2} \tag{2.10}$$

The Spectral Leakage Constraint (SLC) was introduced in the MEEV approach (Chiriyath et al. 2019) to limit the RF energy in a specific band within the system bandwidth. However, SLC restricts the spectrum-sharing capabilities of a radar waveform. So, in the proposed approaches, we relaxed the SLC in solving the optimization problem. Based on the PRC and TPC, a Modified PRC-CRLB (M-PRC-CRLB) optimization approach is proposed to obtain adaptive radar spectral characteristics, which is provided by,

$$\begin{aligned} \underset{\bar{p}}{\text{minimize}} \quad & \frac{1}{8\pi^2 B_{\text{rms}}(\bar{p})^2 TB(SNR)}, \\ \text{subject to} \quad & p_l \in [0, 10] \quad \forall l \\ & \frac{\sigma^2_{\text{estm}}}{\sigma^2_{\text{CRLB}}} \leq \delta_{\text{constraint}} \\ & (S(f))^H \odot (S(f)) \preceq \frac{1}{N}\|S(f)\|^2 PRC \end{aligned} \tag{2.11}$$

The M-PRC-CRLB approach provides improved radar spectral characteristics compared to the MEEV and PRC-CRLB approaches. However, the optimized solution is still stuck at the local minimum. Therefore, there is a strong need to globally optimize the phase coefficients to achieve the desired spectral characteristics. In this regard, a global optimization-based Spatial Branch and Bound (SBnB) framework is applied to the optimization problem given in (2.11). Detailed information regarding the SBnB framework is explained in Section 2.2.4. Based on the globally optimized phase coefficients, the performance analysis is carried out in the spectral domain and range domain and simulated results are presented in Section 2.4 to demonstrate the effectiveness of the proposed approaches.

2.2 Radar Waveform Design Approaches for a CRCS

In this section, we concisely discuss the existing radar waveform design approaches, namely the Minimum Estimation Error Variance (MEEV) approach (Chiriyath et al. 2019) and the PRC-CRLB approach (Mahipathi et al. 2021). Subsequently, a proposed local optimization-based M-PRC-CRLB radar waveform design approach is presented in this section. Eventually, a proposed global optimization-based Spatial Branch and Bound (SBnB) approach is presented in this section.

2.2.1 MEEV Approach

In this approach, the optimal NLFM radar waveform spectrum is designed to maximize the information rate of a CRCS. However, the optimal NLFM spectral shape depends on the phase coefficients. An optimized radar spectrum can be achieved by minimizing the CRLB at the threshold SNR value. Thus, to get the optimum radar waveform spectrum, a non-convex optimization problem is formulated. In this approach, the objective function (CRLB) is solved locally according to the Threshold Point Constraint (TPC) and Spectral Leakage Constraint (SLC) to get the optimized phase coefficients (Chiriyath et al. 2019). Here, the spectral energy of the radar waveform is concentrated either at the center or edges of the bandwidth according to the threshold SNR value. Further, there is a need to improve radar system performance by maintaining communication system performance. In this approach, adaptive spectral

characteristics are not achieved. Further, it also introduces range-domain ambiguities.

2.2.2 PRC-CRLB Approach

To improve radar waveform spectral characteristics and reduce range-domain ambiguities a PRC-CRLB radar waveform design approach is presented in (Mahipathi et al. 2021). In this approach, to accomplish an optimized radar waveform spectrum, the objective function (CRLB) is locally solved according to the Power Ratio Constraint (PRC), TPC, and SLC. This approach improves the spectral characteristics and range-domain ambiguities compared to the MEEV approach. Further, it improves the radar performance compared to the MEEV approach. However, this approach fails to maintain the communication system's performance. In addition, still, this waveform design approach suffers from dominant side-lobe peaks in the radar spectrum and range-domain ambiguities.

2.2.3 M-PRC-CRLB Approach

In the aforementioned approaches, the SLC confines the radar spectrum within a specific band over the available bandwidth. To achieve adaptive spectral characteristics, a spectrum cannot be constrained to a specific sub-band. Therefore, in this work, SLC is relaxed in solving the optimization problem. We present an M-PRC-CRLB radar waveform design approach to optimize the radar waveform spectrum. To accomplish this, the objective function (CRLB) is solved locally in association with the PRC and TPC. Here the PRC uniformly distributes the spectral energy. However, the optimized solution is still stuck at the local minimum.

2.2.4 SBnB Approach

To accomplish a globally optimized solution (phase coefficients), a Spatial Branch and Bound (SBnB) framework is proposed in this work. Here, a unified optimization framework is proposed using the SBnB algorithm, to optimize the phase coefficients of an NLFM waveform. With reference to the globally optimized NLFM radar waveform, the performance of a CRCS system is improved. Further, we briefly discuss the SBnB algorithm and how it helps in solving a non-convex optimization problem.

Furthermore, an energy constraint is annexed to the proposed optimization problem (2.11) to understand its influence on radar waveform.

SBnB is a deterministic global optimization algorithm (Liberti, Leo) specifically developed to solve non-convex optimization problems. It is a divide-and-conquer technique to find the deterministic solution. Further, the solution should also lie in the feasible region of the given problem.

A Convergence of an SBnB algorithm

The Spatial Branch and Bound (SBnB) algorithm is a method for systematically enumerating alternative solutions by iteratively exploring the problem space (Ellen Zhuang). The main algorithmic strategy is to split the original problem into several subproblems by branching the variables into possible values. For each subproblem, a sequence of asymptotic lower bounds and upper bounds are attained based on well-designed bounding functions. In each iteration, the bounds are updated, and then set the subproblems, this will continue till the convergence Pozo et al. [2011]. SBnB algorithm also converges by an exact selection rule (Ellen Zhuang). Further, the smaller sub-problems are easier to solve than the original problem (Liberti, Leo). However, the SBnB algorithm may not provide convergence in a finite number of steps. A detailed step-by-step SBnB algorithm and flow chart are presented, to clarify how the optimized phase coefficients achieve convergence.

B Convergence time

It is the time required for an SBnB algorithm to find a globally optimized solution for an optimization problem. We have conducted a Monte-Carlo simulation for 1000 runs to attain the optimized phase coefficients and to find convergence time for different chirp orders (N) and SNR values in the range (-80 dB to 50 dB). To measure convergence time in MATLAB, the start time before running the optimization algorithm is recorded. Subsequently, the end time is recorded i.e., the time at which the optimization solution is attained. The difference between the start and end times gives you an estimate of the convergence time. Further, the values are listed in Table 2.1. It is evident from Table 2.1 that, the time required to find the globally optimized solution mainly depends on the complexity of the objective function.

Algorithm 1: Spatial Branch and Bound algorithm for solving (2.11)

Result: p_{opt} = The feasible solution that achieves UB
Input: $B_{\text{rms}}(\bar{p})$, p_0, **SNR**, T, B *and* $p_l \in$ [0,10]
Step 1: Initialization
1. Original problem, set convergence tolerance $\epsilon > 0$
2. Set current best solution:
   $U = \infty \;\; for - \infty < p^* < \infty$

Step 2: Choice of region
1. Choose sub-region S_j of the problem to a single region S.
2. Feasibility-based, tightening of the bounds is performed at each sub-region.

Step 3: Lower bound
1. Non-convex terms are relaxed by convex terms i.e in the form of convex envelopes.
2. Convex relaxation ensures a lower bound to the objective function value in that sub-region.
3. Compute lower bound l of the objective function with solution ${p_j}^L$
   If $l < u$ then compute upper bound u
   Else, the relaxed problem is infeasible, repeat from step 2.

Step 4: Upper bound
1. Compute upper bound u of the objective function with solution ${p_j}^U$
2. The sub-problem is solved based on branching.

Step 5: Pruning
1. If $u < U$ then set $U = u$ and $p^* = {p_j}^U$.
2. Else, repeat from step 2.
3. The regions with lower bounds greater than U are discarded.

Step 6: Check region
1. If $l - u < \epsilon$ then u is identified as the global minimum of the sub-region.
2. Still, if any sub-regions are found then repeat step 2.
3. If there are no sub-regions, the solution converges.

Step 7: Branching
1. Otherwise, partition the region into sub-regions.
2. Continue to repeat step 2.

Table 2.1: Convergence time analysis for different chirp order

Chirp order (N)	**Convergence time**
2	3 Minutes
4	8 Minutes
6	16 Minutes
8	19 Minutes
10	22 Minutes

C Convergence proof

Assume 'S' is the sample space, and it is divided at each iteration because it contains an unqualified region that does not comprise candidate solutions that provide the objective function with more optimal solutions than the incumbent solution. As a result, the best solution may be found in any qualifying sub-region of S_n (Liberti, Leo). However, the spatial branch and bound framework do not promise convergence in a limited number of steps. Instead of the standard concept of optimality, the method here employs the concept of *epsilon*-optimality. The solution $\bar{p}^*$ is globally optimum, when $f(\bar{p}^*) < f(\bar{p})$ for $\bar{p}$ in the problem-space. Since ϵ is positive, $\bar{p}^\epsilon$ in the problem-space is ϵ-globally optimal if the optimum solution is bounded by $s \leq f(\bar{p}^*) \leq S$, here $f(\bar{p}^\epsilon)$ is in $[s, S]$ and $S - s < \epsilon$. Determining the ϵ-globally optimized solution guarantees a finite termination than a typical globally optimized solution (Stein, Oliver, Peter Kirst, and Paul Steuermann).

SBnB algorithm implements the concept of ϵ-optimality (Ellen Zhuang), rather than the regular idea of optimality. Finding the ϵ- global optimum solution ensures a finite termination than a usual global optimum solution. In the SBnB algorithm, the general procedure is to introduce the concept of convex relaxation of the original non-convex problem.

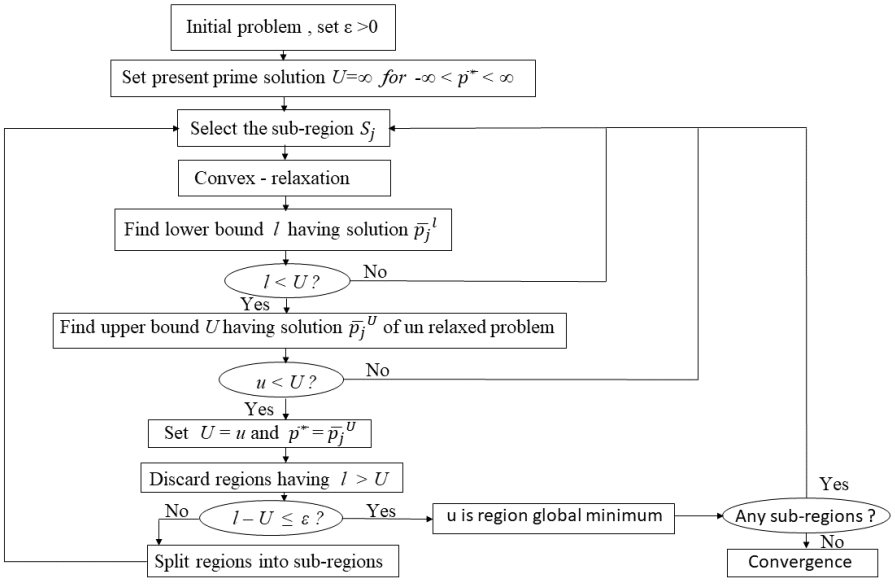

Figure 2.2: Flowchart for solving (2.11)

To perform convex relaxation, the SBnB algorithm replaces the non-convex terms

with the convex envelopes (Stein, Oliver, Peter Kirst, and Paul Steuermann). However, the solution of the modified optimization problem is affirmed to result in the underestimated optimal value of the original objective function (Ellen Zhuang). SBnB algorithm constructs a sequence of subproblems, that attempt to converge to a solution of Mixed Integer non-linear Programming (MINLP) problem (Ellen Zhuang). Algorithm 1 illustrates how the proposed approach reaches to approach a globally optimized solution for a non-convex problem.

2.2.5 Energy Constraint

In practical radar systems, the transmitted energy is limited. So, to limit the transmitted energy, an energy constraint (Tang et al. 2021) is added to the optimization framework given in (2.11). Subsequently, optimized phase coefficients are attained using the SBnB algorithm. Energy constraint is represented as

$$||\mathrm{s(t)}||^2 \leq E_t, \tag{2.12}$$

here E_t is the total available transmitted energy. The spectral and auto-correlation characteristics are analyzed at various threshold SNR values in Section 2.4.4, to understand the influence of energy constraint on the optimized radar waveform.

2.3 Significance of Various Performance Metrics in Optimum Waveform Design

In this section, we concisely discuss the influence of threshold SNR and NLFM phase polynomial order in the design of an optimal radar waveform. Subsequently, the side-lobe performance metrics Peak-Side-Lobe-Ratio (PSLR) and Integrated Side-Lobe Ratio (ISLR) are defined. Further, the radar estimation rate and communication data rate are discussed. In addition, we concisely describe the significance of the ambiguity function.

2.3.1 Threshold SNR

The performance of a JRC system relies on the spectral shape (RMS bandwidth) of the radar waveform (Chiriyath et al. 2016c). More significantly, the choice of threshold SNR is a critical parameter in optimizing phase coefficients, which leads

to the desired radar spectrum. According to locally optimized phase coefficients of NLFM, radar waveform (Chiriyath et al. 2019), for a low threshold SNR value, the probability of side lobe confusion is low in the auto-correlation function. In such cases, most of the spectral energy is concentrated at the center of the bandwidth (Low RMS bandwidth), which is undesirable and affects the radar performance. When the major portion of the spectral energy is focused at the center, it results in a reduction in the noise spectral density, which enhances the communication data rate. Therefore, there is a performance trade-off at a low threshold SNR value.

Contrary to the previous case, for a large threshold SNR value, the probability of side lobe confusion is higher in the auto-correlation function resulting in significant spectral energy concentrated at the edges of the bandwidth (High RMS bandwidth), thereby accomplishing the improved radar estimation rate. However, when the RMS bandwidth is large, noise spectral density is proportionally large, which affects the performance of a communication system. Hence, there exists a trade-off between radar and communication system performance with respect to the SNR threshold value.

To provide enhanced performance of both the subsystems (radar and communication systems) at various threshold SNR values, this investigation focuses primarily on optimizing the phase coefficients of the NLFM radar waveform.

2.3.2 NLFM Phase Polynomial Order

The shape of an NLFM waveform mainly depends on the phase coefficients, which in turn rely on the polynomial order (N). By increasing the polynomial order, the associated degrees of freedom available to design the optimum radar waveform spectrum increase, resulting in optimal waveform with reduced auto-correlation side-lobe levels (Chiriyath et al. 2019). Further, as the polynomial order increases, more energy is located at higher frequencies of the radar waveform spectrum. Hence, the radar estimation rate increases in accordance with the polynomial order. From (2.4), it is evident that at higher frequencies residual noise spectral density is large, which affects the communication data rate. In this work, an in-depth analysis is performed on the auto-correlation characteristics, to observe the effect of phase polynomial order on the side-lobe levels.

2.3.3 Peak-Side-Lobe-Ratio (PSLR)

PSLR is defined as the ratio of the energy present in the peak side-lobe to the energy present in the peak main-lobe (Richards et al. 2010). In our work, PSLR(dB) values are estimated based on the auto-correlation characteristics within the time frame [-4μs, 4μs] (Chiriyath et al. 2019). It is expressed as,

$$\text{PSLR (dB)} = \text{peak side-lobe energy (dB)} - \text{peak main-lobe energy (dB)} \tag{2.13}$$

2.3.4 Integrated-Side-Lobe-Ratio (ISLR)

ISLR is defined as the ratio of the energy present in the side lobes to the energy present in the main lobe (Richards et al. 2010). In our investigation, ISLR(dB) values are estimated based on the auto-correlation characteristics within the time frame [-4μs, 4μs] (Chiriyath et al. 2019). It is expressed as,

$$\text{ISLR (dB)} = \text{side-lobe energy (dB)} - \text{main-lobe energy (dB)} \tag{2.14}$$

2.3.5 Radar Estimation Rate

The performance of a radar system is estimated based on the radar estimation rate. The radar estimate rate determines how much information a radar return carries. The radar estimation rate is provided by (Paul et al. 2016),

$$R_{\text{est}} \leq \frac{\delta}{2T} \log_2 \left[1 + \frac{\sigma^2_{\tau,\text{proc}}}{\sigma^2_{\text{estm}}} \right], \tag{2.15}$$

here, 'δ' denotes the duty factor of the radar, 'T' denotes the time, $\sigma^2_{\tau,\text{proc}}$ indicates the range fluctuation process noise variance and σ^2_{estm} represents the time-delayed estimation variance. The time-delayed estimation variance is derived by utilizing the method of interval errors, which is represented as (Richmond 2006),

$$\sigma^2_{\text{estm}} = [1 - \text{P}_{\text{s.l.}}(\text{ISNR})]\ \sigma^2_{\text{CRLB}}(\text{ISNR}) + \text{P}_{\text{s.l.}}(\text{ISNR})\, \Phi^2_{\text{s.l.}}, \tag{2.16}$$

where $\Phi^2_{\text{s.l.}}$ is time-offset between the auto-correlation main-lobe and peak side-lobe and $\text{P}_{\text{s.l.}}(\text{ISNR})$ is estimated by evaluating the auto-correlation characteristics Bliss and Govindasamy [2013]. Aforementioned parameters ($\text{P}_{\text{s.l.}}(\text{ISNR})$, $\Phi^2_{\text{s.l.}}$) are evaluated based on the auto-correlation characteristicsBliss and Govindasamy [2013]. Generally, a good waveform is characterized by good auto-correlation properties. That is

a high main-lobe peak and very low side-lobe levels. Thus, these kinds of properties guarantee good range resolution performance for closely spaced strong and weak targets. Further, the auto-correlation characteristics mainly depend on the coexistence parameters used for the simulation. Therefore, the radar performance is related to the coexistence parameters used for the simulation listed in Table 2.4.

2.3.6 Communication-Data Rate

The communication system performance is estimated using data rate. A spectral water-filling technique is used to distribute the entire communication power throughout the spectrum to assess the data rate of the communication system. By deploying the optimized communication power spectrum, the optimized communication data rate is estimated. Here, the optimized communication spectrum depends on the residual noise power spectral density. The communication system's data rate in the presence of channel noise with a noise power spectral density ($N_{\text{int+n}}(f)$) is given by (Cover and Thomas 2006),

$$R_{\text{comm}} = \int_{\frac{-B}{2}}^{\frac{B}{2}} df \log_2 \left(1 + \frac{b^2\, P(f)}{N_{\text{int+n}}(f)}\right), \tag{2.17}$$

where $P(f)$ represents optimized communications power spectrum by deploying spectral water filling algorithm provided by Gallager [1968].

$$P(f) = \left(\mu - \frac{N_{\text{int+n}}(f)}{b^2}\right)^{+}, \tag{2.18}$$

here 'μ' is a constant and it is estimated based on the total power constraint, which is represented as

$$P_{\text{c}} = \int_{\frac{-B}{2}}^{\frac{B}{2}} df P(f) \; = \int_{\frac{-B}{2}}^{\frac{B}{2}} df \; \left(\mu - \frac{N_{\text{int+n}}(f)}{b^2}\right)^{+} \tag{2.19}$$

2.3.7 Spectral efficiency:

In a radar system, the spectral efficiency is defined as, the amount of information carried by a radar return in a given bandwidth. Whereas in a communication system, spectral efficiency is defined as the amount of data that can be transmitted over a given bandwidth.

$$\text{Radar system spectral efficiency} = \frac{Radar\ estimation\ rate}{Bandwidth} \tag{2.20}$$

$$\text{Communication system spectral efficiency} = \frac{Communication\ data\ rate}{Bandwidth} \tag{2.21}$$

To estimate spectral efficiency, we considered an NLFM phase polynomial order($N = 6$), threshold SNR = 7.6 dB, and conducted a Monte-Carlo simulation for 100 runs to optimize the phase coefficients. The spectral efficiency is calculated for both the subsystems and values are listed in Table 2.2.

Table 2.2: Comparison of spectral efficiency for various waveform design approaches

Optimum waveform design approach	**Radar system spectral efficiency (milli. bits/seconds/Hz)**	**Communication system spectral efficiency (bits/seconds/Hz)**
Spectral-Mask shaping	0.212	0.0026
Minimum Estimation Error Variance (MEEV)	0.276	1.384
PRC-CRLB	1.9	0.626
M-PRC-CRLB	2.04	0.84
Spatial Branch and Bound	**2.68**	**1.26**

2.3.8 Ambiguity Function

Modern radar systems deploy the matched filter in the receiver section to enhance the Signal-to-Noise-Ratio (SNR), while simultaneously accomplishing the range resolution with appropriate radar waveform design. When the specified waveform is used as the filter input, the ambiguity function of a waveform represents exactly the output of the matching filter for non-zero Doppler values. Because of this precise representation, the ambiguity function is useful for designing and analyzing waveforms. This method provides more insight into the waveform resolution capability in both range and Doppler domains for a given waveform. Based on ambiguity function analysis, one can assess if the given waveform is appropriate for a specific application. More specifically, the ambiguity function is used to characterize the Doppler tolerance of a particular waveform. It refers to the matched filter response in the presence of uncompensated Doppler. The ambiguity function is defined as (Richards et al. 2010)

$$\mathrm{A(t}, f_D) = \left| \int_{-\infty}^{+\infty} \mathrm{s(k)} \exp(j2\pi f_D \mathrm{k}) \mathrm{s'(k\text{-}t)dk} \right| \tag{2.22}$$

Here $s'(\cdot)$ represents the conjugation of $s(\cdot)$, k represents a dummy variable of integration, and $s(k)\exp(j2\pi f_D k)$ is the Doppler-shifted waveform. Doppler tolerance is analyzed by using an ambiguous surface plot.

2.4 Results and Analysis

In this section, the simulation results are presented to affirm the efficacy of the proposed optimization framework outlined in Section 2.1. The proposed M-PRC-CRLB approach and Spatial Branch and Bound (SBnB) approaches are compared with the existing PRC-CRLB approach (Mahipathi et al. 2021) and Minimum Estimation Error Variance (MEEV) approach (Chiriyath et al. 2019). The simulated functions of proposed and existing waveform design approaches are illustrated in Table 2.3. Firstly, in the proposed M-PRC-CRLB local optimization approach, the formulated optimization problem (2.11) is solved to the initial random solution. Subsequently, in the proposed SBnB approach, an SBnB algorithm is deployed to globally solve the optimization problem with reference to the initial randomized solution. Eventually, the solution is obtained with the highest objective function value. All the results are simulated according to the radar and communication system specifications listed in Table 2.4.

Table 2.3: List of MATLAB functions used for various waveform design approaches

S.No	**Type of waveform design Approach**	**MATLAB function**	**Number of Monte-Carlo runs**
1	MEEV	*fmincon*	100
2	PRC-CRLB	*fmincon*	100
3	M-PRC-CRLB	*fmincon*	100
4	SBnB	*ga*	100

2.4.1 Optimal Waveform Shape of an NLFM signal

Primitively, a constraint-based optimization problem formulated in (2.11) is locally solved for MEEV, PRC-CRLB, and proposed M-PRC-CRLB waveform design ap-

Table 2.4: Specifications used for optimum waveform design

Parameter	Value
Radar duty factor (δ)	1%
Pulse width (T)	25.6 μs
Time-Bandwidth (TB) Product	128
Threshold-point constraint $\delta_{\text{constraint}}$	1.01
Center Frequency	3 GHz
Bandwidth (B)	5 MHz
Effective Temperature (T_{temp})	1000 K
Total Power required for a communication system ($\mathbf{P}_c$)	45 W
Antenna gain of the communication system (b)	0 dBi
Communication receiver side-lobe gain	10 dBi
Communication range	10 km
Target range of a radar system	200 km
Antenna gain of radar (a)	30 dBi
Radar transmitted power ($\mathbf{P}_r$)	100 kW
Target cross-section	10 m^2
Target process standard deviation $\sigma_{\tau,proc}$	100 m
Sampling frequency (f_s)	15 MHz

proaches. Subsequently, the same optimization problem is globally solved using the SBnB algorithm to get the optimized phase coefficients for an NLFM radar waveform. The proposed optimization problem is solved at a low threshold SNR value of -80 dB and at a high threshold SNR value of 50 dB. An NLFM phase polynomial order of $N = 6$ is chosen. With reference to the optimized phase coefficients, the simulated results are plotted. The time-domain representation of an optimized NLFM signal is shown in Figures 2.3 and 2.4. It is observed that the amplitude fluctuations are relatively limited for the proposed M-PRC-CRLB and SBnB approaches compared to the MEEV and PRC-CRLB approaches. However, the amplitude fluctuations gradually increase with the increase in threshold SNR value. Further, it is also noticed that a constant modulus nature is apparent from the SBnB-based globally optimized NLFM

waveform.

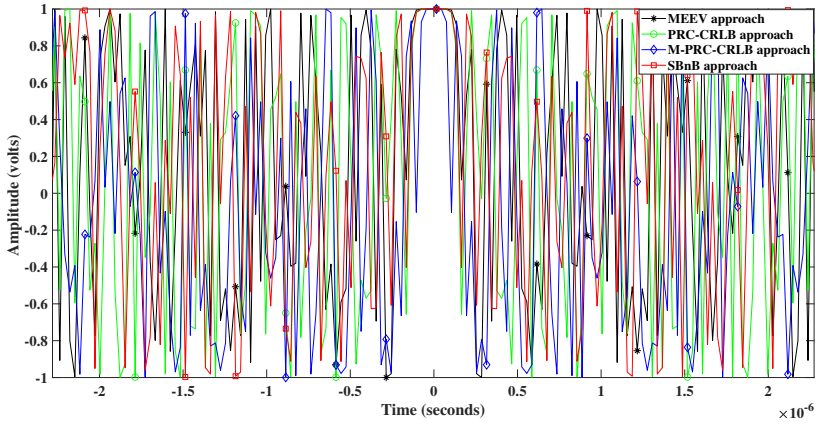

Figure 2.3: Time domain representation of an NLFM signal with a phase polynomial order (N=6) and a low threshold SNR (-80 dB)

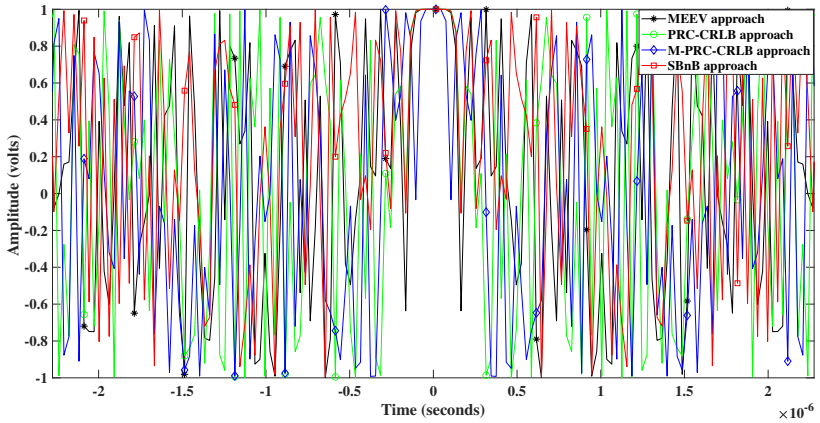

Figure 2.4: Time domain representation of an NLFM signal with a phase polynomial order (N=6) and a high threshold SNR (50 dB)

2.4.2 Effect of Threshold SNR

The impact of threshold SNR on the radar waveform spectrum is already discussed in Section 2.3.1. In Figures 2.5 and 2.6, the spectral energy distribution of proposed M-PRC-CRLB and SBnB approaches are compared with the MEEV and PRC-CRLB approaches for a low threshold SNR value of -80 dB and a high threshold SNR value of 50 dB. Here, an NLFM phase polynomial order of $N = 6$ is considered. From Figures 2.5 and 2.6, it is observed that at low and high threshold SNR values, MEEV and PRC-CRLB approaches can maintain considerable spectral magnitude either at the center or at the edges of the bandwidth. Further, these approaches failed

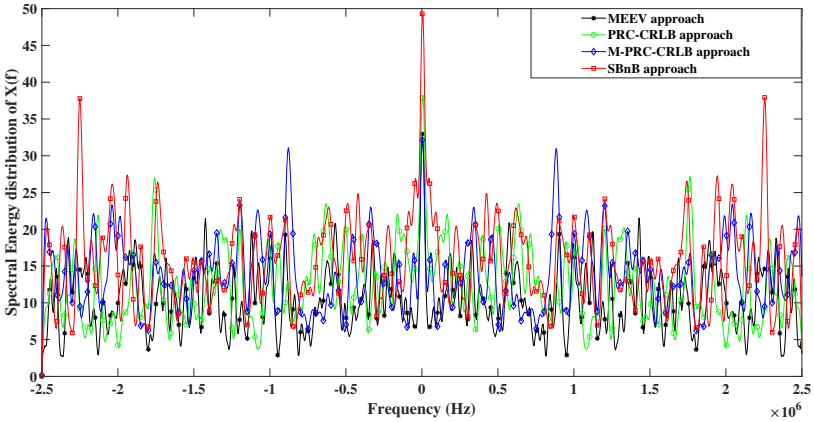

Figure 2.5: Optimized radar waveform spectrum for an NLFM signal with a phase polynomial order (N=6) and a low threshold SNR (-80 dB)

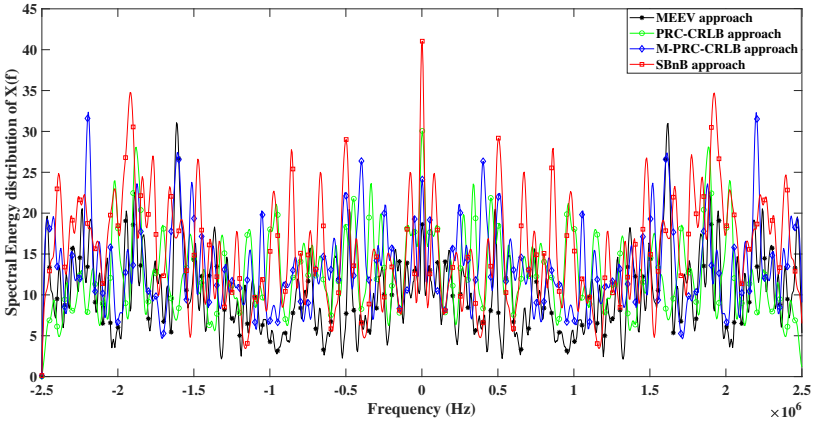

Figure 2.6: Optimized radar waveform spectrum for an NLFM signal with a phase polynomial order (N=6) and a high threshold SNR (50 dB)

to attain the desired adaptive spectral characteristics. Furthermore, in MEEV and PRC-CRLB approaches side-lobe spectral energy is comparable to main-lobe spectral energy. Whereas in the M-PRC-CRLB approach spectral energy is distributed both at the center and edges of the bandwidth for a low threshold SNR value of -80 dB. Further, it is observed that RMS bandwidth is very limited for a low threshold SNR (-80 dB). In addition, the M-PRC-CRLB approach is unable to maintain adaptive spectral characteristics at a high threshold SNR (50 dB). Whereas in the SBnB approach, the RMS bandwidth is adaptive i.e. most of the spectral energy is concentrated not only at the center of the bandwidth (low RMS bandwidth) but also at the edges of the bandwidth (high RMS bandwidth). It is also noticed that even at high threshold SNR values proposed SBnB approach maintains similar spectral characteristics. However, in the proposed approaches, spectral energy contained

in the side lobes slightly increases at a high threshold SNR value. Thus, the SBnB approach globally optimizes the phase coefficients to achieve the intended spectral characteristics, which are desirable for both radar and communication applications.

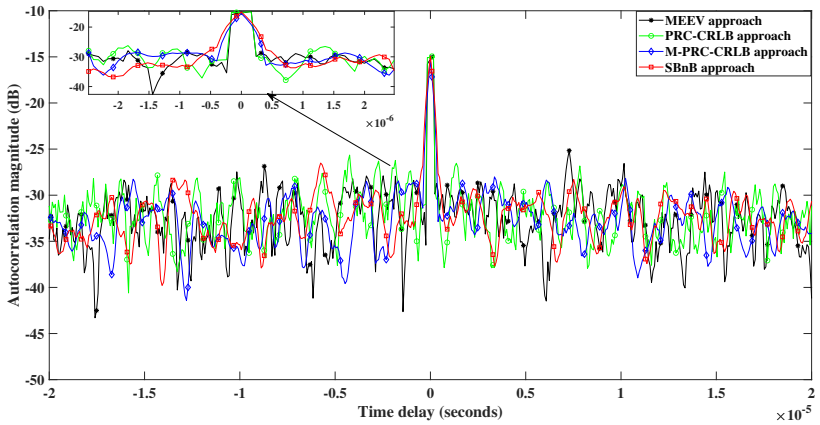

Figure 2.7: Autocorrelation of optimized NLFM radar waveform for a low threshold SNR (-80 dB)

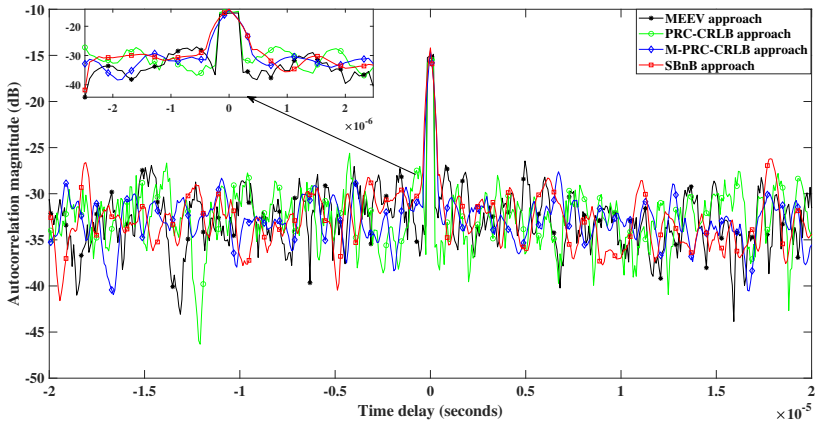

Figure 2.8: Autocorrelation of optimized NLFM radar waveform for a high threshold SNR (50 dB)

In Figures 2.7 and 2.8, the auto-correlation characteristics are plotted for a low threshold SNR value of -80 dB and a high threshold SNR value of 50 dB. An NLFM phase polynomial order of $N = 6$ is chosen. In both cases, it is noticed that side-lobe levels are minimal in the proposed M-PRC-CRLB and SBnB approaches compared to the MEEV and PRC-CRLB approaches. In addition, it is also observed that the M-PRC-CRLB approach reduces the range-domain ambiguities compared to the MEEV and PRC-CRLB approaches. Further, the SBnB approach greatly reduces the side-lobe levels and range-domain ambiguities compared to all the aforementioned

Table 2.5: Effect of threshold SNR on the side-lobe levels

Threshold SNR value	**Type of waveform design approach**	**PSLR (dB)**	**ISLR (dB)**
-80 dB	MEEV	-11.44	-11.87
	PRC-CRLB	-11.78	-15.12
	M-PRC-CRLB	-11.92	-15.50
	SBnB	**-13.55**	**-16.30**
-50 dB	MEEV	-11.26	-12.90
	PRC-CRLB	-11.68	-14.52
	M-PRC-CRLB	-11.78	-13.95
	SBnB	**-12.82**	**-15.98**
-20 dB	MEEV	-10.91	-11.73
	PRC-CRLB	-11.43	-14.88
	M-PRC-CRLB	-11.66	-13.84
	SBnB	**-12.62**	**-15.84**
0 dB	MEEV	-10.73	-12.77
	PRC-CRLB	-11.29	-14.62
	M-PRC-CRLB	-11.49	-14.84
	SBnB	**-12.59**	**-15.63**
20 dB	MEEV	-10.68	-11.96
	PRC-CRLB	-11.27	-14.46
	M-PRC-CRLB	-11.27	-13.64
	SBnB	**-12.28**	**-15.57**
50 dB	MEEV	-10.40	-11.88
	PRC-CRLB	-10.84	-14.16
	M-PRC-CRLB	-11.19	-14.72
	SBnB	**-12.03**	**-15.19**

approaches. Subsequently, the auto-correlation characteristics are analyzed at various threshold SNR levels. To give more insight into the auto-correlation characteristics, the Peak-to-Side-Lobe-Ratio (PSLR) and low Integrated Side-Lobe Ratio (ISLR) (Levanon 2014) are calculated and the values are listed in Table 2.5. It is evident that in all the approaches PSLR values increase by the threshold SNR value. However, the proposed M-PRC-CRLB and SBnB approach achieves better PSLR and ISLR values compared to the MEEV and PRC-CRLB approaches. Further, in both MEEV and PRC-CRLB approaches, as the threshold SNR value increases, ISLR values fluctuate. Therefore, in both MEEV and PRC-CRLB approaches, there is no control over the side-lobe energy levels and range-domain ambiguities. Whereas in the M-PRC-CRLB approach, the side-lobe levels are minimum when compared to the MEEV and PRC-CRLB approaches. Moreover, this approach achieves a PSLR value of -11.92 dB and an ISLR value of -15.50 dB at a low threshold SNR (-80 dB). Subsequently, the M-PRC-CRLB approach yields a PSLR value of -11.19 dB and an ISLR value of -14.72 dB at a high threshold SNR (50 dB). Interestingly, it is noticed that ISLR values are slightly fluctuating at high threshold SNR values in the M-PRC-CRLB approach. Eventually, the proposed SBnB approach outperforms all the other approaches by controlling the side-lobe levels. At a lower threshold SNR value (-80 dB), the SBnB approach fulfills a PSLR value of -13.55 dB and an ISLR value of -16.30 dB. Further, at a high threshold SNR value (50 dB) a PSLR value of -12.03 dB and an ISLR value of -15.19 dB is obtained. Even at a high threshold SNR value, the SBnB approach controls the side-lobe levels significantly when compared to MEEV, PRC-CRLB, and M-PRC-CRLB approaches.

2.4.3 Effect of Order of Phase Polynomial

The impact of phase polynomial order on the radar waveform is already discussed in Section 2.3.2. To analyze the effect of polynomial order on the side-lobe levels, a comprehensive analysis is carried out on the auto-correlation characteristics. Based on the auto-correlation characteristics, the PSLR and ISLR values are estimated corresponding to different polynomial order and listed out in Table 2.6. To illustrate the effect of side-lobe levels on the auto-correlation characteristics for various approaches, the bar charts are plotted at different threshold SNR levels and they are depicted in

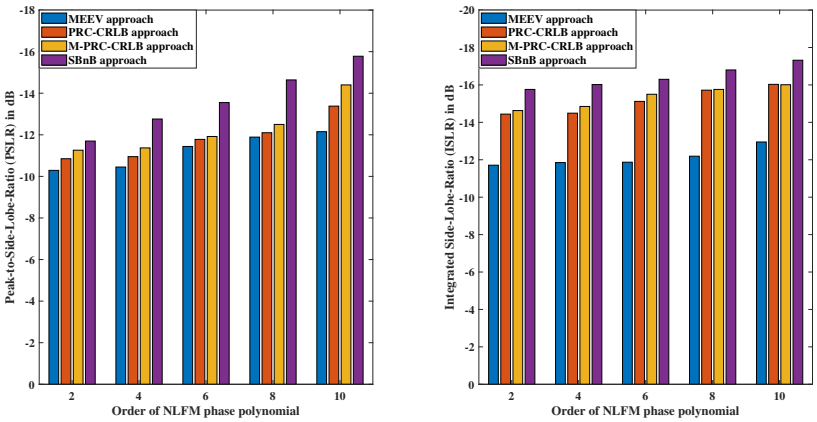

Figure 2.9: Impact of the phase polynomial order on side-lobe levels at a low threshold SNR (-80 dB)

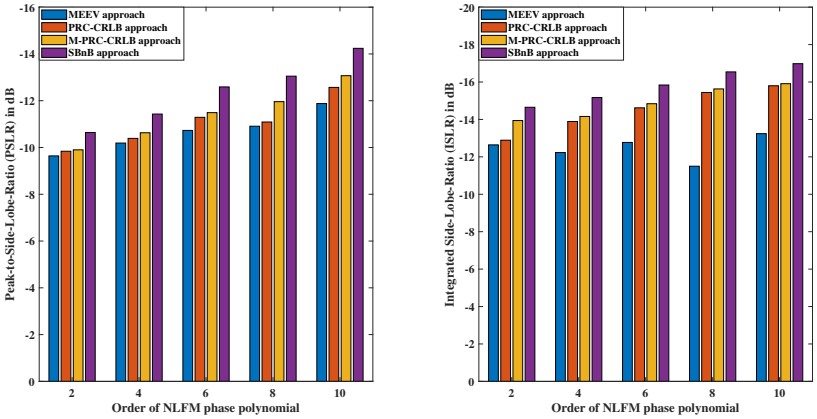

Figure 2.10: Impact of the phase polynomial order on side-lobe levels at a threshold SNR (0 dB)

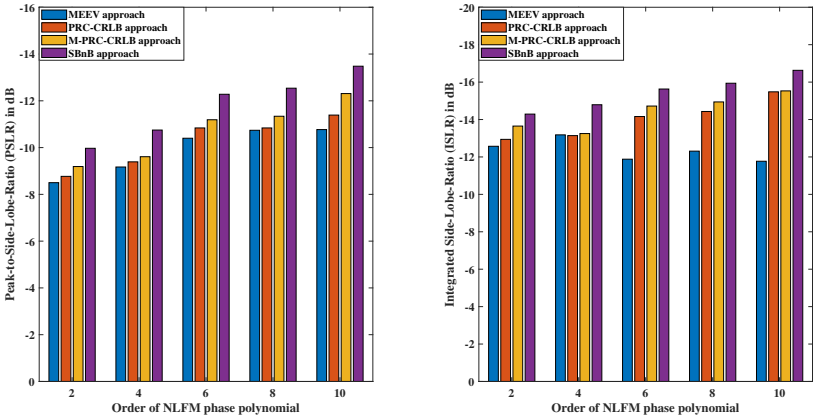

Figure 2.11: Impact of the phase polynomial order on side-lobe levels at a high threshold SNR (50 dB)

Figures 2.9–2.11. It is observed that in all the designated approaches PSLR values are gradually decreasing by the phase polynomial order. However, at various threshold

Table 2.6: Effect of phase polynomial order on the side-lobe levels

Order (N)	Type of waveform design approach	MEEV						PRC-CRLB						M-PRC-CRLB						SBnB					
	Threshold SNR (dB)	**-80**	**-50**	**-20**	**0**	**20**	**50**	**-80**	**-50**	**-20**	**0**	**20**	**50**	**-80**	**-50**	**-20**	**0**	**20**	**50**	**-80**	**-50**	**-20**	**0**	**20**	**50**
2	PSLR (dB)	-10.29	-9.83	-9.85	-9.64	-9.05	-8.5	-10.85	-10.07	-9.71	-9.84	-9.08	-8.77	-11.26	-10.08	-9.98	-9.90	-8.61	-9.19	-11.70	-10.87	-10.72	-10.64	-10.14	-9.97
	ISLR (dB)	-11.71	-11.74	-12.16	-12.64	-12.21	-12.57	-14.44	-13.35	-13.19	-12.89	-12.96	-12.94	-14.63	-14.53	-14.45	-13.94	-13.55	-13.65	-15.76	-15.11	-14.84	-14.65	-14.39	-14.29
4	PSLR (dB)	-10.45	-10.37	-10.24	-10.19	-10.07	-9.17	-10.95	-10.86	-10.81	-10.39	-9.73	-9.39	-11.37	-11.35	-10.95	-10.63	-9.82	-9.61	-12.76	-11.90	-11.79	-11.43	-11.07	-10.75
	ISLR (dB)	-11.85	-12.57	-12.21	-12.23	-12.66	-13.18	-14.49	-14.52	-14.04	-13.89	-13.71	-13.14	-14.85	-14.12	-13.84	-14.16	-13.44	-13.25	-16.02	-15.93	-15.55	-15.17	-14.93	-14.79
6	PSLR (dB)	-11.44	-11.26	-10.91	-10.73	-10.68	-10.40	-11.78	-11.68	-11.43	-11.29	-11.27	-10.84	-11.92	-11.78	-11.66	-11.49	-11.27	-11.19	-13.55	-12.82	-12.62	-12.59	-12.28	-12.03
	ISLR (dB)	-11.87	-12.90	-11.73	-12.77	-11.96	-11.88	-15.12	-14.52	-14.88	-14.62	-14.46	-14.16	-15.50	-13.95	-13.84	-14.84	-13.64	-14.72	-16.30	-15.98	-15.84	-15.63	-15.57	-15.19
8	PSLR (dB)	-11.89	-11.52	-11.25	-10.91	-10.77	-10.74	-12.10	-12.04	-11.57	-11.09	-10.97	-10.84	-12.50	-12.38	-12.07	-11.96	-11.92	-11.34	-14.64	-13.98	-13.57	-13.05	-12.97	-12.54
	ISLR (dB)	-12.19	-12.59	-12.41	-11.50	-12.46	-12.31	-15.72	-15.62	-15.55	-15.44	-14.80	-14.43	-15.76	-14.76	-14.67	-15.63	-14.04	-14.94	-16.80	-16.25	-16.12	-16.54	-15.38	-15.94
10	PSLR (dB)	-12.15	-12.12	-11.95	-11.88	-11.34	-10.77	-13.38	-13.35	-13.24	-12.57	-12.32	-11.39	-14.40	-13.31	-13.17	-13.07	-12.90	-12.31	-15.78	-15.04	-14.57	-14.24	-13.96	-13.48
	ISLR (dB)	-12.95	-12.60	-12.49	-13.24	-13.68	-11.77	-16.03	-15.38	-15.55	-15.80	-15.68	-15.48	-16.01	-15.42	-15.21	-15.91	-14.97	-15.53	-17.32	-17.18	-17.03	-16.98	-16.90	-16.63

SNR values, the proposed M-PRC-CRLB and SBnB approaches provide improved performance in PSLR values compared to the existing MEEV and PRC-CRLB approaches. From Figures 2.9–2.11, it is also noticed that in MEEV and PRC-CRLB approaches ISLR values are fluctuating by the threshold SNR values. Therefore for MEEV and PRC-CRLB approaches, there is no control over the side-lobe energy levels. Whereas in the M-PRC-CRLB approach, ISLR values are slightly improved compared to the MEEV and PRC-CRLB approaches. Further, it also controls the side-lobe energy levels compared to MEEV and PRC-CRLB approaches. Eventually, the proposed SBnB approach outperforms all the aforementioned approaches by greatly improving the PSLR and ISLR values for all polynomial orders at various threshold SNR values. Further, the SBnB approach achieves a minimum PSLR value of -15.78 dB and an ISLR value of -17.32 dB. In addition, at various phase polynomial orders i.e. N=2,4,6,8, and 10, the SBnB approach provides enhanced control over the side-lobe levels compared to MEEV, PRC-CRLB, and M-PRC-CRLB approaches.

2.4.4 Effect of Energy Constraint on the Proposed Optimization Problem

Here, the NLFM phase polynomial order is fixed at $N = 6$. Based on the SBnB algorithm, the globally optimized phase coefficients are obtained and the simulation results are plotted. Figure 2.12, shows the spectral characteristics, with reference to the optimized phase coefficients at various threshold SNR values. It is observed that only at a threshold SNR value of -20 dB the spectral energy is concentrated both at the center and edges of the bandwidth. Whereas for all the remaining threshold SNR values, the spectral energy magnitude is insignificant either at the center or at the edges of the bandwidth, which is undesired for the spectrum sharing in a CRCS.

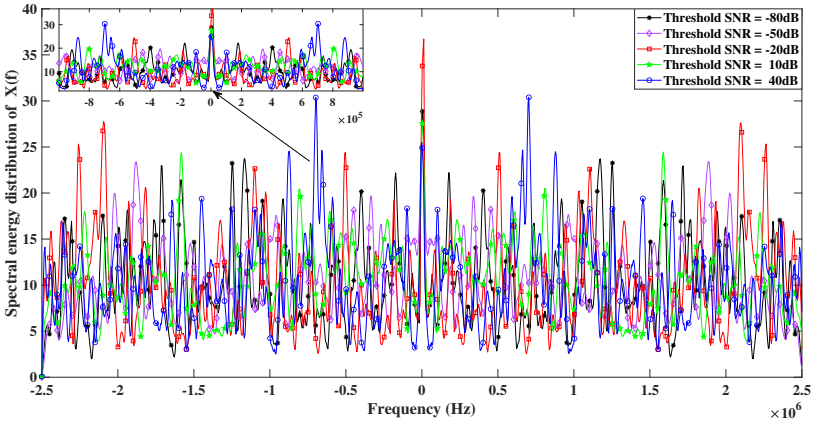

Figure 2.12: Energy constrained optimal NLFM radar waveform spectrum

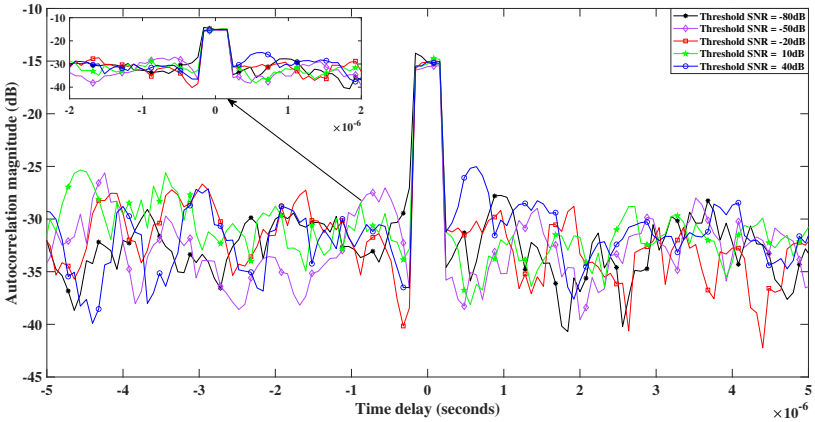

Figure 2.13: Energy constrained optimal NLFM radar waveform autocorrelation function

Table 2.7: Effect of energy constraint on the SBnB approach

Threshold SNR value	**SBnB approach (without energy constraint)**		**SBnB approach (with energy constraint)**	
	PSLR (dB)	**ISLR (dB)**	**PSLR (dB)**	**ISLR (dB)**
-80 dB	-13.55	-16.30	-12.63	-13.21
-50 dB	-12.82	-15.98	-10.09	-12.80
-20 dB	-12.62	-15.84	-11.23	-12.46
0 dB	-12.59	-15.63	-10.73	-11.54
20 dB	-12.28	-15.57	-10.09	-12.35
50 dB	-12.03	-15.19	-9.45	-12.08

As a result, the performance of both radar and communication systems may deteriorate. Besides, in Figure 2.13, the auto-correlation characteristics of the waveforms are analyzed for various threshold SNR values. In addition, to precisely investigate the auto-correlation characteristics, we computed the PSLR and ISLR values at various threshold SNR values and tabulated them in Table 2.7. Also for comparison, the PSLR and ISLR values are calculated and listed in Table 2.7, in the presence and absence of an energy constraint. It is noticed that PSLR and ISLR values fluctuate in the presence of energy constraints. Therefore, there is no control over the side-lobe levels. In the absence of energy constraint, contrary to the previous case, PSLR and ISLR values are gradually increasing in accordance with the threshold SNR value. Thus, there is noticeable control over the side-lobe levels in the absence of energy constraints. Due to this reason, energy constraint is ignored while computing radar estimation rate and communication data rate.

2.4.5 Performance Analysis of Designated Optimum Radar Waveform Design Approaches

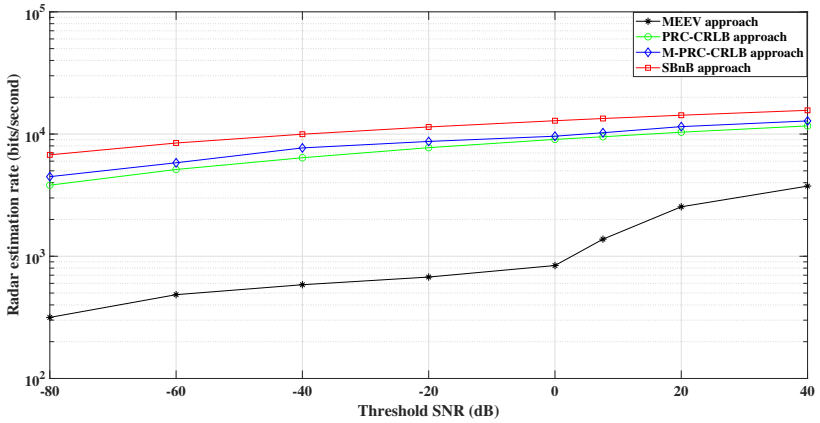

Figure 2.14: Radar estimation rate versus threshold SNR

To carry out the performance evaluation, firstly the proposed optimization problem is solved at various threshold SNR values to evaluate the optimized phase coefficients for a phase polynomial order $N = 6$. Based on the optimized coefficients, the radar estimation rate and communication data rate are computed. With reference to the computed estimation rate and communication data rate, the simulated results are plotted. From Figure 2.14, it is observed that the radar estimation rate

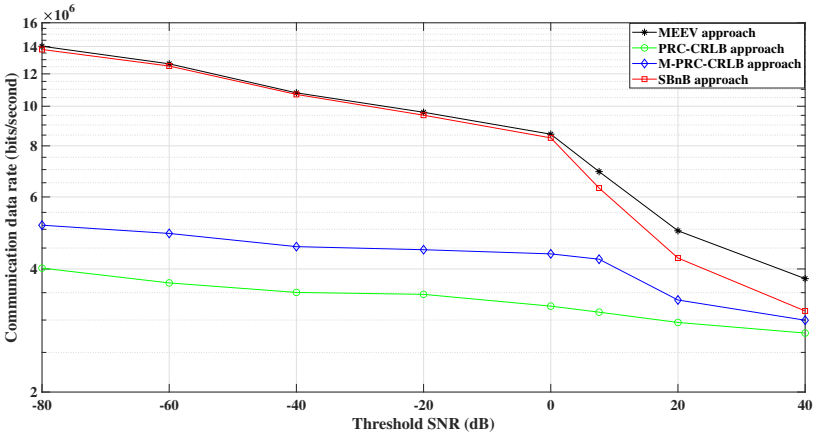

Figure 2.15: Communication data rate versus threshold SNR

Table 2.8: Performance analysis of various optimum waveform design approaches

Optimum Waveform Design Approach	**Radar estimation rate**	**Communication data rate**
Spectral-Mask shaping	1.06 kbps	0.013 Mbps
Minimum Estimation Error Variance (MEEV)	1.38 kbps	6.92 Mbps
PRC-CRLB	9.5 kbps	3.13 Mbps
M-PRC-CRLB	10.2 kbps	4.20 Mbps
Spatial Branch and Bound	**13.4 kbps**	**6.30 Mbps**

gradually increases in accordance with the threshold SNR value for all the designated waveform design approaches. This is because the CRLB is inversely proportional to the threshold SNR value. Primarily, the proposed M-PRC-CRLB approach improves the radar estimation rate compared to MEEV and PRC-CRLB approaches at various threshold SNR values. Subsequently, the proposed SBnB approach outperforms the MEEV, PRC-CRLB, and M-PRC-CRLB approaches in terms of radar estimation rate. From Figure 2.15, it is evident that the data rate of the communication system gradually decreases as the threshold SNR increases in all the designated waveform design approaches. This is because, the residual noise power spectral density increases in accordance with the threshold SNR, which affects the communication system performance. It is also evident that the SBnB approach outperforms PRC-CRLB and M-PRC-CRLB approaches in terms of communication data rate. However, the SBnB

approach achieves a comparable communication data rate as achieved in the MEEV approach. Interestingly, in the proposed SBnB approach, it is witnessed that there is a drastic fall in the communication data rate at high threshold SNR values.

In addition, the performance comparison of the proposed methods against various existing optimum waveform design methods like spectral mask shaping method (Paul et al. 2016), minimum estimation error variance method (Chiriyath et al. 2019), and PRC-CRLB method (Mahipathi et al. 2021) is elucidated in Table 2.8. For this comparison, an NLFM phase polynomial order fixed at $N = 6$, and a threshold SNR value of 7.6 dB and conducted a Monte-Carlo simulation with 100 runs to optimize the phase coefficients and thereby calculated the radar estimation rate and communication data rate. From Table 2.8, it is evident that the proposed M-PRC-CRLB approach achieves a radar estimation rate of 10.2 kbps and a communication data rate of 4.20 Mbps. Hence, the M-PRC-CRLB approach performs better compared to the MEEV and PRC-CRLB approaches in terms of radar estimation rate. However, this approach is unable to uphold the communication data rate, which was achieved by the MEEV approach. The proposed SBnB approach achieves a radar estimation rate of 13.4 kbps and a communication data rate of 6.30 Mbps. Hence, the SBnB approach outperforms MEEV, PRC-CRLB, and M-PRC-CRLB approaches in terms of radar estimation rate. However, the proposed SBnB approach almost upholds the same communication data rate, which was achieved in the MEEV approach. Therefore, the proposed SBnB approach significantly improves the radar estimation rate at a comparable performance of communication data rate.

2.4.6 Waveform Analysis Using Ambiguity Function

To perform the waveform analysis based on the ambiguity function, for all the proposed and existing optimal waveform design approaches, 3-D ambiguity surfaces are plotted and are depicted in Figures 2.16 and 2.17. Based on the ambiguity surfaces, PSLR values at non-zero Doppler are estimated and tabulated in Table 2.9. At a low threshold SNR value (-80 dB), the proposed SBnB and M-PRC-CRLB approach provides a slightly improved PSLR value compared to the existing MEEV and PRC-CRLB approaches. As observed in Table 2.7, PSLR values gradually increase by the threshold SNR value. Even the same is observed in Table 2.9. Further, even at a

Table 2.9: Comparison of PSLR values of various waveform design approaches using ambiguity function

Type of waveform design approach	**Low threshold SNR (-80 dB)**	**High threshold SNR (50 dB)**
	PSLR (dB)	**PSLR (dB)**
MEEV	-17.83	-15.78
PRC-CRLB	-18.32	-17.60
M-PRC-CRLB	-18.47	-17.21
SBnB	**-18.57**	**-16.84**

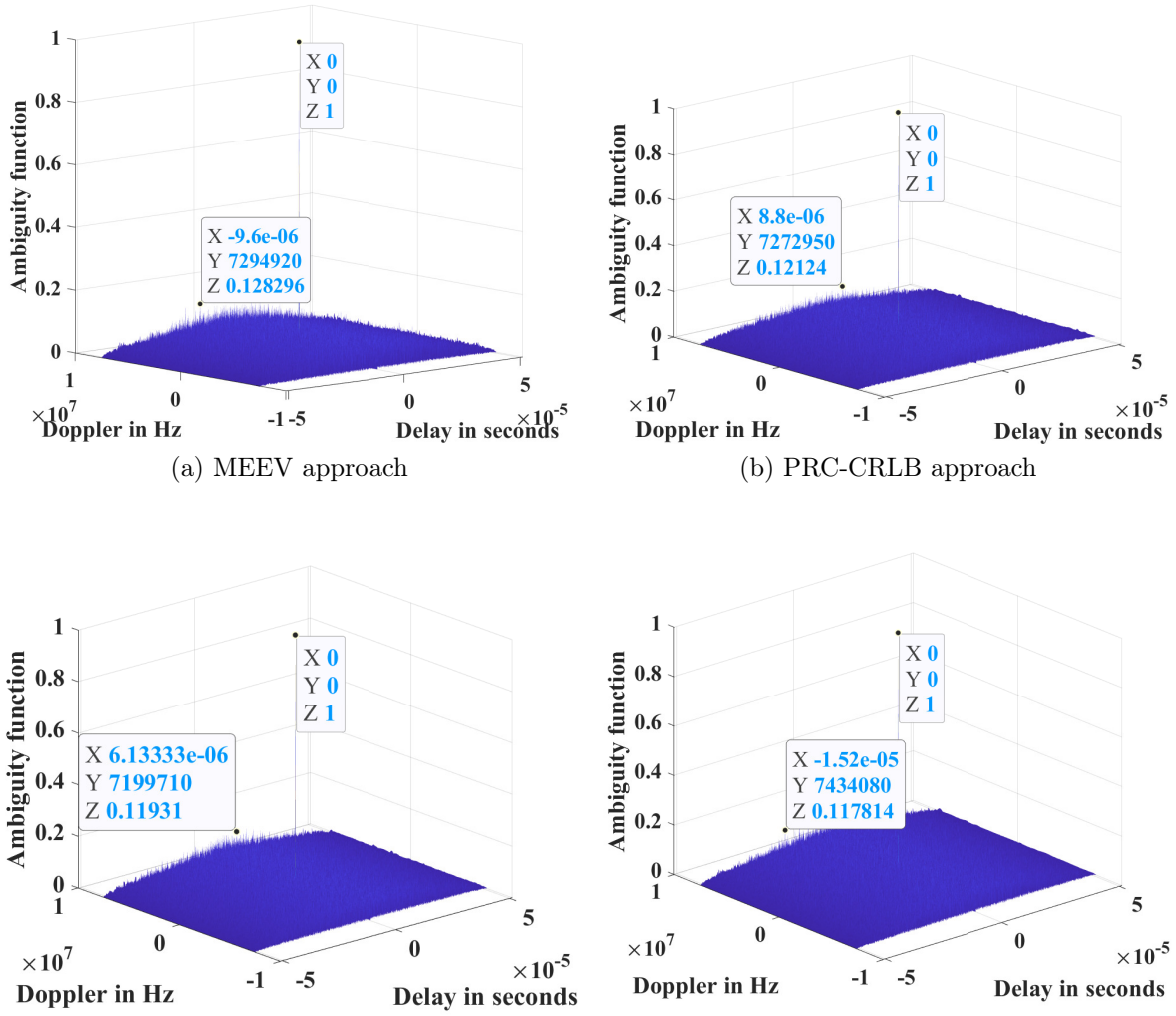

(a) MEEV approach

(b) PRC-CRLB approach

(c) M-PRC-CRLB approach

(d) SBnB approach

Figure 2.16: Ambiguity surface plot with a phase polynomial order (N=6) and a low threshold SNR (-80 dB)

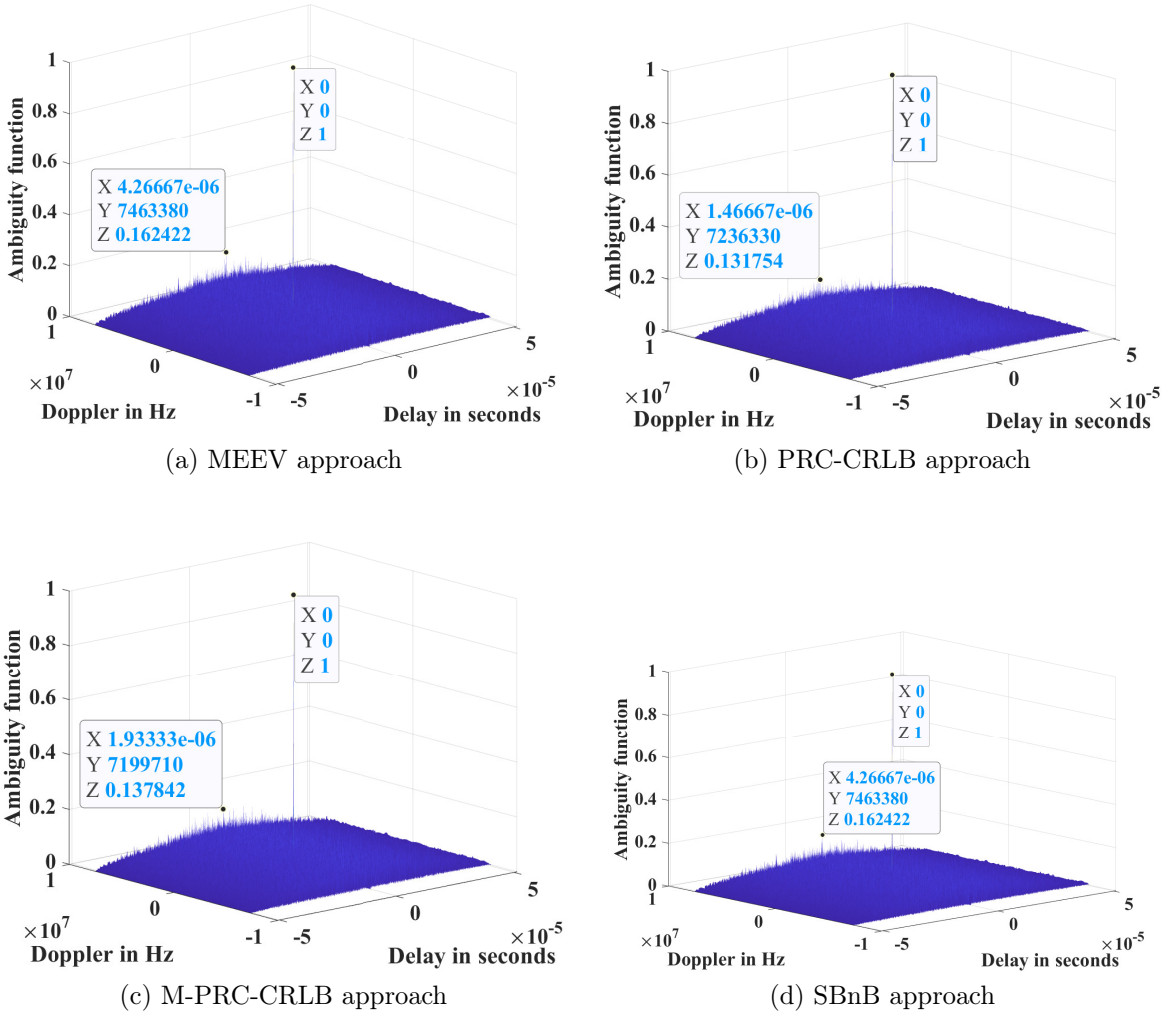

(a) MEEV approach

(b) PRC-CRLB approach

(c) M-PRC-CRLB approach

(d) SBnB approach

Figure 2.17: Ambiguity surface plot with a phase polynomial order (N=6) and a high threshold SNR (50 dB)

high threshold SNR value (50 dB), the proposed approaches provide relatively good PSLR values. However, the ambiguous surface plots for various approaches show almost similar performance with an insignificant difference in the PSLR values. The ambiguity surface plots (Figures 2.16 and 2.17) illustrate the basic idea of how all these approaches (MEEV, PRC-CRLB, M-PRC-CRLB, and SBnB) perform in the Doppler domain. To provide an exact analysis of the proposed approaches, additional Doppler performance evaluation can be implemented for all polynomial orders at various threshold SNR values using the ISLR metric. This might be carried out as future work.

2.5 Summary

This chapter proposed a local optimization approach i.e., M-PRC-CRLB, and a global optimization approach i.e., SBnB to optimize an NLFM radar waveform for improving the performance of a radar system in a CRCS environment. Further, a comparable communication data rate is achieved in a CRCS configuration. However, the proposed SBnB approach faces the problem of computational complexity. Hence one can continue this work to minimize the computational complexity. Subsequently, Chapter 3 demonstrates the importance of optimal waveform selection for enhancing the target tracking performance in a CRCS.

Chapter 3

Optimum Waveform Selection for Target State Estimation in a CRCS

This chapter introduces a novel measurement model based on the communication residual component for various radar waveforms to characterize the radar sensor behaviour in a CRCS environment. Further, with reference to the sensor characterization, the Kalman Filter (KF) is considered to estimate the target trajectory for all the designated radar waveforms in the CRCS configuration.

3.1 Problem Formulation

Figure 3.1 depicts the Cooperative Radar-Communication System (CRCS) framework, where the Joint Radar-Communication (JRC) node is capable of detecting the radar target and acting as a communication receiver. The JRC node uses the same spectral band and coverage area for sensing and communication purposes. Further, the radar-sensor system receives the communication signal information. Based on information theory, radar signal estimation always tries to reduce uncertainty in the channel, and the channel information is passed to the wireless communication system (Chiriyath 2018). Therefore, the radar and the communication systems are cooperative with each other. Further, to perceive the cooperation between radar and communication systems, the standard performance limits of the CRCS system are examined in (Bliss 2014) and (Chiriyath et al. 2016c).

In general, the radar and communication systems have distinct waveform requirements (Chiriyath et al. 2019). Therefore, the proposed waveform selection approach has considered that radar and communication systems use separate waveforms for

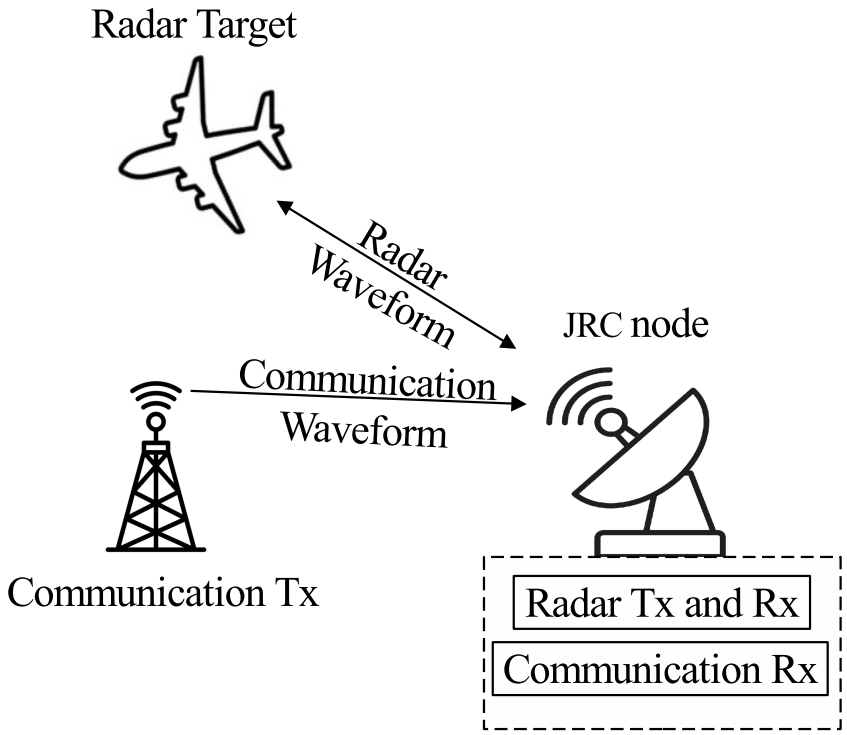

Figure 3.1: Cooperative radar-communication system model

transmission, and a radar-centric approach (Aubry et al. 2016a) has been considered in the current scenario. The overall received signal at the JRC node is provided by,

$$y(t) = s_{rad}(t - \tau) + s_{com}(t) + n(t), \tag{3.1}$$

where $s_{rad}(t - \tau)$ represents the radar target return, $s_{com}(t)$ indicates the received communication signal, and $n(t)$ represents thermal noise present in the receiver. Here, τ indicates the round trip time delay and is given by,

$$\tau = \frac{2R}{c}, \tag{3.2}$$

here, c signifies the light velocity and R represents the distance of the target from the radar sensor. Further, it is assumed that the JRC node uses the successive interference cancellation (SIC) receiver model (Bliss 2014), which combats the mutual interference among wireless communication and radar sensing systems. However, the performance of the SIC receiver model is super sensitive to model-mismatch errors (Chiriyath et al. 2019). In addition, they bring in higher residual components, which badly affects the interference-cancellation process. The likely sources for model mismatch

errors are phase noise and dynamic range constraints on the receiver. In this work, we concentrated on how phase noise solely influences the CRCS performance. A detailed analysis of the interconnection between phase noise and the SIC receiver is presented in (Chiriyath et al. 2016a).

In the SIC receiver model, it is assumed that subject to prior observations, the round trip time delay of the radar system can be predicted. Utilizing this knowledge, the predicted target return is generated and it is suppressed from the joint radar-communication signal. Once the radar signal is predicted, the JRC node will decode the communication symbols (Chiriyath et al. 2019). However, due to phase noise, there is a variation between the received communication signal and the decoded communication signal, adding a residual component to the radar return. Hence, in the presence of communication residual, the JRC node extracts radar target information from the joint received signal (3.1). Therefore, the affected received signal at the JRC node from a radar sensor perspective is provided by,

$$y(t) = s_{rad}(t-\tau) + s_{com}^{resi}(t) + n(t), \tag{3.3}$$

with reference to (Bliss 2014), the communication residual component ($s_{com}^{resi}(t)$) is given by,

$$\begin{aligned} s_{com}^{resi}(t) &= s_{com}(t) - s_{com}^{decoded}(t) \\ &= \frac{\partial s_{com}(t)}{\partial t} n_{\tau,\text{proc}}, \end{aligned} \tag{3.4}$$

here, $s_{com}^{resi}(t) + n(t)$ represents the sum of communication residual and thermal noise components, $s_{com}(t)$ represents the received communication signal, $s_{com}^{decoded}(t)$ represents the decoded communication signal, and $n_{\tau,\text{proc}}$ represents the process noise having variance ($\sigma^2_{\tau,\text{proc}}$). It is considered that the thermal noise is an additive white bandpass Gaussian noise having a spectral height $N_0/2$. Further, to obtain valid inferences from the residual component, it should follow a Gaussian distribution (Xie et al. 2017). Here, we assume the spectral height of the residual communication component as $N_r/2$. In addition, in (3.3), the $s_{rad}(t-\tau)$ represents the baseband envelope owing to target return and is provided by

$$s_{rad}(t-\tau) = \sqrt{E_R} e^{j\Phi} \tilde{x}(t-\tau) e^{jv_0 t}, \tag{3.5}$$

here, E_R represents the energy of the target return , Φ represents the random phase shift, $\tilde{x}(t)$ represents the transmitted signal envelope, υ_0 represents the Doppler frequency shift, and τ indicates the target delay. The normalized communication residual spectral density is given by Chiriyath et al. [2019],

$$N_r(f) = \left(4\pi^2\right) \|b\|^2 P_{comm}\ \eta_0 {\sigma_f}^2 \|S_{com}(f)\|^2 f^2, \tag{3.6}$$

here b represents overall communication channel gain, P_{comm} denotes the transmitted communication signal power, η_0 signifies the phase noise spectral density, σ_f represents the process noise variance, $S_{com}(f)$ represents the spectrum of received communication signal component, and f is the frequency.

subsequently, the thermal noise spectral density is expressed as,

$$N_0(f) = K_B T_K \Pi_B(f), \tag{3.7}$$

here, K_B represents the Boltzmann constant, T_K represents temperature in Kelvin degree and $\Pi_B(f)$ represents the rectangular spectrum. Based on above equations (3.6) and (3.7), thermal noise power (N_0), and communication residual signal power (N_r) are evaluated.

The radar sensor should do signal processing during the intra-pulse time slot of the received pulse (Kershaw and Evans 1994). In general, the radar sensor estimates the target position and target velocity. The radar tracker should perform information processing during the inter-pulse time slot of the received pulse (Kershaw and Evans 1994). Of course, there is an indirect connection between radar sensor measurement and tracking. However, the quality of a radar sensor measurement mainly depends on waveform selection. Thus, the target tracking performance relies on optimal waveform selection. In this regard, in our work, firstly we derived the measurement noise covariance matrix ($\mathbf{N}(\mathbf{\Theta_k})$) for various waveforms to test the quality of measurement. Further, we applied the Kalman filter to obtain a single target track using these measurements with RMSE as a metric to accomplish enhanced radar target tracking performance for both range and range rate.

With reference to (Kershaw and Evans 1994), the proposed tracking framework is represented in Figure 3.2(a). It is observed that the radar sensor contains both a transmitter, a receiver, and an optimal receiver sub-section for better detector performance. Here, the signal processor performs pulse compression and Doppler processing

to improve the range resolution (Richards et al. 2010). Subsequently, the optimal detector selects the appropriate threshold level to accomplish the best possible detection probability of a target. Further, the tracking filter estimates the target position and velocity based on the measurements. In addition, a feedback loop is present in Figure 3.2(a) signifies the dependency of target tracking on waveform optimization. Furthermore, it also provides information regarding the selection of the next transmitted waveform in accordance with the tracker requirement. Moreover, the detailed idea of the waveform selection process is shown in Figure 3.2(b).

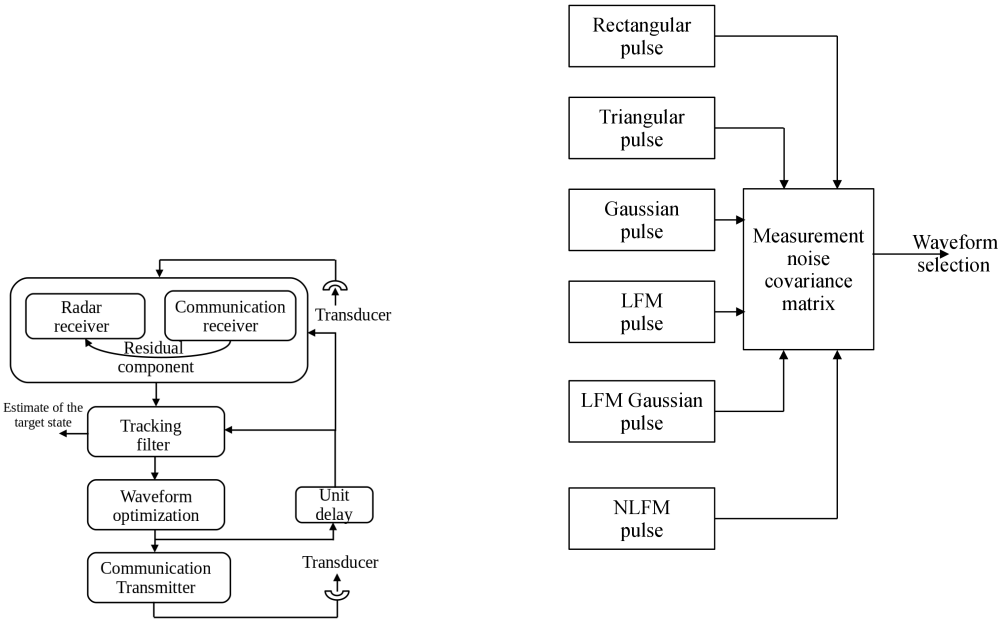

(a) Proposed target tracking framework (b) Waveform selection strategy

Figure 3.2: Optimal waveform selection based on tracking scenario

3.2 Radar Sensor Characterization

The characterization of a radar sensor mainly relies on knowledge of the measurement noise covariance matrix ($\mathbf{N}(\mathbf{\Theta_k})$) (Kershaw and Evans 1994). Further, it is a waveform-dependent non-linear function of the waveform parameter vector ($\mathbf{\Theta_k}$). Here, $\mathbf{\Theta_k}$ provides the information regarding the received waveform parameters of the designated waveform at the time instant $\mathbf{k}$. The measurement noise covariance matrix obtains the relation between waveform parameter vector $\mathbf{\Theta}_k$ and the covariance

matrix of the noisy observations ($\mathbf{N}(\mathbf{\Theta_k})$) as derived in (Kershaw and Evans 1994) and it is expressed as,

$$\mathrm{E}[(\mathbf{y}-\bar{\mathbf{y}})(\mathbf{y}-\bar{\mathbf{y}})^T] = \mathbf{N}(\mathbf{\Theta_k}) = \mathbf{T}\mathbf{J}^{-1}\mathbf{T}^T, \tag{3.8}$$

here $\mathbf{y} = \mathbf{T}\alpha$, $\mathbf{y}$ represents the measurement vector of the tracking system and it is formed based on a range (r) and range-rate ($\dot{r}$) i.e., $\mathbf{y} = [r \;\; \dot{r}]^T$. Subsequently, $\bar{\mathbf{y}}$ represents the mean of the measurement vector $\mathbf{y}$. Whereas, α represents the receiver estimation parameter vector and it is formed based on the received signal vector i.e., $\alpha = [\tau \;\; \omega]^T$. Here τ is the time delay and ω represents the Doppler frequency. Further, $\mathbf{T}$ is the transformation matrix and it is given by Sira et al. [2004], $\mathbf{T} = \mathrm{diag}\,(c/2, c/\,(2\omega_c))$. Here c represents the waveform propagation velocity and ω_c is the carrier frequency. $\mathbf{J}$ represents the Fisher information matrix. From (3.8), it is evident that Fisher's information matrix needs to be evaluated to find the measurement noise covariance matrix($\mathbf{N}(\mathbf{\Theta_k})$).

A Calculation of Fisher Information Matrix (J)

In general, the Fisher information matrix is represented as,

$$\begin{bmatrix} J_{11} & J_{12} \\ J_{21} & J_{22} \end{bmatrix} \tag{3.9}$$

According to the parameters of interest (τ and ω), the Fisher information matrix elements are defined as,

$$J_{11} = -\mathrm{E}[\frac{\partial^2}{\partial\tau^2}\ln\Lambda\,(\tau,\omega)] \tag{3.10}$$

$$J_{22} = -\mathrm{E}[\frac{\partial^2}{\partial\omega^2}\ln\Lambda\,(\tau,\omega)] \tag{3.11}$$

$$J_{12} = J_{21} = -\mathrm{E}[\frac{\partial^2}{\partial\tau\partial\omega}\ln\Lambda\,(\tau,\omega)] \tag{3.12}$$

Firstly, it is necessary to determine the log-likelihood function to obtain elements of the Fisher information matrix. According to Trees [1971], the log-likelihood function corresponding to the received signal (3.3) at the JRC node is evaluated as,

$$\ln\Lambda\,(\tau,\omega) = \frac{1}{N_0+N_r}\frac{\bar{E}_r}{\bar{E}_r+N_0+N_r}\left\{|L(\tau,\omega)|^2\right\}, \tag{3.13}$$

here,

$$L(\tau,\omega)=\int_{\infty}^{\infty}y(t)\tilde{x}^{*}(t-\tau)\exp^{-j\omega t}\,dt \tag{3.14}$$

from (3.13),

$$\frac{\partial\ln\Lambda(\tau,\omega)}{\partial\tau}=K'\left[L(\tau,\omega)\frac{\partial L^{*}(\tau,\omega)}{\partial\tau}+\frac{\partial L(\tau,\omega)}{\partial\tau}L^{*}(\tau,\omega)\right],$$

$$=2K'\,\mathrm{Re}\left[L(\bar{\tau},\omega)\frac{\partial L^{*}(\tau,\omega)}{\partial\tau}\right] \tag{3.15}$$

here,

$$K'\triangleq\frac{1}{N_0+N_r}\frac{\bar{E}_r}{\bar{E}_r+N_0+N_r} \tag{3.16}$$

subsequently, the following derivatives are required to evaluate the Fisher information matrix ($\mathbf{J}$),

$$\frac{\partial^2\ln\Lambda(\tau,\omega)}{\partial\tau^2}=2K'\,\mathrm{Re}\left[\frac{\partial L(\tau,\omega)}{\partial\tau}\cdot\frac{\partial L^{*}(\tau,\omega)}{\partial\tau}+L(\tau,\omega)\frac{\partial^2 L^{*}(\tau,\omega)}{\partial\tau^2}\right] \tag{3.17}$$

$$\frac{\partial^2\ln\Lambda(\tau,\omega)}{\partial\tau\partial\omega}=2K'\,\mathrm{Re}\left[\frac{\partial L(\tau,\omega)}{\partial\omega}\cdot\frac{\partial L^{*}(\tau,\omega)}{\partial\tau}+L(\tau,\omega)\frac{\partial^2 L^{*}(\tau,\omega)}{\partial\tau\partial\omega}\right] \tag{3.18}$$

$$\frac{\partial^2\ln\Lambda(\tau,\omega)}{\partial\omega^2}=2K'\,\mathrm{Re}\left[\frac{\partial L(\tau,\omega)}{\partial\omega}\frac{\partial L^{*}(\tau,\omega)}{\partial\omega}+L(\tau,\omega)\frac{\partial^2 L^{*}(\tau,\omega)}{\partial\omega^2}\right] \tag{3.19}$$

$$J_{11}=-E\left\{\frac{\partial^2\ln\Lambda(\tau,\omega)}{\partial\tau^2}\right\} \tag{3.20}$$

$$\begin{aligned}&=-2K'\left\{\int_{-\infty}^{\infty}\frac{\partial\tilde{x}^{*}(t-\tau)}{\partial\tau}\frac{\partial\tilde{x}(u-\tau)}{\partial\tau}e^{jw(t-u)}E\left[y(t)y^{*}(u)\right]dtdu\right.\\&\quad\left.+\iint_{-\infty}^{\infty}\tilde{x}^{*}(t-\tau)\frac{\partial^2 x(u-\tau)}{\partial\tau^2}e^{jw(t-u)}E\left[y(t)y^{*}(u)\right]dtdu\right\}.\end{aligned} \tag{3.21}$$

The correlation of $y(t)$ is,

$$E[y(t)y^{*}(u)]=E_r\tilde{x}(t-\tau)\tilde{x}^{*}(u-\tau)e^{jw(t-u)}+N_0\delta(t-u)+N_R\delta(t-u) \tag{3.22}$$

$$\begin{aligned}J_{11}=&-2Z'\left\{\bar{E}_r\left|\int_{-\infty}^{\infty}\frac{\partial\tilde{x}(t-\tau)}{\partial t}\tilde{x}^{*}(t-\tau)dt\right|^2+N_0\int_{-\infty}^{\infty}\left|\frac{\partial\tilde{x}(t-\tau)}{\partial t}\right|^2dt\right.\\&+\mathrm{Re}\left[\bar{E}_r\int_{-\infty}^{\infty}|\tilde{x}(t-\tau)|^2dt\int_{-\infty}^{\infty}\frac{\partial^2\tilde{x}^{*}(u-\tau)}{\partial\tau^2}\tilde{x}(u-\tau)du\right]+\mathrm{Re}\left[N_0\int_{-\infty}^{\infty}\tilde{x}(t-\tau)\frac{\partial^2\tilde{x}^{*}(t-\tau)}{\partial\tau^2}dt\right]\\&\left.+N_r\int_{\infty}^{\infty}\left|\frac{\partial\tilde{x}(t-\tau)}{\partial t}\right|^2dt+\mathrm{Re}\left[N_r\int_{-\infty}^{\infty}\tilde{x}(t-\tau)\frac{\partial^2\tilde{x}^{*}(t-\tau)}{\partial\tau^2}dt\right]\right\},\end{aligned} \tag{3.23}$$

here Re represents the real part of this signal component. we further simplify the above equation by considering the following:

$$\int_{-\infty}^{\infty} |\tilde{x}(t-\tau)|^2 dt = 1, \tag{3.24}$$

it is known that the waveform energy does not rely on the delay. So differentiating (3.24) with respect to τ, then

$$\mathrm{Re}\left\{\int_{-\infty}^{\infty}\left[\frac{\partial\tilde{x}(t-\tau)}{\partial\tau}\tilde{x}^*(t-\tau)\right]dt\right\} = 0, \tag{3.25}$$

we again differentiate the above equation, then

$$\mathrm{Re}\left\{\int_{-\infty}^{\infty}\left(\frac{\partial^2\tilde{x}(t-\tau)}{\partial\tau^2}\tilde{x}^*(t-\tau) + \frac{\partial\tilde{x}(t-\tau)}{\partial\tau}\frac{\partial\tilde{x}^*(t-\tau)}{\partial\tau}\right)dt\right\} = 0, \tag{3.26}$$

hence,

$$\mathrm{Re}\left[\int_{-\infty}^{\infty}\frac{\partial^2\tilde{x}^*(t-\tau)}{\partial\tau^2}\tilde{x}(t-\tau)dt\right] = -\int_{-\infty}^{\infty}\left|\frac{\partial\tilde{x}(t-\tau)}{\partial\tau}\right|^2 dt \tag{3.27}$$

Hence, from (3.23) second term, fourth term, and fifth term, the sixth term cancels each other. Further based on Parseval's theorem, the first term represents $\overline{\omega}^2$, and the third term represents $\overline{\omega^2}$. With reference to the above results,

$$J_{11} = 2K'\bar{E}_r\left[\overline{\omega^2} - (\bar{\omega})^2\right] \tag{3.28}$$

In the same way, the remaining fisher information matrix elements are evaluated. Moreover, the derivation of J_{12} and J_{21} is identical. Similarly,

$$J_{12} = J_{21} = 2K'\bar{E}_r\left[\overline{\omega t} - \bar{\omega}\bar{t}\right] \tag{3.29}$$

$$J_{22} = 2K'\bar{E}_r\left[\overline{t^2} - (\bar{t})^2\right] \tag{3.30}$$

Finally, the fisher information matrix for a given received signal is provided by,

$$\mathbf{J} = \frac{2\bar{E}_r}{N_0+N_r}\left(\begin{array}{c}\frac{\bar{E}_r}{\bar{E}_r+N_0+N_r}\end{array}\right)\left[\begin{array}{cc}\overline{\omega^2}-(\bar{\omega})^2 & \overline{\omega t}-\bar{\omega}\bar{t}\\ \overline{\omega t}-\bar{\omega}\bar{t} & \overline{t^2}-(\bar{t})^2\end{array}\right] \tag{3.31}$$

In general, meantime and mean frequency is equivalent to zero. Any time-domain waveform ensures symmetry to the origin by considering the mean as zero. Further, a zero-mean frequency indicates the transmitted waveform envelope has zero carrier frequency. Thus above equation (3.31) is modified as,

$$\mathbf{J} = \frac{2\bar{E}_r}{N_0+N_r}\left(\begin{array}{c}\frac{\bar{E}_r}{\bar{E}_r+N_0+N_r}\end{array}\right)\left[\begin{array}{cc}\overline{\omega^2} & \overline{\omega t}\\ \overline{\omega t} & \overline{t^2}\end{array}\right] \tag{3.32}$$

Further, the contribution of the waveform parameter vector and the contribution of signal-to-residual noise ratio (γ) can be isolated. Hence, the Fisher information matrix ($\mathbf{J}$) is expressed as,

$$\mathbf{J} = \gamma\, U(\Theta_k) \tag{3.33}$$

Here $\gamma = \frac{2\bar{E}_r}{N_0+N_r}\left(\frac{\bar{E}_r}{\bar{E}_r+N_0+N_r}\right)$ and $\mathbf{U(\Theta_k)} = \begin{bmatrix} \overline{\omega^2} & \overline{\omega t} \\ \overline{\omega t} & \overline{t^2} \end{bmatrix}$ with reference to (3.33), the measurement noise covariance matrix is modified as,

$$\mathbf{N(\Theta_k)} = \frac{1}{\gamma}\mathbf{T}\mathbf{U}(\mathbf{\Theta_k})^{-\mathbf{1}}\mathbf{T}^T \tag{3.34}$$

B Calculation of $\mathbf{N(\Theta_k)}$ for Designated Waveforms

In this section, the following designated waveforms are considered to evaluate the measurement noise covariance matrix. Further, it is assumed that mean time ($\bar{t}$) and mean frequency ($\bar{\omega}$) are zero for the waveform envelope of the transmitter Trees [1971]. As anticipated, $\overline{\omega t} = 0$ for pure amplitude modulated waveforms as it quantifies the amount of frequency modulation in the pulse signal Helstrom [1966].

1) *Continuous Wave – Rectangular Pulse*

Let $\tilde{x}(t)$ be a rectangular pulse waveform and it is provided by,

$$\tilde{x}(t) = \begin{cases} \frac{1}{\sqrt{T}}, & -\frac{\tau}{2} < t < \frac{\tau}{2} \\ 0, & \text{elsewhere.} \end{cases} \tag{3.35}$$

$$|\tilde{X}(\omega)| = \frac{2}{\sqrt{\tau}\omega}\sin(\frac{\omega\tau}{2}) \tag{3.36}$$

$$\overline{\omega^2} = \frac{4\pi B_1}{\tau}, \quad \overline{t^2} = \frac{\tau^2}{12}, \quad \overline{\omega t} = 0 \tag{3.37}$$

$$\mathbf{N(\Theta_k)} = \begin{bmatrix} \frac{c^2\tau}{16\gamma\pi B_1} & 0 \\ 0 & \frac{3c^2}{\gamma\tau^2\omega_c{}^2} \end{bmatrix} \tag{3.38}$$

Further, $|\mathbf{N(\Theta_k)}| = \frac{3c^4}{16\gamma^2\pi B_1\tau\omega_c{}^2}$. Here $|[\cdot]|$ represents the determinant of a matrix. It is evident from the expression that, by maintaining a high signal-to-residual noise ratio (γ) value the measurement noise covariance can be reduced.

2) *Continuous Wave – Triangular Pulse*

An analog triangular pulse waveform is represented as,

$$\tilde{x}(t) = \begin{cases} \sqrt{\frac{3}{2\tau}}\left(1 - \frac{|t|}{\tau}\right) & -\tau < t < \tau \\ 0 & \text{otherwise} \end{cases} \tag{3.39}$$

$$\tilde{X}(\omega) = \sqrt{\frac{3\tau}{2}}\,\mathrm{sinc}^2\left(\frac{\omega\lambda}{2}\right) \tag{3.40}$$

$$\overline{\omega^2} = 3/\tau^2, \quad \overline{t^2} = \tau^2/10, \quad \overline{\omega t} = 0 \tag{3.41}$$

$$\mathbf{N}(\mathbf{\Theta_k}) = \begin{bmatrix} \frac{c^2\tau^2}{12\gamma} & 0 \\ 0 & \frac{5c^2}{2\omega_c^2\tau^2\gamma} \end{bmatrix} \tag{3.42}$$

Further, $|\mathbf{N}(\mathbf{\Theta_k})| = \frac{5c^4}{24\gamma^2{\omega_c}^2}$. It is evident from the expression that, by maintaining a high signal-to-residual noise ratio (γ) value the measurement noise covariance can be minimized.

3) *Continuous Wave – Gaussian Pulse*

A Gaussian pulse often obeys a handy analytic idealization and it is represented as,

$$\tilde{x}(t) = \left(\frac{1}{\pi\tau^2}\right)^{1/4} \exp\left(\frac{-t^2}{2\tau^2}\right) \tag{3.43}$$

$$\tilde{X}(\omega) = \left(4\pi\tau^2\right)^{1/4} \exp\left(\frac{-\omega^2\tau^2}{2}\right) \tag{3.44}$$

$$\overline{\omega^2} = 1/2\tau^2, \quad \overline{t^2} = \tau^2/2, \quad \overline{\omega t} = 0 \tag{3.45}$$

$$\mathbf{N}(\mathbf{\Theta_k}) = \begin{bmatrix} \frac{c^2\tau^2}{2\gamma} & 0 \\ 0 & \frac{c^2}{2\omega_c^2\tau^2\gamma} \end{bmatrix} \tag{3.46}$$

Further, $|\mathbf{N}(\mathbf{\Theta_k})| = \frac{c^4}{4\gamma^2{\omega_c}^2}$. It is evident from the expression that, by maintaining a high signal-to-residual noise ratio (γ) value the measurement noise covariance can be reduced.

In a nutshell, for the above-selected amplitude-modulated waveforms, the selection of optimized waveform parameter vector (Θ_k) is provided by the following objective function,

$$\begin{aligned} &\underset{\mathbf{\Theta_k}}{\text{minimize}} \quad |\mathbf{N}(\mathbf{\Theta_k})| \\ &\text{subject to} \quad \gamma_{max}, \end{aligned} \tag{3.47}$$

here $\mathbf{\Theta_k}$ represents the received waveform parameter vector at the time instant k. Further, the maximized signal-to-residual noise ratio (γ_{max}) is the waveform constraint (tunable waveform parameter) in all the designated amplitude-modulated waveforms. Furthermore, by controlling the measurement noise covariance the radar target state estimation performance may be improved in the CRCS.

4) $LFM - Pulse$

A linear frequency-modulated pulse waveform is suitable for pulse compression to achieve high-range resolution. Mathematically, it is given by,

$$\tilde{x}(t) = A_1 \cos\left(\pi \frac{B_1}{\tau} t^2\right) \quad -\frac{\tau}{2} \leq t \leq \frac{\tau}{2}, \tag{3.48}$$

here, A_1 represents the amplitude of the waveform, B_1 represents the waveform bandwidth, and τ indicates the pulse duration.

$$\tilde{X}(\omega) \approx |\tilde{X}(\omega)| \exp\left(-j \frac{1}{4\pi} \frac{\tau}{B_1} \omega^2\right) \exp\left(j \frac{\pi}{4}\right), \tag{3.49}$$

here $|\tilde{X}(\omega)| \approx 1, -\pi B_1 \leq \omega \leq \pi B_1$ and for all the remaining ω values $|\tilde{X}(\omega)| = 0$. Subsequently, $\overline{\omega^2} = \frac{2\pi^3 {B_1}^3}{3}$, $\overline{t^2} = \frac{A_1^2 \tau^3}{12}$ and $\overline{\omega t} = \frac{A_1^2 \tau^2 \pi B_1}{6}$

$$\mathbf{N}(\mathbf{\Theta_k}) = \beta \begin{bmatrix} \frac{3c^2 A_1^2 \tau^3}{4\gamma} & \frac{-3c^2 {A_1}^2 \tau^2 \pi B_1}{2\omega_c \gamma} \\ \frac{-3c^2 {A_1}^2 \tau^2 \pi B_1}{2\omega_c \gamma} & \frac{6c^2 \pi^3 {B_1}^3}{\gamma {\omega_c}^2} \end{bmatrix}, \tag{3.50}$$

where $\beta = \left(\frac{1}{A_1^2 B_1^2 \tau^2 \pi^2 (2\tau\pi B_1 - A_1^2 \tau^2)}\right)$ and $|\mathbf{N}(\mathbf{\Theta_k})| = \beta^2 \left(\frac{18c^4\pi^3\tau^3 {A_1}^2 {B_1}^3 - 9c^4\pi^2\tau^4 {A_1}^4 {B_1}^2}{4\gamma^2 {\omega_c}^2}\right)$. It is evident from the expression that, $|\mathbf{N}(\mathbf{\Theta_k})|$ can be reduced by considering optimal signal bandwidth (B_{1opt}) and high signal-to-residual noise ratio (γ) value. Hence the selection of the waveform parameter vector ($\mathbf{\Theta_k}$) is given by the following objective function,

$$\begin{aligned} \underset{\mathbf{\Theta_k}}{\text{minimize}} \quad & |\mathbf{N}(\mathbf{\Theta_k})|, \\ \text{subject to} \quad & \gamma_{max} \\ & B_{min} < B_{1opt} < B_{max} \end{aligned} \quad , \tag{3.51}$$

here '$\mathbf{\Theta_k}$' represents the received waveform parameter vector at time instant 'k'. From (3.51) the optimal waveform bandwidth (B_{1opt}) is obtained based on the optimization problem defined in (Trees 1971), using minimum bandwidth (B_{min}), maximum bandwidth (B_{max}) as the constraints of the optimization problem. i.e., $B_{min} < B_{1opt} < B_{max}$. In addition, the optimization problem is solved based on the signal-to-residual noise ratio (γ) and bandwidth (B_{min}, B_{max}) as constraints (Venkataraman 2009). By tuning the waveform parameters of the LFM-pulse, we can minimize the measurement noise covariance, thereby achieving an enhanced radar target tracking performance in the JRCS.

5) $LFM - GaussianPulse$

Let $\tilde{x}(t)$ be an LFM-Gaussian pulse and it is provided by,

$$\tilde{x}(t) = \left(\frac{1}{\pi\tau^2}\right)^{1/4} \exp\left[-\left(\frac{1}{2\tau^2} - jb\right)t^2\right] \tag{3.52}$$

$$\tilde{X}(\omega) = \frac{(4\pi\tau^2)^{1/4}}{\sqrt{1-2jb\tau^2}} \exp\left(\frac{-\omega^2\tau^2}{2\left(1-2jb\tau^2\right)}\right) \tag{3.53}$$
$$\overline{\omega^2} = \left(1/2\tau^2\right) + 2b^2\tau^2, \quad \overline{t^2} = \tau^2/2, \quad \overline{\omega t} = b\tau^2$$

$$\mathbf{N}(\mathbf{\Theta_k}) = \begin{bmatrix} \frac{c^2\tau^2}{2\gamma} & \frac{-c^2b\tau^2}{\omega_c\gamma} \\ \frac{-c^2b\tau^2}{\omega_c\gamma} & \frac{c^2}{\omega_c^2\gamma}\left(\frac{1}{2\tau^2} + 2b^2\tau^2\right) \end{bmatrix} \tag{3.54}$$

Further, $|\mathbf{N}(\mathbf{\Theta_k})| = \frac{c^4}{4{\omega_c}^2\gamma^2}$. It is evident from (3.54) and $|\mathbf{N}(\mathbf{\Theta_k})|$ that, the measurement noise covariance can be reduced by choosing maximum sweep rate (b_{max}) and maximum signal-to-residual noise ratio (γ_{max}) values. Hence the waveform parameter vector ($\mathbf{\Theta_k}$) is selected based on the following optimization problem,

$$\begin{aligned} \underset{\mathbf{\Theta_k}}{\text{minimize}} \quad & |\mathbf{N}(\mathbf{\Theta_k})|, \\ \text{subject to} \quad & \gamma_{max} \\ & b_{max}, \end{aligned} \tag{3.55}$$

here, the maximized signal-to-residual noise ratio (γ_{max}) and maximized sweep rate (b_{max}) are the waveform constraints (tunable waveform parameters) of the optimization problem (3.55). With reference to the proper selection of tunable waveform parameters of the LFM-Gaussian pulse, the measurement noise covariance can be minimized such that an improved radar target tracking performance can be achieved.

6) $NLFM - Pulse$

The NLFM-pulse waveform is widely used due to its special characteristics like low side-lobe ratio, and high flexibility ([Mahipathi et al., 2021]). A second-order NLFM pulse with a polynomial phase is represented as,

$$\tilde{x}(t) = \mathrm{e}^{i\pi\left(p_1B^2t^2 + p_2B^4t^4\right)} \quad -\frac{\tau}{2} \leq t \leq \frac{\tau}{2}, \tag{3.56}$$

here p_1, p_2 are phase coefficients of the phase polynomial, and B_1 represents the bandwidth. Based on the Principle of Stationary Phase (PSP) approximation, the

spectrum of the signal is expressed as,

$$\tilde{X}(\omega) \approx 2\sqrt{\frac{-\pi}{2\Phi''(t_0,\omega)}}\mathrm{e}^{-i\frac{\pi}{4}}\tilde{x}(t_0)\,\mathrm{e}^{i\Phi(t_0,\omega)}$$
$$= 2\sqrt{\frac{-1}{4p_1{B_1}^2+24p_2{B_1}^4t_0^2}}\mathrm{e}^{-i\frac{\pi}{4}}\mathrm{e}^{i\pi\left(p_1{B_1}^2t_0^2+p_2{B_1}^4t_0^4\right)} \quad (3.57)$$
$$\cdot\ \mathrm{e}^{i\pi\left(p_1{B_1}^2t_0^2+p_2{B_1}^4t_0^4-2ft_0\right)},$$

here $\Phi''(t,\omega)=\frac{\partial^2\Phi(t,\omega)}{\partial t^2}=\pi\left(2p_1{B_1}^2+12p_2{B_1}^4t^2\right)$. Further, $|\tilde{X}(\omega)|\approx 1, -\pi B_1\leq\omega\leq\pi B_1$ and for all the remaining ω values $|\tilde{X}(\omega)|=0$.

Subsequently, $\overline{\omega^2}=\frac{8\pi^3{B_1}^3}{3(4p_1{B_1}^2+24p_2{B_1}^4t_0{}^2)}$, $\overline{t^2}=\frac{\tau^3}{12}$, and $\overline{\omega t}=\frac{\pi p_1B_1^2\tau^3}{6}+\frac{\pi p_2{B_1}^4\tau^5}{20}$

$$\mathbf{N}(\mathbf{\Theta_k})=\frac{1}{\gamma}\mathbf{T}\begin{bmatrix}\frac{\tau^3}{12} & \frac{\pi p_1B_1^2\tau^3}{6}+\frac{\pi p_2{B_1}^4\tau^5}{20}\\ \frac{\pi p_1B_1^2\tau^3}{6}+\frac{\pi p_2{B_1}^4\tau^5}{20} & \frac{8\pi^3{B_1}^3}{3(4p_1{B_1}^2+24p_2{B_1}^4t_0{}^2)}\end{bmatrix}\mathbf{T}^T, \quad (3.58)$$

here $\mathbf{T}=\mathrm{diag}\left(c/2, c/\left(2\omega_c\right)\right)$, c represents the waveform propagation velocity and ω_c is the carrier frequency. In NLFM pulse waveform, phase coefficients (p_1, p_2) and signal-to-residual noise ratio (γ) are the waveform constraints (tunable waveform parameters). Here the optimized phase coefficients (p_1, p_2) are evaluated based on our previous work Mahipathi et al. [2021]. From (3.58), it is evident that the measurement noise covariance can be minimized by optimizing the phase coefficients and maximizing the (γ) value. Further, by minimizing the measurement noise covariance an improved radar target tracking performance can be accomplished in the CRCS.

With reference to Table 3.1, the measurement noise covariance matrix ($\mathbf{N}(\mathbf{\Theta_k})$) is evaluated for all the designated waveforms. It is noticed that the selection of a radar waveform and its tunable parameters plays an important role in minimizing the measurement noise covariance such that efficient target estimation performance can be achieved. From the above analysis, the standard deviation of the range and range rate measurements is calculated for designated waveforms and is listed in Table 3.2. It is noticed that the NLFM-pulse waveform exhibits the minimum range and range rate measurement errors compared to other waveforms.

3.3 Target Tracking

A single radar sensor operating in a co-located configuration produces the measurements pertaining to the target present in the surveillance. These measurements are filtered and estimate the state of interest.

Table 3.1: Parameters considered for evaluating the measurement noise covariance matrix

Parameter	Value
Operating Bandwidth (B)	5 MHz
Operating frequency at the center (f)	3 GHz
Target range of a radar system (R)	50 km
Antenna gain of a radar (G_r)	40 dBi
Radar transmitted power (P_t)	1 MW
Target cross-section area of a radar (σ_a)	30 m^2
Temperature (T_k)	1000 K
Boltzmann constant (K_B)	1.38x10^{-23} J/K
Overall communication antenna gain and propagation loss (b)	6.33x10^{-13}
Transmitted communication signal power (P_{comm})	300 mW
Power spectral density of phase noise (η_0)	-110 dBc/Hz
Range fluctuation process variance ($\sigma_f{}^2$)	25 m^2
Time-bandwidth product (TB)	128
Range of the communication system	10 km

Table 3.2: Standard deviation of range and range rate measurements for various waveforms.

Type of waveform	**Range standard deviation(σ)**	**Range rate standard deviation(σ)**
Rectangular pulse	8.48 m	7.87 m/s
Triangular pulse	7.62 m	7.61 m/s
Gaussian pulse	5.91 m	7.07 m/s
LFM pulse	6.98 m	6.02 m/s
LFM Gaussian pulse	5.91 m	4.86 m/s
NLFM pulse	5.10 m	3.70 m/s

3.3.1 Measurement and State Model

The measurement model is given by,

$$z_j(k) = HX(k) + n_j(k) \tag{3.59}$$

Here $X(k)$ is the state vector at k^{th} time instant, H represents a measurement transition matrix, and $n_j(k)$ represents the measurement noise. The measurement vector is a stacked form of range and range rate, which is represented as $z_k = \begin{bmatrix} r_k & \dot{r}_k \end{bmatrix}^T$, where r and $\dot{r}$ represents the range and range rate respectively. Similarly, the state is given by $X = [r, \dot{r}, \ddot{r}]$. Since the measurement and state are in a linear relation, in (3.59) the measurement model is represented as a multiplication of state and measurement. The measurement transition matrix can be written as

$$H = \begin{bmatrix} 1 & 0 & 0 \\ 0 & 1 & 0 \end{bmatrix}. \tag{3.60}$$

Both the noise components present in range and range rate are independent and identically distributed (iid) and follow a Gaussian random process with mean as zero and standard deviation σ_r and $\sigma_{\dot{r}}$ respectively. The waveform parameter vector $\mathbf{\Theta_k}$ characterizes the received waveform at time instant k and it is incorporated in the measurement noise covariance matrix $\mathbf{N}(\mathbf{\Theta_k}) = \mathbb{E}\{n(k)n(k)'\}$. The target kinematic model is given by

$$X(k+1) = F(k)X(k) + w(k), \tag{3.61}$$

where $X(k)$ represents a state vector and $w(k)$ is a Gaussian distributed white noise vector having zero mean and its covariance matrix is expressed as $Q(k) = \mathbb{E}[w(k)w(k)']$. The process noise vector $w(k)$ is due to the perturbation in $r, \dot{r}$, and $\ddot{r}$ dimensions. Here $F(k)$ denotes the state transition matrix for the constant range rate

$$F(k) = \begin{bmatrix} 1 & t_s & t_s/2 \\ 0 & 1 & t_s \\ 0 & 0 & 1 \end{bmatrix}, \tag{3.62}$$

here t_s represents the sampling time interval. This measurement generation is carried out under the condition of target detection probability ($p_d = 1$) and probability of false alarm ($p_{fa} = 0$). The target movement follows the CV model rather than the constant turn model. The reason behind this assumption is to illustrate the significance of extracted measurement noise covariance corresponding to the waveforms. In the case of non-linear trajectories and non-linear measurement relationships, the extended Kalman filters and IMM filters are required. It is hard to illustrate the significance of the extracted measurement noise covariance matrix parameter. Hence, the rest of the filtering is carried out using the Kalman filter owing to its optimal behaviour for linearity and Gaussian assumptions.

3.3.2 Filtering

There are three major steps involved in filtering, namely state prediction, calculation of gain, and then state updation. Firstly, the predicted state is expressed as,

$$\hat{X}(k+1 \mid k) = F\hat{X}(k \mid k) \tag{3.63}$$

subsequently, the predicted covariance is provided by,

$$P(k+1 \mid k) = FP(k \mid k)F' + Q(k) \tag{3.64}$$

The predicted measurement is expressed as,

$$\hat{z}(k+1/k) = H\hat{X}(k+1 \mid k) \tag{3.65}$$

Using the predicted measurement and actual observation, the innovation is calculated as

$$\gamma = z(k+1) - \hat{z}(k+1|k), \tag{3.66}$$

The gain of Kalman filter K is expressed as,

$$K(k+1) = P(k+1/k)H(k+1)' \tag{3.67}$$

$$[H(k+1)P(k+1/k)H(k+1)' + \mathbf{N}(\mathbf{\Theta_k})]^{-1}, \tag{3.68}$$

here $\mathbf{N}(\mathbf{\Theta_k})$ represents the measurement noise covariance matrix. Based on the above equations, the updated state is given by,

$$\hat{X}(k+1 \mid k+1) = \hat{X}(k+1 \mid k) + K(k+1)\gamma(k+1) \tag{3.69}$$

subsequently, the updated covariance is provided by,

$$P(k+1 \mid k+1) = P(k+1 \mid k) - K(k+1)H(k+1)K'(k+1) \tag{3.70}$$

3.3.3 Posterior Cramer-Rao Lower Bound (PCRLB)

In this work, we consider a standard theoretical lower bound posterior Cramer Rao lower bound (PCRLB) Bar-Shalom et al. [2010] to validate the state estimation. Let $X(k+1)$ be the state vector and estimation of the state vector with respect to the measurement set $z_{1:k+1}$ is denoted as $\hat{X}(k+1)$. According to Tichavsky et al. [1998], the PCRLB on the covariance matrix $P(k+1)$ is evaluated by taking the inverse of the Fisher Information Matrix (FIM) ($J(k+1)$).

$$P(k+1) \triangleq \mathbb{E}\left[\left(\hat{X}(k+1) - X(k+1)\right)\left(\hat{X}(k+1) - X(k+1)\right)'\right] \geq \mathbf{J(k+1)^{-1}}, \tag{3.71}$$

where,

$$\mathbf{J(k+1)} = \left[F(k)^{-1}\right]^T J(k)F(k)^{-1} + Q(k)^{-1} + H(k)^T\mathbf{N}(\mathbf{\Theta_{k+1}})^{-1}H(k) \tag{3.72}$$

Based on the measurement noise covariance matrix formula in (3.34), $\mathbf{N}(\mathbf{\Theta_{k+1}})$ is expressed as,

$$\mathbf{N}(\mathbf{\Theta_{k+1}}) = \frac{1}{\gamma}\mathbf{T}\mathbf{U}(\mathbf{\Theta_{k+1}})^{-\mathbf{1}}\mathbf{T}^T \tag{3.73}$$

3.4 Results and Analysis

The simulated results are presented here to witness the significance of optimum waveform selection for enhancing tracking performance. A single in-band communication transmitter and a radar sensor are assumed to elucidate the uncertainty of the radar target state in the presence of in-band communication residual interference.

3.4.1 Scenario Generation

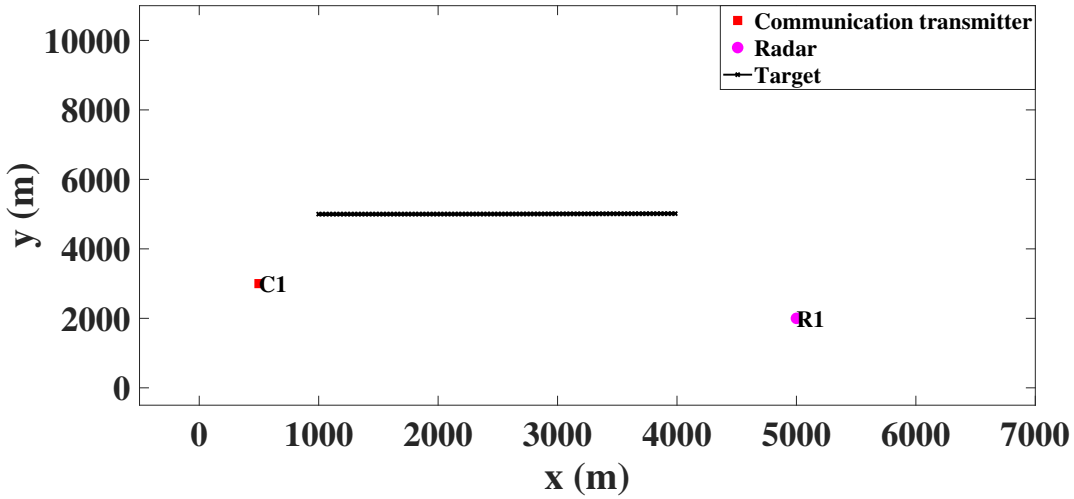

Figure 3.3: Generating a scenario for a single radar-sensor, single communication transmitter

In the simulated scenario, it is assumed that a JRC receiver is stationary and has a maximum detectable range of R_{max}=50 km. From Figure 3.3, it is considered that the radar sensor is located at [5000, 2000]′ and an in-band communication transmitter is located at [500, 2500]'. Here the radar is of mono-static type, hence the JRC receiver node is also present at the radar position. Within the surveillance, a target is present at $[10000, 10000]$ and moving with 40 m/s and 20 m/s along x and y directions respectively. In addition to that, throughout the simulation scenario, the target is following a Constant Velocity (CV) motion model. The perturbation of the target is modeled as process noise and it follows an additive white Gaussian noise distribution. The noise components corresponding to position is $N(0, 0.05^2)$, where, $N(\mu, \sigma^2)$ is a Gaussian pdf having mean (μ) and variance (σ^2). Similarly, the noise component in velocity is taken as $N(0, 0.02^2)$. The total simulation time is 100 s with a sampling interval of 1 s. Besides, the radar sensor receives the range and range rate measurements corresponding to the waveform of operation at the JRC node.

3.4.2 Track filtering

The Kalman Filter(KF) is applied to estimate the range and range rate values at various instants of time. To initiate the track, a one-point initialization approach Musicki

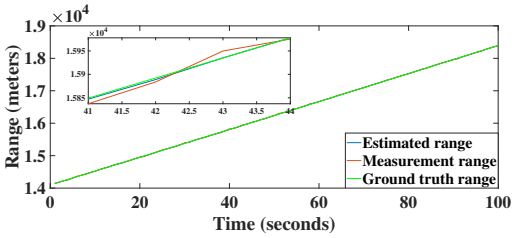

(a) Range measurement for a rectangular pulse waveform

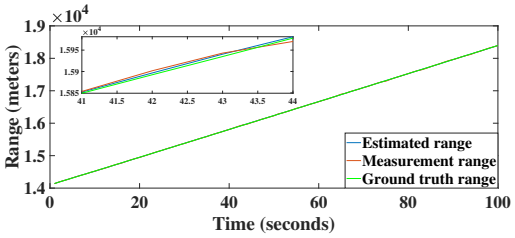

(b) Range measurement for an NLFM waveform

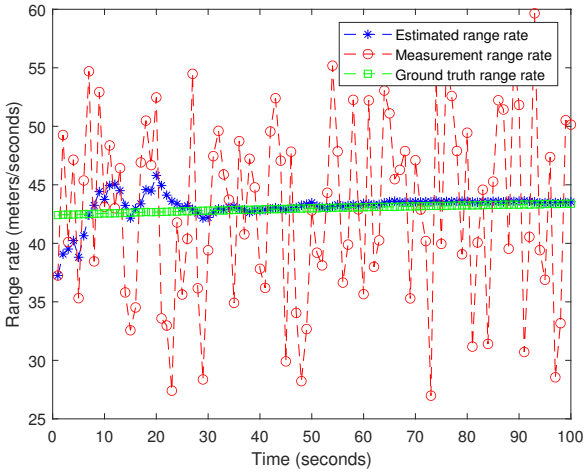

(c) Range rate measurement for a rectangular pulse waveform

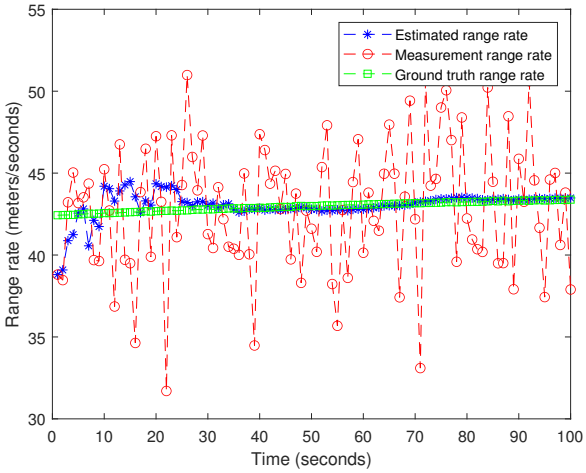

(d) Range rate measurement for an NLFM waveform

Figure 3.4: Comparison of range and range rate for rectangular and NLFM waveforms

and Song [2013] is considered, and the maximum velocity is tuned to $V_{max} = 40\ m/s$. A Constant Velocity (CV) motion model is utilized in the prediction steps. The process noise covariance is chosen as

$$Q = [N(0, 0.05^2), N(0, 0.02^2), N(0, 0.05^2), N(0, 0.02^2)]' \tag{3.74}$$

The optimized measurement noise is used for the calculation of innovation covariance.

As an illustration, for example, two different waveforms and the same ground truth are considered to compare the importance of computing the measurement noise and the superiority of the waveform. The range and range rate measurements ground truth, observed measurement, and estimated state are visualized in Figure 3.4. Figure 3.4(a) and Figure 3.4(b) show the estimated range and acquired range measurement in comparison to ground truth for rectangular-pulse and NLFM-pulse waveforms respectively. Since the range is in the order of $10^4\ m$, it is hard to visualize. Further, Figure 3.4(c) and Figure 3.4(d) show the estimated range rate and acquired range rate

measurement in comparison to ground truth for rectangular-pulse and NLFM-pulse waveforms respectively. Here, we can see that the ground truth range rate is around 43 m/s, whereas the acquired range rate measurements fluctuate around the ground truth range rate with their standard deviations of the waveform. It is worth noting that the estimated range rate fluctuates initially due to the initialization problem. Thereafter, it saturates over time. In the process of estimation, the filter is tuned to the range and range rate covariance obtained in Table 3.2 for a rectangular pulse and NLFM-pulse waveform. Further, it is also evident that the optimized NLFM-pulse waveform exhibits fewer fluctuations in the range and range rate estimations. However, by visualization, it is hard to conclude the superiority of the waveforms. Hence, better performance analysis can be done by estimating the Root Mean Square Error (RMSE) for the range and range rate measurements.

The RMSE of range measurement is plotted in Figures 3.5(a)–3.5(f) for the selected waveforms. It is perceived that the estimated RMSE is compared with both the measurement RMSE (before filtering) and PCRLB for all the selected waveforms. Besides, it is also noticed that the estimated RMSE (range measurement error) values are gradually decreasing by the time scan for all the designated waveforms. In addition, for all the waveforms, the estimated RMSE values are within the PCRLB limit in the given time duration. Among all the waveforms, the optimized NLFM-pulse waveform outperforms the remaining waveforms in terms of deviation between estimated RMSE and PCRLB. That is, estimated RMSE values of the NLFM-pulse waveform are approaching the minimum error variance. We also observed that frequency-modulated waveforms (LFM-pulse, LFM-Gaussian pulse, and NLFM-pulse) outperform the amplitude-only modulated waveforms (rectangular pulse, triangular pulse, and Gaussian pulse) in terms of range error.

In Figures 3.6(a)–3.6(f), the estimated range rate error values are compared with both the measurement RMSE (before filtering) and PCRLB from a range rate perspective for all the selected waveforms. Further, it is noticed that the estimated RMSE (range rate measurement error) values are gradually decreasing in accordance with the time scan (as shown in Figures 3.6(a)–3.6(f)). Furthermore, it is also perceived that the estimated range rate RMSE values are within the PCRLB limit at all time instants for all the designated waveforms. Among all the selected waveforms, the

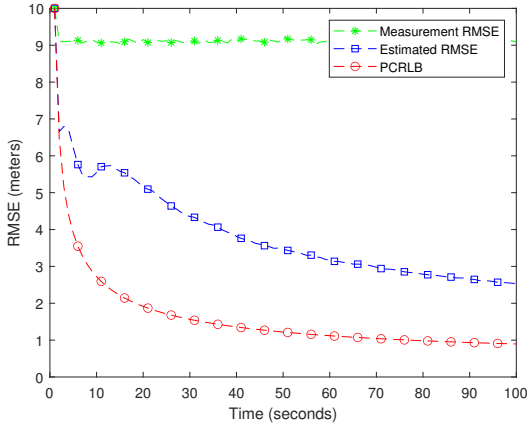

(a) Analyzing range measurement error for a rectangular pulse waveform

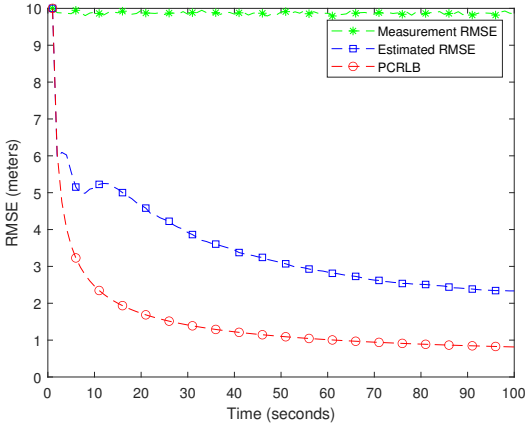

(b) Analyzing range measurement error for a triangular pulse waveform

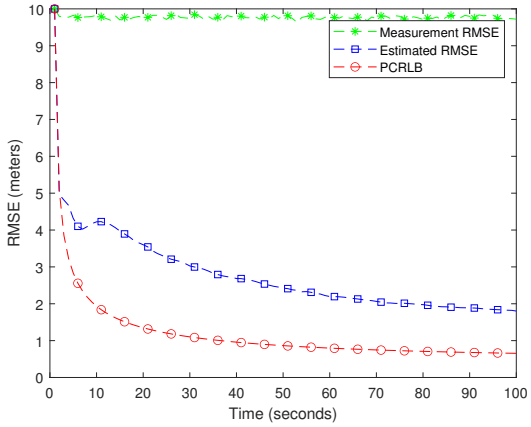

(c) Analyzing range measurement error for a Gaussian pulse waveform

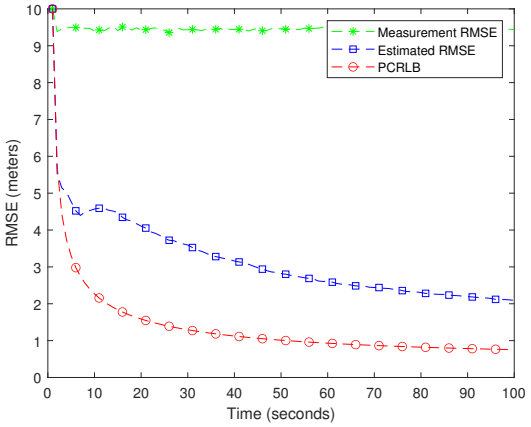

(d) Analyzing range measurement error for an LFM pulse waveform

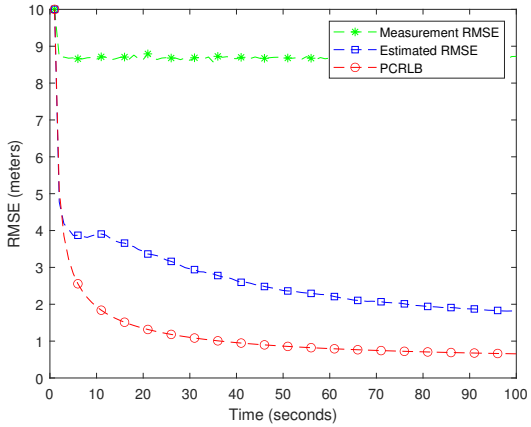

(e) Analyzing range measurement error for an LFM Gaussian pulse waveform

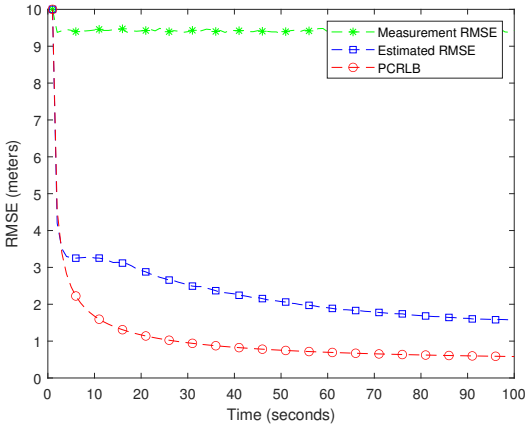

(f) Analyzing range measurement error for an NLFM pulse waveform

Figure 3.5: Comparison of range measurement error for selected waveforms

optimized NLFM-pulse waveform outperforms the remaining waveforms in terms of deviation between the estimated RMSE and the PCRLB. That is, range rate RMSE values of the NLFM-pulse waveform are approaching minimum error variance. We also

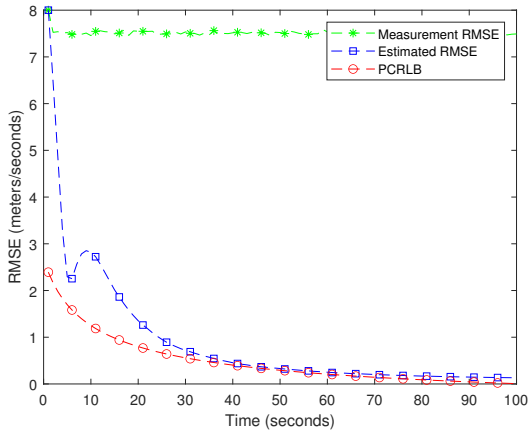

(a) Analyzing range rate measurement error for a rectangular pulse waveform

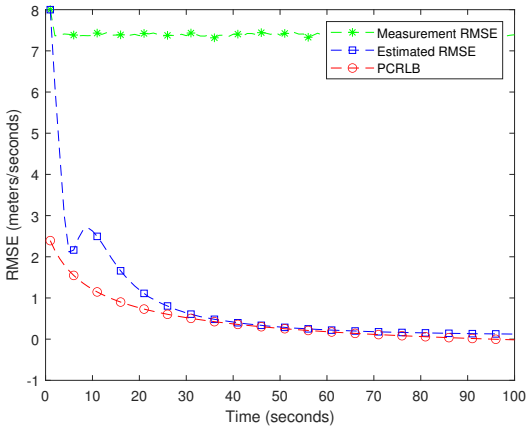

(b) Analyzing range rate measurement error for a triangular pulse waveform

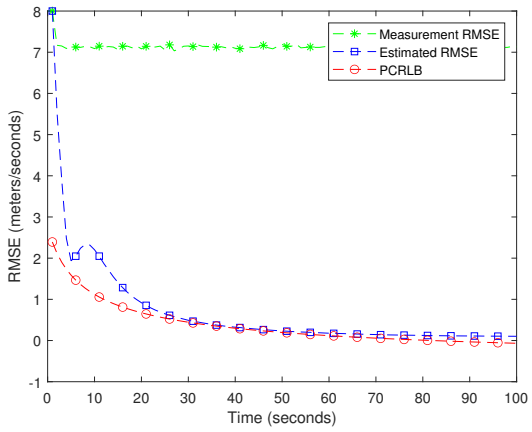

(c) Analyzing range rate measurement error for a Gaussian pulse waveform

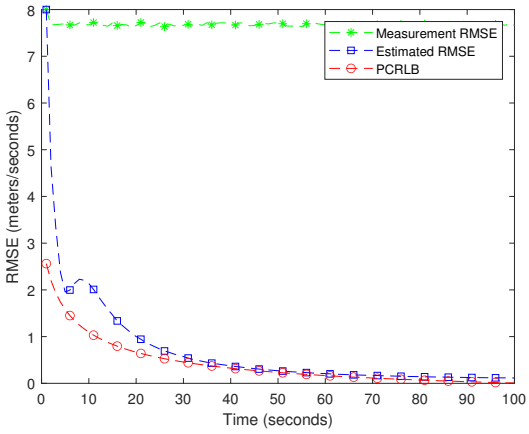

(d) Analyzing range rate measurement error for an LFM pulse waveform

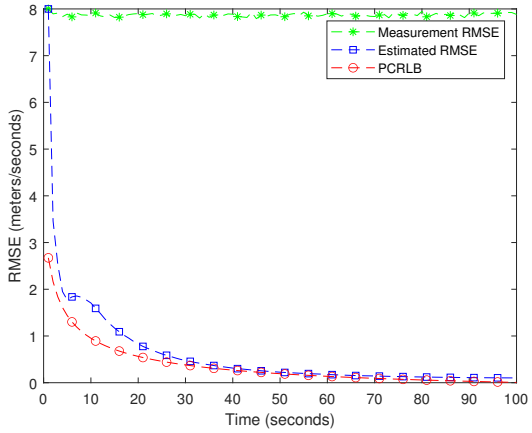

(e) Analyzing range rate measurement error for an LFM Gaussian pulse waveform

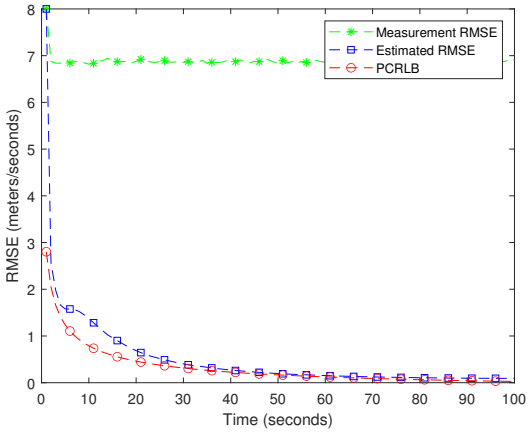

(f) Analyzing range rate measurement error for an NLFM pulse waveform

Figure 3.6: Comparison of range rate measurement error for selected waveforms

observed that the frequency-modulated waveforms (LFM-pulse, LFM-Gaussian pulse, and NLFM-pulse) provide improved performance compared to amplitude-only modulated waveforms(rectangular pulse, triangular pulse, and Gaussian pulse) in terms of range rate RMSE.

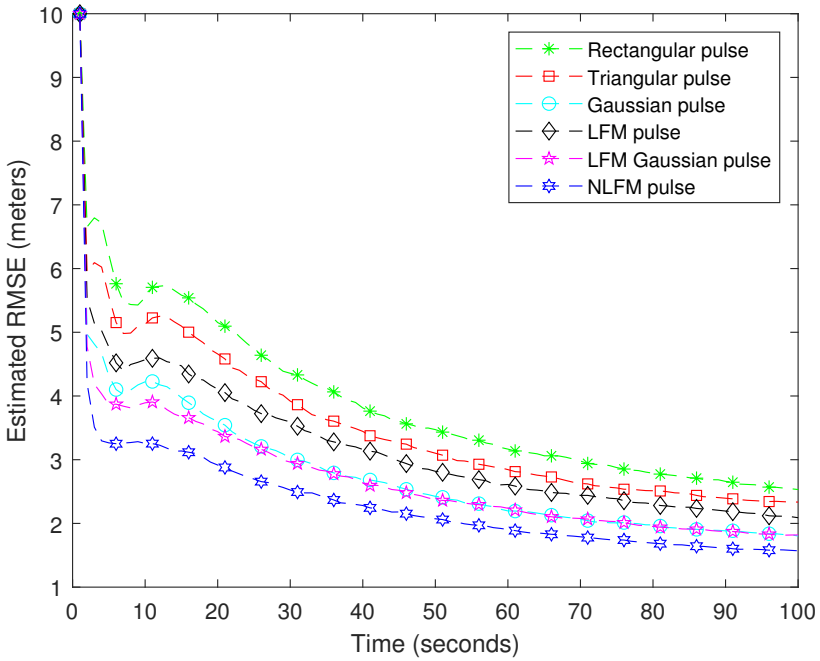

Figure 3.7: Analyzing estimated range measurement error for various designated waveforms

The estimated range RMSE of various waveforms is plotted in Figure 3.7. It is evident from the plot that, the estimated range RMSE values for all the waveforms are gradually decreasing with the increasing number of time scans. Further, the range RMSE of the NLFM-pulse waveform yields improved performance compared to the remaining waveforms. Furthermore, the range RMSE values of the rectangular pulse waveform are high (which is undesirable) compared to other designated waveforms. In Figure 3.8, the range rate RMSE of various selected waveforms is plotted. It is noticed from the plot that the range rate RMSE for all the waveforms is gradually decreasing with the increasing number of time scans. Additionally, the range rate RMSE of the NLFM-pulse waveform provides superior performance compared to the remaining waveforms. In addition, the range rate RMSE of the rectangular pulse waveform provides poor performance compared to other designated waveforms.

Here, we quantified the Monte-Carlo-based simulation results against the PCRLB.

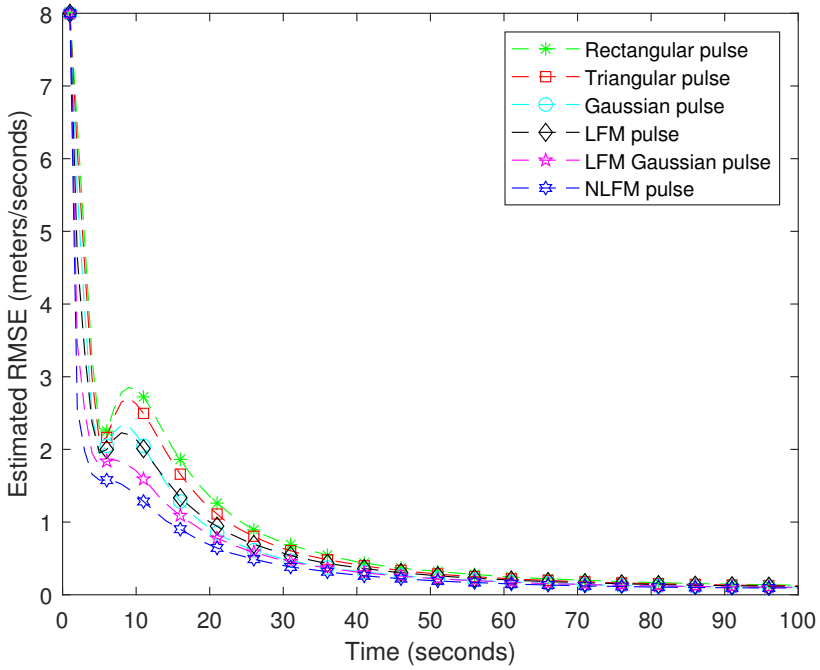

Figure 3.8: Analyzing estimated range rate measurement error for various designated waveforms

It is noticed that the RMSE is decreasing over time and coming very near the theoretical PCRLB value. This intuitively shows that the measured covariance from the waveform characteristics is an optimal approach compared to tuning the measurement noise covariance. In addition, the PCRLB value and RMSE value for the NLFM waveform are low, which gives an understanding that the filtering/tracking accuracy is high.

3.5 Summary

This chapter analyzed the effect of communication residual components on the radar target state estimation performance in a CRCS environment. In addition, the NLFM radar waveform outperforms the other designated radar waveforms in terms of target state estimation performance in a CRCS. The next chapter i.e., Chapter 4 illustrates the importance of communication-aided radar target state estimation in a CRCS framework.

Chapter 4

Communication-Aided Target State Estimation in a CRCS

This chapter introduces a communication-aided novel measurement model to analyze the radar target state estimation performance in a CRCS. The measurement noise covariance matrix is evaluated for the radar and communication waveform combinations to characterize the radar sensor behaviour. In addition, an iterative least square framework is considered to obtain the converted measurements. Thereafter, the Kalman filter is deployed to estimate the target dynamics for both waveform combinations in a CRCS environment.

4.1 Problem Formulation

A generalized cooperative radar-communication spectrum sharing scenario is depicted in Figure 4.1, where a single in-band communication transmitter, one monostatic radar transceiver, and a single target are present. Here the Joint Radar-Communication (JRC) transceiver is efficient enough to perform both radar-sensing and communication operations. When the radar transceiver is operating in a surveillance mode, it receives a target echo signal through a monostatic channel and an in-band communication signal scattered off the target through a bistatic channel. In addition, the radar receiver also receives a direct communication signal through a reference channel. Then, the received signal at the radar receiver is given by,

$$y_{rad}^{sur}(t) = s_{rad}(t-\tau) + s_{com}(t-\tau_c) + n(t) \tag{4.1}$$

$$y_{rad}^{ref}(t) = s_{com}(t) + n(t), \tag{4.2}$$

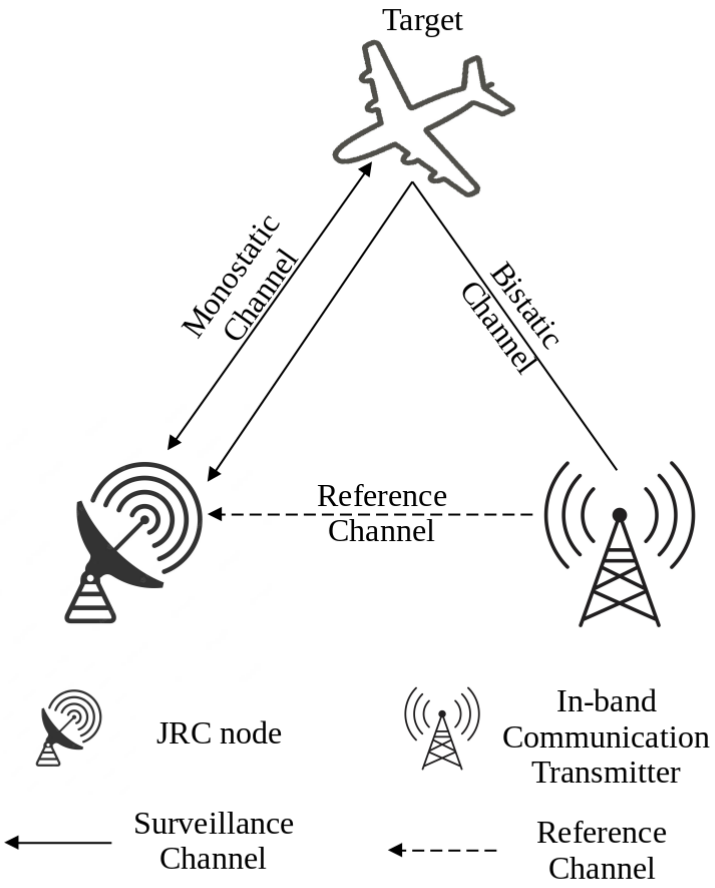

Figure 4.1: System model for cooperative spectrum sharing between radar and communication systems

here $y_{rad}^{sur}(t)$ represents the signal received at the JRC node when the radar is operating in surveillance mode, $y_{rad}^{ref}(t)$ signifies the signal received at the JRC node through the reference channel, $s_{rad}(t-\tau)$ signifies the radar-sensor target echo signal, $s_{com}(t-\tau_c)$ represents the communication signal scattered off the target, $n(t)$ signifies the thermal noise present in the receiver, and $s_{com}(t)$ indicates the directly received communication signal at the radar receiver. Interestingly, the in-band communication signal reflected off the target ($s_{com}(t-\tau_c)$) aids the target information at the radar receiver. In addition, τ represents the true target time delay to the radar-transmitted signal, and τ_c is the true target delay experienced by a transmitted communication signal.

In addition, it is considered that the JRC node utilizes the Successive Interference Cancellation (SIC) receiver model (Bliss 2014), which mitigates the mutual interference among radar sensing and communication systems. The SIC receiver model is utilized such that, the strongest received signal component is first removed from the

joint radar-communication signal (Bică and Koivunen 2018). Already, in some of the previous significant contributions (Bliss 2014), (Chiriyath et al. 2016c), it was very well demonstrated how the SIC model separates the radar and communication returns at the JRC receiver. In addition, the phase noise present in the receiver introduces a signal reconstruction error in the SIC receiver model (Chiriyath et al. 2019). Moreover, the effect of phase noise on the SIC receiver model was discussed in (Chiriyath et al. 2016b). Then, the radar and communication signal separation at the JRC node is achieved by considering the following cases:

Case 1: Strong radar target return

It is considered that the radar target round trip time delay is known based on the previous observations. Thus by utilizing this information, the radar target return is reconstructed and it is suppressed from the $y_{rad}^{sur}(t)$. Here, the reconstructed radar target return ($y_{rec}(t)$) is given by,

$$y_{rec}(t) + e_r(t) = s_{rad}(t - \tau), \tag{4.3}$$

here $e_r(t)$ is the signal reconstruction error concerning the reconstructed radar echo signal ($y_{rec}(t)$) as in (Bliss 2014). In addition, the communication return is obtained as follows:

$$y_{rad}^{sur}(t) - y_{rec}(t) = s_{com}(t - \tau_c) + e_r(t) + n(t) \tag{4.4}$$

As a result, the set of radar and communication measurements are obtained as follows:

$$y_{r1}(t) = y_{rec}(t) = s_{rad}(t - \tau) + e_r(t) \tag{4.5}$$

$$y_{c1}(t) = y_{rad}^{sur}(t) - y_{rec}(t) = s_{com}(t - \tau_c) + n(t) + e_r(t) \tag{4.6}$$

Case 2: Strong communication return

In the same way, when the communication signal scattered off the target is stronger, then it is suppressed from the ($y_{rad}^{sur}(t)$). Moreover, it is considered that the radar acquires knowledge regarding the target channel based on the target reflected communication signal, and it can predict the time delay experienced by the received communication signal. Concerning the predicted time delay, the received communications signal is reconstructed as follows:

$$s_{com}(t - \tau_c) = y_{rec}(t) + e_c(t), \tag{4.7}$$

here $e_c(t)$ is the communication signal reconstruction error. Further, the radar and communication measurements are expressed as follows:

$$y_{r2}(t) = y_{rad}^{sur}(t) - y_{rec}(t) = s_{rad}(t-\tau) + n(t) + e_c(t) \tag{4.8}$$

$$y_{c2}(t) = y_{rec}(t) = s_{com}(t-\tau_c) + e_c(t) \tag{4.9}$$

It is assumed that noise $n(t)$ follows the Gaussian distribution having a spectral height $N_0/2$. In addition, to attain reasonable inferences from both the radar and communication signal reconstruction error components $e_r(t)$ and $e_c(t)$ are also distributed in a Gaussian manner with the spectral heights $N_{er}/2$, $N_{ec}/2$ respectively. Moreover, the radar target return envelope is expressed as,

$$s_{rad}(t-\tau) = \sqrt{E_r} e^{j\phi_1} \tilde{x_r}(t-\tau) e^{jv_r t}, \tag{4.10}$$

here E_r is the energy of the radar target return, ϕ_1 denotes the phase shift associated with the target return, $\tilde{x_r}(t)$ signifies radar transmitted signal envelope, and v_r represents the Doppler shift. Similarly, the communication signal reflected off the target received at the JRC node is provided by,

$$s_{com}(t-\tau_c) = \sqrt{E_c} e^{j\phi_2} \tilde{x_c}(t-\tau_c) e^{jv_c t}, \tag{4.11}$$

where E_c is the energy of the communication signal reflected off the target, ϕ_2 signifies the phase shift associated with the communication return, $\tilde{x_c}(t)$ transmitted communication signal envelope, and v_c represents the Doppler shift. Further, the normalized spectral density of $e_r(t)$ is provided by (Chiriyath et al. 2019),

$$N_{er}(f) = \left(4\pi^2\right) \|a\|^2 P_{rad}\ \eta_0\ \sigma_{\tau,pr}^2 \|S_{rad}(f)\|^2 f^2, \tag{4.12}$$

here a signifies the overall radar channel gain, P_{rad} indicates the transmitted radar signal power, η_0 signifies the phase noise spectral density, $\sigma_{\tau,pr}^2$ represents the range deviation process variance, $S_{rad}(f)$ signifies the spectrum of radar target return, and f is the frequency of the transmitted radar signal. In the same way, the normalized spectral density of $e_c(t)$ is given by

$$N_{ec}(f) = \left(4\pi^2\right) \|b\|^2 P_{com}\ \eta_0\ \sigma_{\tau_c,pr}^2 \|S_{com}(f)\|^2 f^2, \tag{4.13}$$

where b signifies the overall communication channel gain, P_{com} is the transmitted communication signal power, $\sigma_{\tau_c,pr}^2$ represents the range deviation process variance

concerning communication return, and $S_{com}(f)$ represents the spectrum of communication return. The aforementioned two cases i.e., strong radar return and strong communication return affect the measurement noise covariance matrix and therefore have an impact on the sensor characterization (Kershaw and Evans 1994).

The proposed framework analyzes the effect of the error components on the characterization of a radar sensor. In this process, a detailed mathematical analysis is presented in Section 4.2 to compute the measurement noise covariance matrix. Further, a novel measurement model is developed based on the converted measurements to estimate the target state in a CRCS environment.

4.2 Characterization of a radar sensor

The radar sensor characterization predominantly depends on knowledge of the measurement noise covariance matrix ($\mathbf{N}(\mathbf{\Theta_k})$) (Kershaw and Evans 1994). In addition, it also relies on the non-linear function of the waveform parameter vector ($\mathbf{\Theta_k}$). Where $\mathbf{\Theta_k}$ knows the received waveform parameters of the chosen waveform at the time instant $\mathbf{k}$. The measurement noise covariance matrix establishes the connection between the received waveform parameter vector $\mathbf{\Theta}_k$ and the covariance matrix of the noisy observations ($\mathbf{N}(\mathbf{\Theta_k})$) as derived in (Kershaw and Evans 1994) and it is provided by,

$$\mathrm{E}[(\mathrm{y}-\bar{\mathrm{y}})(\mathrm{y}-\bar{\mathrm{y}})^T] = \mathbf{N}(\mathbf{\Theta_k}) = \mathbf{T}\mathbf{J}^{-1}\mathbf{T}^T, \tag{4.14}$$

here $\mathrm{y} = \mathbf{T}\alpha$, y denotes the tracking system measurement vector and it is obtained based on a range (r) and range-rate ($\dot{r}$) i.e., $\mathrm{y} = [r \;\; \dot{r}]^T$. Whereas, $\bar{\mathrm{y}}$ denotes the mean of the measurement vector y, α denotes the receiver estimation parameter vector, and it is obtained based on the received signal vector i.e., $\alpha = [\tau_1 \;\; w_1]^T$. Here τ_1 denotes the time delay and w_1 denotes the Doppler frequency. Further, $\mathbf{T}$ is the transformation matrix and it is given by (Sira et al. 2004), $\mathbf{T} = \mathrm{diag}\,(c/2, c/(2\omega_c))$. Here c represents the waveform propagation velocity and ω_c is the carrier frequency. Here $\mathbf{J}$ is the Fisher information matrix. From (4.14), it is evident that the Fisher Information Matrix (FIM) needs to be evaluated to determine the measurement noise covariance matrix ($\mathbf{N}(\mathbf{\Theta_k})$). However, we need to find the FIM ($\mathbf{J}$) for all the radar and communication measurements (4.5), (4.6), (4.8), and (4.9) corresponding to two different cases i.e., strong radar target return and strong communication return.

4.2.1 Calculation of Fisher Information Matrix (J)

The Fisher information matrix (**J**) of order 2x2 is given by,

$$\begin{bmatrix} J_{11} & J_{12} \\ J_{21} & J_{22} \end{bmatrix} \tag{4.15}$$

Based on the parameters of interest (τ_1 and ω_1), the Fisher information matrix elements are expressed as,

$$J_{11} = -\mathrm{E}[\frac{\partial^2}{\partial \tau_1^2} \ln \Lambda\left(\tau_1, \omega_1\right)] \tag{4.16}$$

$$J_{22} = -\mathrm{E}[\frac{\partial^2}{\partial \omega_1^2} \ln \Lambda\left(\tau_1, \omega_1\right)] \tag{4.17}$$

$$J_{12} = J_{21} = -\mathrm{E}[\frac{\partial^2}{\partial \tau_1 \partial \omega_1} \ln \Lambda\left(\tau_1, \omega_1\right)] \tag{4.18}$$

Case 1: Strong radar target return

1(a) Radar measurement ($y_{r1}(t)$)

Initially, it is necessary to find the log-likelihood function to deduce the elements of the Fisher Information Matrix (FIM). According to (Trees 1971), the log-likelihood function with respect to the radar measurement (4.5) is evaluated as,

$$\ln \Lambda\left(\tau_1, \omega_1\right) = \frac{1}{N_{er}} \frac{\bar{E}_r}{\bar{E}_r + N_{er}} \left\{ \left| L(\tau_1, \omega_1) \right|^2 \right\}, \tag{4.19}$$

here,

$$L(\tau_1, \omega_1) = \int_{\infty}^{\infty} y_{r1}(t) \tilde{x_r}^*(t - \tau_1) \exp^{-j\omega_1 t}\, dt \tag{4.20}$$

from (4.19),

$$\frac{\partial \ln \Lambda(\tau_1, \omega_1)}{\partial \tau_1} = Z' \left[L(\tau_1, \omega_1) \frac{\partial L^*(\tau_1, \omega_1)}{\partial \tau_1} + \frac{\partial L(\tau_1, \omega_1)}{\partial \tau_1} L^*(\tau_1, \omega_1) \right],$$

$$= 2Z' \,\mathrm{Re} \left[L(\tau_1, \omega_1) \frac{\partial L^*(\tau_1, \omega_1)}{\partial \tau_1} \right], \tag{4.21}$$

where,

$$Z' \triangleq \frac{1}{N_{er}} \frac{\bar{E}_r}{\bar{E}_r + N_{er}} \tag{4.22}$$

Further, the following derivatives are needed to find the Fisher information matrix.

$$\frac{\partial^2 \ln \Lambda(\tau_1, \omega_1)}{\partial \tau_1^2} = 2Z' \,\mathrm{Re} \left[\frac{\partial L(\tau_1, \omega_1)}{\partial \tau_1} \cdot \frac{\partial L^*(\tau_1, \omega_1)}{\partial \tau_1} + L(\tau_1, \omega_1) \frac{\partial^2 L^*(\tau_1, \omega_1)}{\partial \tau_1^2} \right] \tag{4.23}$$

$$\frac{\partial^2 \ln \Lambda(\tau_1,\omega_1)}{\partial\tau_1\partial\omega_1} = 2Z' \operatorname{Re}\left[\frac{\partial L(\tau_1,\omega_1)}{\partial\omega_1}\cdot\frac{\partial L^*(\tau_1,\omega_1)}{\partial\tau_1} + L(\tau_1,\omega_1)\frac{\partial^2 L^*(\tau_1,\omega_1)}{\partial\tau_1\partial\omega_1}\right] \tag{4.24}$$

$$\frac{\partial^2 \ln \Lambda(\tau_1,\omega_1)}{\partial\omega_1^2} = 2Z' \operatorname{Re}\left[\frac{\partial L(\tau_1,\omega_1)}{\partial\omega_1}\frac{\partial L^*(\tau_1,\omega_1)}{\partial\omega_1} + L(\tau_1,\omega_1)\frac{\partial^2 L^*(\tau_1,\omega_1)}{\partial\omega_1^2}\right] \tag{4.25}$$

$$J_{11} = -E\left\{\frac{\partial^2 \ln \Lambda(\tau_1,\omega_1)}{\partial\tau_1^2}\right\} \tag{4.26}$$

$$\begin{aligned} &= -2Z'\left\{\int_{-\infty}^{\infty}\frac{\partial\tilde{x_r}^*(t-\tau_1)}{\partial\tau_1}\frac{\partial\tilde{x_r}(u-\tau_1)}{\partial\tau_1}e^{j\omega_1(t-u)}E\left[y_{r1}(t){y_{r1}}^*(u)\right]dtdu\right. \\ &\left. + \iint_{-\infty}^{\infty}\tilde{x_r}^*(t-\tau)\frac{\partial^2 x_r(u-\tau)}{\partial\tau_1^2}e^{j\omega_1(t-u)}E\left[y_{r1}(t){y_{r1}}^*(u)\right]dtdu\right\}. \end{aligned} \tag{4.27}$$

The correlation of $y_{r1}(t)$ is,

$$E[y_{r1}(t){y_{r1}}^*(u)] = E_r\tilde{x_r}(t-\tau_1)\tilde{x_r}^*(u-\tau_1)e^{j\omega_1(t-u)} + N_{er}\delta(t-u) \tag{4.28}$$

$$\begin{aligned} J_{11} = &-2Z'\left\{\bar{E}_r\left|\int_{-\infty}^{\infty}\frac{\partial\tilde{x_r}(t-\tau_1)}{\partial t}\tilde{x_r}^*(t-\tau_1)dt\right|^2 + \operatorname{Re}\left[\bar{E}_r\int_{-\infty}^{\infty}|\tilde{x_r}(t-\tau_1)|^2dt\int_{-\infty}^{\infty}\frac{\partial^2\tilde{x_r}^*(u-\tau_1)}{\partial\tau_1^2}\tilde{x_r}(u-\tau_1)du\right]\right. \\ &\left. +N_{er}\int_{\infty}^{\infty}\left|\frac{\partial\tilde{x}(t-\tau_1)}{\partial t}\right|^2dt + \operatorname{Re}\left[N_{er}\int_{-\infty}^{\infty}\tilde{x_r}(t-\tau_1)\frac{\partial^2\tilde{x_r}^*(t-\tau_1)}{\partial\tau_1^2}dt\right]\right\}, \end{aligned} \tag{4.29}$$

where Re denotes the real part of the signal component. To simplify the above expression consider the following:

$$\int_{-\infty}^{\infty}|\tilde{x_r}(t-\tau_1)|^2dt = 1 \tag{4.30}$$

As we know, the signal energy does not depend on the time delay. Thus differentiating (4.30) with respect to τ_1, then

$$\operatorname{Re}\left\{\int_{-\infty}^{\infty}\left[\frac{\partial\tilde{x_r}(t-\tau_1)}{\partial\tau_1}\tilde{x_r}^*(t-\tau_1)\right]dt\right\} = 0 \tag{4.31}$$

we again differentiate the above expression, then

$$\operatorname{Re}\left\{\int_{-\infty}^{\infty}\left(\frac{\partial^2\tilde{x_r}(t-\tau_1)}{\partial\tau_1^2}\tilde{x_r}^*(t-\tau_1) + \frac{\partial\tilde{x_r}(t-\tau_1)}{\partial\tau_1}\frac{\partial\tilde{x_r}^*(t-\tau_1)}{\partial\tau_1}\right)dt\right\} = 0 \tag{4.32}$$

Hence,

$$\operatorname{Re}\left[\int_{-\infty}^{\infty}\frac{\partial^2\tilde{x_r}^*(t-\tau_1)}{\partial\tau_1^2}\tilde{x_r}(t-\tau_1)dt\right] = -\int_{-\infty}^{\infty}\left|\frac{\partial\tilde{x_r}(t-\tau_1)}{\partial\tau_1}\right|^2dt, \tag{4.33}$$

from (4.29) third term and fourth term cancel each other. Further, concerning Parseval's theorem, the first term represents $\overline{\omega_1}^2$, and the third term represents $\overline{\omega_1^2}$. According to the above results,

$$J_{11} = 2Z'\bar{E}_r\left[\overline{\omega_1^2} - (\bar{\omega_1})^2\right] \tag{4.34}$$

In the same way, the remaining elements of the fisher information matrix elements can be evaluated. Moreover, the derivation of J_{12} and J_{21} is identical. Similarly,

$$J_{12} = J_{21} = 2Z'\bar{E}_r \left[\overline{\omega_1 t} - \bar{\omega_1}\bar{t}\right] \tag{4.35}$$

$$J_{22} = 2Z'\bar{E}_r \left[\overline{t^2} - (\bar{t})^2\right] \tag{4.36}$$

Eventually, the Fisher information matrix for a given received radar signal measurement is provided by,

$$\mathbf{J} = \frac{2\bar{E}_r}{N_{er}} \left(\frac{\bar{E}_r}{\bar{E}_r + N_{er}} \right) \begin{bmatrix} \overline{\omega_1^2} - (\bar{\omega_1})^2 & \overline{\omega_1 t} - \bar{\omega_1}\bar{t} \\ \overline{\omega_1 t} - \bar{\omega_1}\bar{t} & \overline{t^2} - (\bar{t})^2 \end{bmatrix} \tag{4.37}$$

Generally, the meantime and mean frequency are equal to zero. Any designated time-domain waveform assures symmetry concerning the origin by considering the mean as zero. In addition, a zero-mean frequency signifies the transmitted radar waveform envelope has zero carrier frequency. Hence the above equation (4.37) is updated as,

$$\mathbf{J} = \frac{2\bar{E}_r}{N_{er}} \left(\frac{\bar{E}_r}{\bar{E}_r + N_{er}} \right) \begin{bmatrix} \overline{\omega_1^2} & \overline{\omega_1 t} \\ \overline{\omega_1 t} & \overline{t^2} \end{bmatrix} \tag{4.38}$$

Further, the waveform parameter vector's contribution and signal-to-error noise ratio (γ_{se}) can be isolated. Hence, the Fisher information matrix ($\mathbf{J}$) is expressed as,

$$\mathbf{J} = \gamma_{se}\ \mathbf{U}(\mathbf{\Theta_k}), \tag{4.39}$$

here $\gamma_{se} = \frac{2\bar{E}_r}{N_{er}} \left(\frac{\bar{E}_r}{\bar{E}_r + N_{er}} \right)$, $\mathbf{U}(\mathbf{\Theta_k}) = \begin{bmatrix} \overline{\omega_1^2} & \overline{\omega_1 t} \\ \overline{\omega_1 t} & \overline{t^2} \end{bmatrix}$, and $\bar{t}$ represents the mean time $\bar{\omega}$ represents the mean frequency of the received waveform envelope. Further, $\overline{t^2}$ signifies the mean squared value of time, $\overline{\omega_1^2}$ signifies the mean squared value of the frequency. Whereas $\bar{E}_r$ represents the average energy of the target return, and N_{er} represents the residual noise power corresponding to the strong radar return.

1(b) Communication measurement ($y_{c1}(t)$)

The log-likelihood function concerning the communication measurement (4.6) is given by,

$$\ln \Lambda\left(\tau_1, \omega_1\right) = \frac{1}{N_0 + N_{er}} \frac{\bar{E}_c}{\bar{E}_c + N_0 + N_{er}} \left\{ \left| L(\tau_1, \omega_1) \right|^2 \right\}, \tag{4.40}$$

here,

$$L(\tau_1, \omega_1) = \int_{\infty}^{\infty} y_c(t)\tilde{x_c}^*(t-\tau_1)\exp^{-j\omega_1 t}\,dt \tag{4.41}$$

from (4.40),

$$\frac{\partial \ln \Lambda(\tau_1,\omega_1)}{\partial \tau_1} = Z'\left[L(\tau_1,\omega_1)\frac{\partial L^*(\tau_1,\omega_1)}{\partial \tau_1} + \frac{\partial L(\tau_1,\omega_1)}{\partial \tau_1}L^*(\tau_1,\omega_1)\right],$$

$$= 2Z'\,\mathrm{Re}\left[L(\tau_1,\omega_1)\frac{\partial L^*(\tau_1,\omega_1)}{\partial \tau_1}\right], \tag{4.42}$$

here,

$$Z' \triangleq \frac{1}{N_0+N_{er}}\frac{\bar{E}_c}{\bar{E}_c+N_0+N_{er}} \tag{4.43}$$

Subsequently, the following derivatives are needed to evaluate the elements of the Fisher information matrix (**J**),

$$\frac{\partial^2 \ln \Lambda(\tau_1,\omega_1)}{\partial \tau_1^2} = 2Z'\,\mathrm{Re}\left[\frac{\partial L(\tau_1,\omega_1)}{\partial \tau_1}\cdot\frac{\partial L^*(\tau_1,\omega_1)}{\partial \tau_1} + L(\tau_1,\omega_1)\frac{\partial^2 L^*(\tau_1,\omega_1)}{\partial \tau_1^2}\right] \tag{4.44}$$

$$\frac{\partial^2 \ln \Lambda(\tau_1,\omega_1)}{\partial \tau_1 \partial \omega_1} = 2Z'\,\mathrm{Re}\left[\frac{\partial L(\tau_1,\omega_1)}{\partial \omega_1}\cdot\frac{\partial L^*(\tau_1,\omega_1)}{\partial \tau_1} + L(\tau_1,\omega_1)\frac{\partial^2 L^*(\tau_1,\omega_1)}{\partial \tau_1 \partial \omega_1}\right] \tag{4.45}$$

$$\frac{\partial^2 \ln \Lambda(\tau_1,\omega_1)}{\partial \omega_1^2} = 2Z'\,\mathrm{Re}\left[\frac{\partial L(\tau_1,\omega_1)}{\partial \omega_1}\frac{\partial L^*(\tau_1,\omega_1)}{\partial \omega_1} + L(\tau_1,\omega_1)\frac{\partial^2 L^*(\tau_1,\omega_1)}{\partial \omega_1^2}\right] \tag{4.46}$$

$$J_{11} = -E\left\{\frac{\partial^2 \ln \Lambda(\tau_1,\omega_1)}{\partial \tau_1^2}\right\} \tag{4.47}$$

$$\begin{aligned} &= -2Z'\left\{\int_{-\infty}^{\infty}\frac{\partial \tilde{x_c}^*(t-\tau_1)}{\partial \tau_1}\frac{\partial \tilde{x_c}(u-\tau_1)}{\partial \tau_1}e^{j\omega_1(t-u)}E\left[y_{c1}(t){y_{c1}}^*(u)\right]dtdu\right. \\ &\quad\left.+\iint_{-\infty}^{\infty}\tilde{x_c}^*(t-\tau)\frac{\partial^2 x_c(u-\tau)}{\partial \tau_1^2}e^{j\omega_1(t-u)}E\left[y_{c1}(t){y_{c1}}^*(u)\right]dtdu\right\}. \end{aligned} \tag{4.48}$$

The correlation of $y_{c1}(t)$ is,

$$E[y_{c1}(t){y_{c1}}^*(u)] = E_c\tilde{x_c}(t-\tau_1)\tilde{x_c}^*(u-\tau_1)e^{j\omega_1(t-u)} + N_0\delta(t-u) + N_{er}\delta(t-u) \tag{4.49}$$

$$\begin{aligned} J_{11} = &-2Z'\left\{\bar{E}_c\left|\int_{-\infty}^{\infty}\frac{\partial \tilde{x_c}(t-\tau_1)}{\partial t}\tilde{x_c}^*(t-\tau_1)dt\right|^2 + N_0\int_{-\infty}^{\infty}\left|\frac{\partial \tilde{x_c}(t-\tau_1)}{\partial t}\right|^2 dt\right. \\ &+\mathrm{Re}\left[N_0\int_{-\infty}^{\infty}\tilde{x_c}(t-\tau_1)\frac{\partial^2 \tilde{x_c}^*(t-\tau_1)}{\partial \tau_1^2}dt\right] + \mathrm{Re}\left[\bar{E}_c\int_{-\infty}^{\infty}|\tilde{x_c}(t-\tau_1)|^2dt\int_{-\infty}^{\infty}\frac{\partial^2 \tilde{x_c}^*(u-\tau_1)}{\partial \tau_1^2}\tilde{x_c}(u-\tau_1)du\right] \\ &\left.+N_{er}\int_{-\infty}^{\infty}\left|\frac{\partial \tilde{x_c}(t-\tau_1)}{\partial t}\right|^2 dt + \mathrm{Re}\left[N_{er}\int_{-\infty}^{\infty}\tilde{x_c}(t-\tau_1)\frac{\partial^2 \tilde{x_c}^*(t-\tau_1)}{\partial \tau_1^2}dt\right]\right\}, \end{aligned} \tag{4.50}$$

where Re denotes the real part of this signal component. To further simplify the above equation by considering the following:

$$\int_{-\infty}^{\infty}|\tilde{x_c}(t-\tau_1)|^2dt = 1, \tag{4.51}$$

it is known that the waveform energy does not rely on the delay. So differentiating (4.51) with respect to τ_1, then

$$\mathrm{Re}\left\{\int_{-\infty}^{\infty}\left[\frac{\partial\tilde{x_c}(t-\tau_1)}{\partial\tau_1}\tilde{x_c}^*(t-\tau_1)\right]dt\right\}=0, \tag{4.52}$$

we again differentiate the above equation, then

$$\mathrm{Re}\left\{\int_{-\infty}^{\infty}\left(\frac{\partial^2\tilde{x_c}(t-\tau_1)}{\partial\tau_1^2}\tilde{x_c}^*(t-\tau_1)+\frac{\partial\tilde{x_c}(t-\tau_1)}{\partial\tau_1}\frac{\partial\tilde{x_c}^*(t-\tau_1)}{\partial\tau_1}\right)dt\right\}=0, \tag{4.53}$$

hence,

$$\mathrm{Re}\left[\int_{-\infty}^{\infty}\frac{\partial^2\tilde{x_c}^*(t-\tau_1)}{\partial\tau_1^2}\tilde{x_c}(t-\tau_1)dt\right]=-\int_{-\infty}^{\infty}\left|\frac{\partial\tilde{x_c}(t-\tau_1)}{\partial\tau_1}\right|^2dt \tag{4.54}$$

from (4.50) second term, third term, and fifth term, sixth term are canceling each other. Further based on Parseval's theorem, the first term represents $\overline{\omega_1}^2$, and the third term represents $\overline{\omega_1{}^2}$. Concerning the above results,

$$J_{11}=2Z'\bar{E}_c\left[\overline{\omega_1^2}-(\bar{\omega_1})^2\right] \tag{4.55}$$

In the same way, the remaining elements of the fisher information matrix elements can be evaluated. Moreover, the derivation of J_{12} and J_{21} is identical. Similarly,

$$J_{12}=J_{21}=2Z'\bar{E}_c\left[\overline{\omega_1 t}-\bar{\omega_1}\bar{t}\right] \tag{4.56}$$

$$J_{22}=2Z'\bar{E}_c\left[\overline{t^2}-(\bar{t})^2\right] \tag{4.57}$$

Eventually, the fisher information matrix for a given received signal is provided by,

$$\mathbf{J}=\frac{2\bar{E}_c}{N_0+N_{er}}\left(\begin{array}{c}\frac{\bar{E}_c}{\bar{E}_c+N_0+N_{er}}\end{array}\right)\left[\begin{array}{cc}\overline{\omega_1^2}-(\bar{\omega_1})^2 & \overline{\omega_1 t}-\bar{\omega_1}\bar{t}\\ \overline{\omega_1 t}-\bar{\omega_1}\bar{t} & \overline{t^2}-(\bar{t})^2\end{array}\right] \tag{4.58}$$

Generally, the meantime and mean frequency are equal to zero. Any time-domain waveform assures symmetry concerning the origin by considering the mean as zero. In addition, a zero-mean frequency signifies the communication transmitted waveform envelope has zero carrier frequency. Thus above equation (4.58) is modified as,

$$\mathbf{J}=\frac{2\bar{E}_c}{N_0+N_{er}}\left(\begin{array}{c}\frac{\bar{E}_c}{\bar{E}_c+N_0+N_{er}}\end{array}\right)\left[\begin{array}{cc}\overline{\omega_1^2} & \overline{\omega_1 t}\\ \overline{\omega_1 t} & \overline{t^2}\end{array}\right] \tag{4.59}$$

Further, the waveform parameter vector's contribution and signal-to-error noise ratio (γ_{se}) can be isolated. Hence, the Fisher information matrix ($\mathbf{J}$) is expressed as,

$$\mathbf{J}=\gamma_{se}\ \mathbf{U}(\mathbf{\Theta_k}), \tag{4.60}$$

here $\gamma_{se} = \frac{2\bar{E}_c}{N_0+N_{er}} \left(\frac{\bar{E}_c}{\bar{E}_c+N_0+N_{er}} \right)$ and $\mathbf{U}(\mathbf{\Theta_k}) = \begin{bmatrix} \overline{\omega_1^2} & \overline{\omega_1 t} \\ \overline{\omega_1 t} & \overline{t^2} \end{bmatrix}$

Similarly, the Fisher Information Matrix ($\mathbf{J}$) can be evaluated for the case of strong communication return.

Case 2: Strong communication return

2(a) Radar measurement ($y_{r2}(t)$)

The Fisher information matrix for a given radar measurement (4.8) is expressed as,

$$\mathbf{J} = \frac{2\bar{E}_r}{N_0 + N_{ec}} \left(\frac{\bar{E}_r}{\bar{E}_r+N_0+N_{ec}} \right) \begin{bmatrix} \overline{\omega_1^2} & \overline{\omega_1 t} \\ \overline{\omega_1 t} & \overline{t^2} \end{bmatrix} \tag{4.61}$$

In addition, the waveform parameter vector's contribution and signal-to-error noise ratio (γ_{se}) can be isolated. Hence, the Fisher information matrix ($\mathbf{J}$) is expressed as,

$$\mathbf{J} = \gamma_{se}\ \mathbf{U}(\mathbf{\Theta_k}), \tag{4.62}$$

here $\gamma_{se} = \frac{2\bar{E}_r}{N_0+N_{ec}} \left(\frac{\bar{E}_r}{\bar{E}_r+N_0+N_{ec}} \right)$, $\mathbf{U}(\mathbf{\Theta_k}) = \begin{bmatrix} \overline{\omega_1^2} & \overline{\omega_1 t} \\ \overline{\omega_1 t} & \overline{t^2} \end{bmatrix}$ and N_{ec} represent the residual noise power corresponding to the strong communication return.

2(b) Communication measurement ($y_{c2}(t)$)

The Fisher information matrix for a given radar measurement (4.9) is expressed as,

$$\mathbf{J} = \frac{2\bar{E}_c}{N_{ec}} \left(\frac{\bar{E}_c}{\bar{E}_c+N_{ec}} \right) \begin{bmatrix} \overline{\omega_1^2} - (\bar{\omega_1})^2 & \overline{\omega_1 t} - \bar{\omega_1}\bar{t} \\ \overline{\omega_1 t} - \bar{\omega_1}\bar{t} & \overline{t^2} - (\bar{t})^2 \end{bmatrix} \tag{4.63}$$

In addition, the waveform parameter vector's contribution and signal-to-error noise ratio (γ_{se}) can be isolated. Hence, the Fisher information matrix ($\mathbf{J}$) is expressed as,

$$\mathbf{J} = \gamma_{se}\ \mathbf{U}(\mathbf{\Theta_k}), \tag{4.64}$$

here $\gamma_{se} = \frac{2\bar{E}_c}{N_{ec}} \left(\frac{\bar{E}_c}{\bar{E}_c+N_{ec}} \right)$ and $\mathbf{U}(\mathbf{\Theta_k}) = \begin{bmatrix} \overline{\omega_1^2} & \overline{\omega_1 t} \\ \overline{\omega_1 t} & \overline{t^2} \end{bmatrix}$

By substituting (4.64) into (4.14), the measurement noise covariance matrix is expressed as,

$$\mathbf{N}(\mathbf{\Theta_k}) = \frac{1}{\gamma}\mathbf{T}\mathbf{U}(\mathbf{\Theta_k})^{-\mathbf{1}}\mathbf{T}^T \tag{4.65}$$

4.2.2 Calculation of Measurement Noise Covariance Matrix ($\mathbf{N}(\mathbf{\Theta_k})$)

In the current work, the measurement noise covariance matrix is computed for Linear Frequency Modulated (LFM) pulse radar waveform, Non-Linear Frequency Modu-

Table 4.1: Parameters considered for evaluating the measurement noise covariance matrix

Parameter	Value
Bandwidth (B)	5 MHz
Carrier frequency (f)	3 GHz
Target range of a radar system (R)	100 km
Antenna gain of a radar (G_r)	40 dBi
Radar transmitted power (P_t)	200 KW
Target cross-section area of a radar (σ_a)	30 m^2
Temperature (T_k)	1000 K
Boltzmann constant (K_B)	1.38x10^{-23} J/K
Overall communication antenna gain and propagation loss (b)	6.33x10^{-13}
Transmitted communication signal power (P_{comm})	300 mW
Range fluctuation process variance ($\sigma_f{}^2$)	25 m^2
Time-bandwidth product (TB)	128
Range of the communication system	10 km

lated (NLFM) pulse radar waveform, and Quadrature Amplitude Modulated (QAM) communication waveform.

Case 1: Strong radar target return

1(a) Radar measurement ($y_{r1}(t)$)

Firstly, a Linear Frequency Modulated (LFM) pulse radar waveform is considered for target detection. In addition, it is more appropriate for pulse compression to accomplish high-range resolution. Mathematically, LFM-pulse radar waveform is expressed as,

$$\tilde{x_r}(t) = A_1 \cos\left(\pi \frac{B_1}{\tau_1} t^2\right) \quad -\frac{\tau_1}{2} \leq t \leq \frac{\tau_1}{2}, \tag{4.66}$$

where, A_1 is the LFM pulse amplitude, B_1 denotes the bandwidth of the LFM-pulse waveform, and τ_1 indicates the pulse duration.

$$\tilde{X_r}(\omega_1) \approx |\tilde{X_r}(\omega_1)| \exp\left(-j\frac{1}{4\pi}\frac{\tau_1}{B_1}\omega_1^2\right) \exp\left(j\frac{\pi}{4}\right), \tag{4.67}$$

where $|\tilde{X}_r(\omega_1)| \approx 1, -\pi B_1 \leq \omega_1 \leq \pi B_1$ and for all the remaining ω_1 values $|\tilde{X}_r(\omega_1)| = 0$.

According to the strong radar target return ($y_{r1}(t)$), the measurement noise covariance matrix is computed as follows:

With reference to (4.65), the elements of $\mathbf{U}(\mathbf{\Theta_k})$ matrix are $\overline{\omega_1^2} = \frac{2\pi^3 {B_1}^3}{3}$, $\overline{t^2} = \frac{A_1^2 \tau_1^3}{12}$ and $\overline{\omega_1 t} = \frac{A_1^2 \tau_1^2 \pi B_1}{6}$

The measurement noise covariance matrix is obtained as,

$$\mathbf{N}(\mathbf{\Theta_k}) = \beta \begin{bmatrix} \frac{3c^2 A_1^2 \tau_1^3}{4\gamma_{se}} & \frac{-3c^2 {A_1}^2 \tau_1^2 \pi B_1}{2\omega_c \gamma_{se}} \\ \frac{-3c^2 {A_1}^2 \tau_1^2 \pi B_1}{2\omega_c \gamma_{se}} & \frac{6c^2 \pi^3 {B_1}^3}{\gamma_{se} {\omega_c}^2} \end{bmatrix}, \tag{4.68}$$

where $\beta = \left(\frac{1}{A_1^2 B_1^2 \tau_1^2 \pi^2 (2\tau_1 \pi B_1 - A_1^2 \tau_1^2)} \right)$, and $\gamma_{se} = \frac{2\bar{E}_r}{N_{er}} \left(\frac{\bar{E}_r}{\bar{E}_r + N_{er}} \right)$

$|\mathbf{N}(\mathbf{\Theta_k})| = \beta^2 \left(\frac{18c^4 \pi^3 \tau_1^3 {A_1}^2 {B_1}^3 - 9c^4 \pi^2 \tau_1^4 {A_1}^4 {B_1}^2}{4 {\gamma_{se}}^2 {\omega_c}^2} \right)$.

From the above expression, it is noticed that, $|\mathbf{N}(\mathbf{\Theta_k})|$ can be reduced by choosing optimum waveform bandwidth ($B_{1_{opt}}$) and high signal-to-error noise ratio (γ_{se}) value. Thus the selection of the waveform parameter vector ($\mathbf{\Theta_k}$) is provided by the following objective function,

$$\begin{aligned} \underset{\mathbf{\Theta_k}}{\text{minimize}} \quad & |\mathbf{N}(\mathbf{\Theta_k})|, \\ \text{subject to} \quad & \gamma_{se_{max}} \\ & B_{1_{opt}} \end{aligned} \quad , \tag{4.69}$$

Where $\mathbf{\Theta_k}$ signifies the received radar waveform parameter vector at the time instant k. In addition, the maximized signal-to-error noise ratio ($\gamma_{se_{max}}$) and optimum signal bandwidth ($B_{1_{opt}}$) are the waveform constraints (tunable waveform parameters) of the optimization problem (4.69). Concerning the tunable parameters of the LFM-pulse radar waveform, the measurement noise covariance can be minimized such that an improved radar target tracking performance can be achieved in the CRCS.

1(b) Communication measurement ($y_{c1}(t)$)

To obtain the communication measurement, a Quadrature Amplitude Modulated (QAM) signal is considered for transmitting the information. However, in the proposed scenario, the communication signal is reflected off the target and is used to improve the target estimation accuracy. It is known that the QAM signal is widely used for data transfer in WiFi communication systems. Mathematically QAM signal

for the transmission of k^{th} signal vector is represented as,

$$\tilde{x}_{ck}(t) = s_{I,k}\psi_I(t) + s_{Q,k}\psi_Q(t) \tag{4.70}$$

Here $\psi_I(t)$, $\psi_Q(t)$ are the basis functions, $s_{I,k}$ represents the in-phase signal amplitude, and $s_{Q,k}$ represents the quadrature-phase signal amplitude. In addition, the overall QAM signal amplitude and phase of a k^{th} signal vector is defined as,

$$\begin{aligned} A_k &= \|\mathbf{s}_k\| = \sqrt{s_{I,k}^2 + s_{Q,k}^2} \\ \Theta_k &= -\tan\frac{s_{Q,k}}{s_{I,k}} \end{aligned} \tag{4.71}$$

$$\begin{aligned} \tilde{x_c}(t) =& A_k P_T(t)\cos\left(\omega_c t + \Theta_k\right), m = 1, 2, \ldots, M_1; \\ & n = 1, 2, \ldots, M_2 \end{aligned} \tag{4.72}$$

here $P_T(t)$ represents the impulse response of the pulse-shaping filter and ω_c is the carrier frequency. In the current scenario, the raised cosine filter is used as a pulse-shaping filter.

$$\begin{aligned} \tilde{X_c}(\omega_1) =& \frac{A_k}{2}\cos(\Theta_k)\left[P(\omega_1 - \omega_c) + P(\omega_1 + \omega_c))\right] \\ & + j\frac{A_k}{2}\sin(\Theta_k)\left[P(\omega_1 - \omega_c) - P(\omega_1 + \omega_c))\right] \end{aligned}, \tag{4.73}$$

here, the frequency response of the raised cosine filter is provided by,

$$P(f_1) = \begin{cases} T_s & |f_1| \leq \frac{1-\beta_r}{2T}, \\ \frac{T_s}{2}\left[1 + \cos\left(\frac{\pi T_s}{\beta_r}\right)\left[|f_1| - \frac{1-\beta_r}{2T}\right]\right], & A_1 < |f_1| \leq B_1, \\ 0 & otherwise, \end{cases}$$

here $A_1 = \frac{1-\beta_r}{2T_s}$, $B_1 = \frac{1+\beta_r}{2T_s}$, and β_r represents the roll-off factor. Subsequently, the impulse response of the raised cosine filter is given by,

$$P_T(t) = \frac{\cos\left(\pi\beta_r\frac{t}{T}\right)}{1 - \left(2\beta_r\frac{t}{T}\right)^2} \times \frac{\sin(\frac{\pi t}{T})}{(\frac{\pi t}{T})}, \tag{4.74}$$

here $P_T(t)$ has zero crossings at $t = \pm T, \pm 2T, \ldots$. However, we have considered the ideal scenario of a raised cosine filter, where the roll of factor (β_r) is 0.

Concerning the communication measurement, the measurement noise covariance matrix is evaluated as follows:

According to (4.65) the matrix elements of $U(\Theta_k)$ are $\overline{\omega_1^2} = \frac{{T_s}^2{A_k}^2\pi^3{B_1}^3}{3}$, $\overline{t^2} = \frac{A_k^2 T_s^3}{\pi^2}$ and $\overline{\omega_1 t} = \frac{2T_s}{\pi}$

The measurement noise covariance matrix is evaluated as,

$$\mathbf{N}(\mathbf{\Theta_k}) = \alpha_1 \begin{bmatrix} \frac{c^2 A_k^2 T_s^3}{4\gamma_{se}\pi^2} & \frac{-c^2 T_s}{2\pi\gamma_{se}\omega_c} \\ \frac{-c^2 T_s}{2\pi\gamma_{se}\omega_c} & \frac{c^2 {T_s}^2 {A_k}^2 \pi^3 {B_1}^3}{12\gamma_{se}{\omega_c}^2} \end{bmatrix}, \tag{4.75}$$

where $\alpha_1 = \left(\frac{3\pi^2}{T_s^5 A_k^4 \pi^3 B_1^3 - 12\pi^2 T_s^2)}\right)$, $\gamma_{se} = \frac{2\bar{E}_c}{N_0+N_{er}}\left(\frac{\bar{E}_c}{\bar{E}_c+N_0+N_{er}}\right)$ From (4.75), $\mathbf{N}(\mathbf{\Theta_k})$ can be minimized by maximizing the signal-to-error noise-ratio (γ_{se}).

Case 2: Strong communication return

2(a) Radar measurement ($y_{r2}(t)$)

In the case of strong communication return, the radar measurement $y_{r2}(t)$ is provided in (4.8). Here a Non-Linear Frequency Modulated (NLFM) pulse radar waveform is considered for target state estimation. The NLFM pulse radar waveform is widely preferred due to its flexibility and low side-lobe ratio (Mahipathi et al. 2021). A second-order NLFM phase polynomial is expressed as,

$$\tilde{x_r}(t) = \mathrm{e}^{i\pi\left(p_1 B_1^2 t^2 + p_2 {B_1}^4 t^4\right)} \quad -\frac{\tau_1}{2} \leq t \leq \frac{\tau}{2}, \tag{4.76}$$

where p_1, and p_2 are the optimized phase coefficients of the NLFM phase polynomial, and B_1 represents the bandwidth of the NLFM pulse waveform. According to the Principle of Stationary Phase (PSP) approximation, the spectrum of the signal is expressed as (Chiriyath et al. 2019),

$$\begin{aligned} \tilde{X_r}(\omega_1) &\approx 2\sqrt{\frac{-\pi}{2\Phi''(t_0,\omega_1)}}\mathrm{e}^{-i\frac{\pi}{4}}\tilde{x_r}(t_0)\,\mathrm{e}^{i\Phi(t_0,\omega_1)} \\ &= 2\sqrt{\frac{-1}{4p_1{B_1}^2 + 24p_2{B_1}^4 t_0^2}}\mathrm{e}^{-i\frac{\pi}{4}}\mathrm{e}^{i\pi\left(p_1{B_1}^2 t_0^2 + p_2{B_1}^4 t_0^4\right)} \\ &\qquad \cdot\ \mathrm{e}^{i\pi\left(p_1{B_1}^2 t_0^2 + p_2{B_1}^4 t_0^4 - 2ft_0\right)}, \end{aligned} \tag{4.77}$$

here $\Phi''(t,\omega_1) = \frac{\partial^2\Phi(t,\omega_1)}{\partial t^2} = \pi\left(2p_1{B_1}^2 + 12p_2{B_1}^4 t^2\right)$. Further, $|\tilde{X_r}(\omega_1)| \approx 1, -\pi B_1 \leq \omega_1 \leq \pi B_1$ and for all the remaining ω_1 values $|\tilde{X_r}(\omega_1)| = 0$. According to (4.5), the measurement noise covariance is evaluated as follows:

From (4.65), the matrix elements of $\mathbf{U}(\mathbf{\Theta_k})$ are: $\overline{\omega^2} = \frac{8\pi^3{B_1}^3}{3(4p_1{B_1}^2+24p_2{B_1}^4 t_0^2)}$, $\overline{t^2} = \frac{\tau^3}{12}$ and $\overline{\omega t} = \frac{\pi p_1 B_1^2 \tau^3}{6} + \frac{\pi p_2 {B_1}^4 \tau^5}{20}$

With reference to the above expressions, the matrix $\mathbf{U}(\mathbf{\Theta_k})$ is formed as,

$$\mathbf{U}(\mathbf{\Theta_k}) = \begin{bmatrix} \frac{8\pi^3{B_1}^3}{3(4p_1{B_1}^2+24p_2{B_1}^4 t_0^2)} & \frac{\pi p_1 B_1^2 \tau^3}{6} + \frac{\pi p_2 {B_1}^4 \tau^5}{20} \\ \frac{\pi p_1 B_1^2 \tau^3}{6} + \frac{\pi p_2 {B_1}^4 \tau^5}{20} & \frac{\tau^3}{12} \end{bmatrix} \tag{4.78}$$

$$\mathbf{N}(\mathbf{\Theta_k}) = \frac{1}{\alpha_2 \gamma_{se}} \mathbf{T} \begin{bmatrix} \frac{\tau^3}{12} & -\frac{\pi p_1 B_1^2 \tau^3}{6} - \frac{\pi p_2 {B_1}^4 \tau^5}{20} \\ -\frac{\pi p_1 B_1^2 \tau^3}{6} - \frac{\pi p_2 {B_1}^4 \tau^5}{20} & \frac{8\pi^3 {B_1}^3}{3(4p_1 {B_1}^2 + 24 p_2 {B_1}^4 {t_0}^2)} \end{bmatrix} \mathbf{T}^T, \tag{4.79}$$

here $\gamma_{se} = \frac{2\bar{E}_r}{N_0 + N_{ec}} \left(\frac{\bar{E}_r}{\bar{E}_r + N_0 + N_{ec}} \right)$, $\alpha_2 = |\mathbf{U}(\mathbf{\Theta_k})|$, and
$\mathbf{T} = \text{diag}\left(c/2, c/\left(2\omega_c\right)\right)$, '$c$' signifies the propagation velocity of the NLFM pulse waveform, and ω_c is the carrier frequency. In NLFM pulse waveform, phase coefficients (p_1, p_2), and signal-to-error noise ratio (γ_{se}) are the waveform constraints (tunable waveform parameters). Here the optimized phase coefficients (p_1, p_2) are computed with based on our previous work (Mahipathi et al. 2021). From (4.79), it is noticed that the measurement noise covariance can be minimized by optimizing the phase coefficients and maximizing the (γ_{se}) value. Further, by minimizing the measurement noise covariance an improved radar target tracking performance can be accomplished in the CRCS.

2(b) Communication measurement ($y_{c2}(t)$)

In this case, the measurement corresponding to the strong communication return ($y_{c2}(t)$) is exploited to estimate the target state in a CRCS configuration. Here also the QAM signal is considered for data transmission through a wireless channel to the intended receiver. Hence the measurement noise covariance matrix is expressed as,

$$\mathbf{N}(\mathbf{\Theta_k}) = \alpha_1 \begin{bmatrix} \frac{c^2 A_k^2 T_s^3}{4\gamma\pi^2} & \frac{-c^2 T_s}{2\pi\gamma\omega_c} \\ \frac{-c^2 T_s}{2\pi\gamma\omega_c} & \frac{c^2 {T_s}^2 {A_k}^2 \pi^3 {B_1}^3}{12\gamma {\omega_c}^2} \end{bmatrix}, \tag{4.80}$$

where $\alpha_1 = \left(\frac{3\pi^2}{T_s^5 A_k^4 \pi^3 B_1^3 - 12\pi^2 T_s^2)} \right)$, and $\gamma = \frac{2\bar{E}_c}{N_{ec}} \left(\frac{\bar{E}_c}{\bar{E}_c + N_{ec}} \right)$
From the above expression (4.80), $\mathbf{N}(\mathbf{\Theta_k})$ can be minimized by reducing the signal-to-error noise-ratio.

4.3 Target Tracking

This section describes target tracking in a Cooperative Radar-Communication System (CRCS). In this framework, the actual measurements (the radar direct and communication passive measurements are in polar coordinates) obtained in CRCS are directly used to obtain the converted measurements (cartesian space measurements) in an Iterative Least Squares (ILS) framework. These converted measurements are further used in a tracking framework to estimate the state of interest (the state contains the position and velocity of the target).

4.3.1 Converted Measurements based on Iterative Least Square

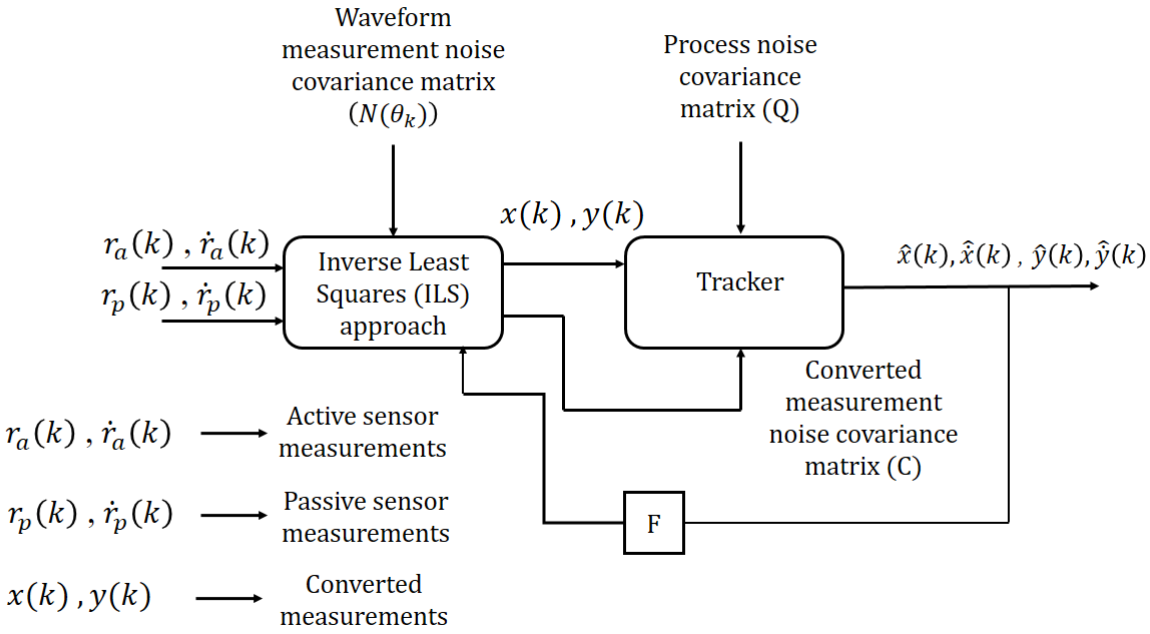

Figure 4.2: Tracking framework for CRCS

The Iterative Least Square (ILS) framework is a widely preferred approach that converges to the solution for any randomized initialization (Ding and Chen 2005, Ding et al. 2008). As shown Figure 4.2, ILS utilizes both active sensor measurements $(r_a, \dot{r}_a)$, passive sensor measurements $(r_p, \dot{r}_p)$, and waveform measurement noise covariance matrix $(N(\Theta_k))$ to attain the converted position (x, y) and converted velocity $(\dot{x}, \dot{y})$. The measurement vector for ILS is given by

$$\mathbf{z} = [r_a \quad \dot{r}_a \quad r_p \quad \dot{r}_p]^T \tag{4.81}$$

where k is the time instant, $r_a(k)$ and $\dot{r}_a(k)$ represent the range and range rate measurements at the k^{th} time instant of active radar sensors respectively. Whereas, $r_p(k)$ and $\dot{r}_p(k)$ are the range and range rate measurements at the k^{th} time instant of a passive sensor (communication signal reflected off the target) respectively. The math-

ematical model for measurements is

$$\begin{aligned} r_a &= \sqrt{x^2+y^2} + \mathcal{N}(0,\sigma_{r_a}) \\ \dot{r}_a &= \frac{x\dot{x}+y\dot{y}}{\sqrt{x^2+y^2}} + \mathcal{N}(0,\sigma_{\dot{r}_a}) \\ r_p &= \sqrt{x^2+y^2} + \sqrt{(x_c-x)^2+(y_c-y)^2} + \mathcal{N}(0,\sigma_{r_p}) \\ \dot{r}_p &= \frac{x\dot{x}+y\dot{y}}{\sqrt{x^2+y^2}} + \frac{(x_c-x)\dot{x}+(y_c-y)\dot{y}}{\sqrt{(x_c-x)^2+(y_c-y)^2}} + \mathcal{N}(0,\sigma_{\dot{r}_p}) \end{aligned} \tag{4.82}$$

It is to be observed from the above equation that, the communication location is known, and there exist four known measurements and four unknowns (position and velocity of the target). The state vector is formed by stacking all four unknowns as

$$\mathbf{y} = [x \quad \dot{x} \quad y \quad \dot{y}] \tag{4.83}$$

The linearized measurement model can be written as

$$\Delta\mathbf{z}_{itr} = \mathbf{H}_{itr}\Delta\mathbf{y}_{itr} + \mathbf{n} \tag{4.84}$$

where $\Delta\mathbf{z}_{itr} = \mathbf{z}_{itr} - \mathbf{z}_{itr-1}$, $\Delta\mathbf{y}_{itr} = \mathbf{y}_{itr} - \mathbf{y}_{itr-1}$, and $\mathbf{H}_{itr}$ is the measurement transition evaluated at the iteration. Meanwhile, the $\mathbf{n}$ is a stacked vector of noise components which are following Gaussian distribution with zero mean and covariance $\mathbf{C}$. It is worth noting that the covariance matrix is calculated from the waveform parameter vector from the section and is equivalent to $\mathbf{N}(\mathbf{\Theta}) = \mathbb{E}\{\mathbf{nn}'\}$. The measurement transition matrix ($\mathbf{H}$) is expressed as

$$\mathbf{H} = \begin{bmatrix} \frac{\partial r_a}{\partial x} & \frac{\partial r_a}{\partial \dot{x}} & \frac{\partial r_a}{\partial y} & \frac{\partial r_a}{\partial \dot{y}} \\ \frac{\partial \dot{r}_a}{\partial x} & \frac{\partial \dot{r}_a}{\partial \dot{x}} & \frac{\partial \dot{r}_a}{\partial y} & \frac{\partial \dot{r}_a}{\partial \dot{y}} \\ \frac{\partial r_p}{\partial x} & \frac{\partial r_p}{\partial \dot{x}} & \frac{\partial r_p}{\partial y} & \frac{\partial r_p}{\partial \dot{y}} \\ \frac{\partial \dot{r}_p}{\partial x} & \frac{\partial \dot{r}_p}{\partial \dot{x}} & \frac{\partial \dot{r}_p}{\partial y} & \frac{\partial \dot{r}_p}{\partial \dot{y}} \end{bmatrix} \tag{4.85}$$

From (4.82), and (4.85), the measurement transition matrix is evaluated as

$$\mathbf{H} = \begin{bmatrix} \frac{x}{r_a} & 0 & \frac{y}{r_a} & 0 \\ \frac{\dot{x}}{r_a} - \frac{x\dot{r_a}}{r_a^2} & \frac{x}{r_a} & \frac{\dot{y}}{r_a} - \frac{y(\dot{r_a})}{r_a^2} & \frac{y}{r_a} \\ \frac{x}{r_a} + \frac{x-x_c}{r_p-r_a} & 0 & \frac{y}{r_a} + \frac{y-y_c}{r_p-r_a} & 0 \\ \frac{\dot{x}}{r_a} - \frac{x(\dot{r}_a)}{r_a^2} - \frac{\dot{x}}{r_p-r_a} + \frac{(x_c-x)(\dot{r}_p-\dot{r}_a)}{(r_p-r_a)^2} & \frac{x_c-x}{r_p-r_a} & \frac{\dot{y}}{r_a} - \frac{y(\dot{r}_a)}{r_a^2} - \frac{\dot{y}}{r_p-r_a} + \frac{(y_c-y)(\dot{r}_p-\dot{r}_a)}{(r_p-r_a)^2} & \frac{y_c-y}{r_p-r_a} \end{bmatrix} \tag{4.86}$$

The best linear unbiased estimator (BLUE) of the state vector is

$$\Delta\hat{\mathbf{y}} = (\mathbf{H}^T\mathbf{C}^{-1}\mathbf{H})^{-1}\mathbf{H}^T\mathbf{C}^{-1}\Delta\mathbf{z} \tag{4.87}$$

Similarly, the covariance of the estimator is

$$\mathbf{R} = \mathbf{H}^T\mathbf{C}^{-1}\mathbf{H}. \tag{4.88}$$

4.3.2 Tracking

A State Model

The target state dynamics are modeled as

$$X(k+1) = F(k)X(k) + w(k), \tag{4.89}$$

where $X(k) = [x(k)\ \dot{x}(k)\ y(k)\ \dot{y}(k)]^T$ represents a state vector and
$w = [\mathcal{N}(0,\sigma_x)\,\mathcal{N}(0,\sigma_{\dot{x}})\,\mathcal{N}(0,\sigma y)\,\mathcal{N}(0,\sigma_{\dot{y}})]^T$ is a Gaussian distributed white noise vector having zero mean and its covariance matrix is expressed as $Q(k) = \mathbb{E}[w(k)w(k)']$, here, k represents the discrete time instant, and $w(k)$ is the process noise vector due to the perturbation of the target. Moreover, $F(k)$ denotes the state transition matrix; the constant velocity (CV) model is represented as

$$F(k) = \begin{bmatrix} F_s(k) & 0_{2,2} \\ 0_{2,2} & F_s(k) \end{bmatrix}; F_s(k) = \begin{bmatrix} 1 & t_s \\ 0 & 1 \end{bmatrix}, \tag{4.90}$$

here 't_s' represents the sampling time interval.

B Measurement Model

The tracking framework takes the converted measurements and performs the tracking. The converted measurement model is

$$\mathbf{y}(k) = \mathcal{H}X(k) + \mathbf{m}(k), \tag{4.91}$$

where, $\mathbf{y}(k)$ is the converted measurement from the ILS. The measurement noise covariance corresponding to $\mathbf{m}(k)$ is $\mathbf{C}(k)$ which is obtained from the ILS covariance estimate. $\mathcal{H}$ represents a measurement transition matrix, which relates the kinematic state to the measurement given by

$$\mathcal{H} = \begin{bmatrix} 1 & 0 & 0 & 0 \\ 0 & 0 & 1 & 0 \end{bmatrix}. \tag{4.92}$$

This measurement generation is carried out under the condition of target detection probability ($p_d = 1$) and probability of false alarm ($p_{fa} = 0$). The target generation is considered to be the CV model rather than the constant turn model. The reason behind this assumption is to illustrate the significance of extracted measurement noise covariance corresponding to the waveforms. In the case of non-linear trajectories and non-linear measurement relationships, the extended Kalman filters and IMM filters are required. It is hard to illustrate the significance of the extracted measurement noise covariance matrix parameter. Hence, the rest of the filtering is carried out using the Kalman filter owing to its optimal behaviour for linearity and Gaussian assumptions.

C Filtering

Three major steps are involved in filtering: state prediction, calculation of gain, and then state updation. Firstly, the predicted state is expressed as,

$$\hat{X}(k+1 \mid k) = F\hat{X}(k \mid k) \tag{4.93}$$

subsequently, the predicted covariance is provided by,

$$P(k+1 \mid k) = FP(k \mid k)F' + Q(k) \tag{4.94}$$

The predicted measurement is expressed as,

$$\hat{z}(k+1/k) = \mathcal{H}\hat{X}(k+1 \mid k) \tag{4.95}$$

Using the predicted measurement and actual observation, the innovation is calculated as

$$\gamma = \mathbf{y}(k+1) - \hat{z}(k+1|k), \tag{4.96}$$

The gain of Kalman filter K is expressed as,

$$K(k+1) = P(k+1/k)\mathcal{H}(k+1)' \tag{4.97}$$

$$[\mathcal{H}(k+1)P(k+1/k)\mathcal{H}(k+1)' + \mathcal{R}]^{-1}, \tag{4.98}$$

here $\mathcal{R}$ represents the measurement noise covariance matrix. Based on the above equations, the updated state is given by,

$$\hat{X}(k+1 \mid k+1) = \hat{X}(k+1 \mid k) + K(k+1)\gamma(k+1) \tag{4.99}$$

subsequently, the updated covariance is provided by,

$$P(k+1 \mid k+1) = P(k+1 \mid k) - K(k+1)(k+1)K'(k+1) \tag{4.100}$$

D Initialization

A single-point initialization is used since position information is available from ILS at zero instant ([Bar-Shalom et al., 2004]). The state is initialized as

$$X(0 \mid 0) = [\hat{x} \quad 0 \quad \hat{y} \quad 0]^T \tag{4.101}$$

Similarly, the state covariance $P(0 \mid 0)$ is initialized as

$$P(0 \mid 0) = \begin{bmatrix} P(1,1) & 0 & 0 & 0 \\ 0 & \frac{V_m^2}{2} & 0 & 0 \\ 0 & 0 & P(3,3) & 0 \\ 0 & 0 & 0 & \frac{V_m^2}{2} \end{bmatrix} \tag{4.102}$$

where $P(1,1)$ and $P(3,3)$ are the tuning parameters of initial covariance. Moreover, here V_m is the maximum velocity of the target. Similarly, the measurement noise covariance is given by

$$\mathcal{R} = \mathbf{C}, \tag{4.103}$$

here, $\mathbf{C}$ is the estimated covariance from the ILS framework.

4.3.3 Posterior Cramer-Rao Lower Bound (PCRLB)

This work considers a standard theoretical lower bound i.e., Posterior Cramer Rao lower bound (PCRLB) (Bar-Shalom et al. 2010) to validate the state estimation. Let $X(k+1)$ be the state vector and estimation of the state vector concerning the measurement set $z_{1:k+1}$ is denoted as $\hat{X}(k+1)$. According to (Tichavsky et al. 1998), the PCRLB on the covariance matrix $P(k+1)$ is evaluated by taking the inverse of the Fisher Information Matrix (FIM) $(J(k+1))$.

$$P(k+1) \triangleq \mathbb{E}\left[\left(\hat{X}(k+1) - X(k+1)\right)\left(\hat{X}(k+1) - X(k+1)\right)'\right] \geq \mathbf{J(k+1)^{-1}}, \tag{4.104}$$

where,

$$\mathbf{J(k+1)} = \left[F(k)^{-1}\right]^T J(k) F(k)^{-1} + Q(k)^{-1} + H(k)^T \mathbf{N}(\mathbf{\Theta_{k+1}})^{-1} H(k) \tag{4.105}$$

Based on the measurement noise covariance matrix formula in (4.65), $\mathbf{N}(\mathbf{\Theta_{k+1}})$ is expressed as,

$$\mathbf{N}(\mathbf{\Theta_{k+1}}) = \frac{1}{\gamma}\mathbf{T}\mathbf{U}(\mathbf{\Theta_{k+1}})^{-\mathbf{1}}\mathbf{T}^{T} \tag{4.106}$$

4.4 Simulation Results and Analysis

This section presents the waveform-based target state estimation analysis with the assistance of scattered QAM communication signals in a CRCS.

4.4.1 Simulation Scenario

It is assumed that a single radar transceiver and an in-band communication transmitter are operated in the CRCS configuration. In the simulation process, it is assumed that the JRC receiver is located at the origin, and the communication transmitter is located at [3000, 5000]'. Meanwhile, at $k = 0$, the target is located at [7000, 4000]' and starts moving with a Constant Velocity (CV) of 25 m/s and 15 m/s along the x-direction and y-direction respectively. Furthermore, the target perturbations are distributed in a Gaussian manner and it is given below,

$$w = [\mathcal{N}(0, 0.01), \mathcal{N}(0, 0.01), \mathcal{N}(0, 0.01), \mathcal{N}(0, 0.01)]^{T} \tag{4.107}$$

The CRCS collects the target measurements at a sampling interval (t_s) of 1 s for 100 s. The simulation is conducted for 1000 Monte-Carlo runs.

4.4.2 ILS performance

Random initialization is used to initialize the state vector $y(0)$ with the number of iterations $itr = 15$ to estimate $\hat{y}(0)$. Further, from $k = 1$, the predicted state vector from the EKF is considered for the ILS initialization. This increases the ILS consistency. Moreover, the initial covariance of ILS is provided with $\mathbf{N}(\mathbf{\Theta_k})$. The convergence of the ILS approach for random initialization over the epoch number is shown in Figure 4.3.

4.4.3 Kalman Filter performance

The Kalman Filter (KF) consumes the measurements $\mathbf{y}$ to estimate the X and P. A single point state and covariance initialization is considered as shown in (4.101) and

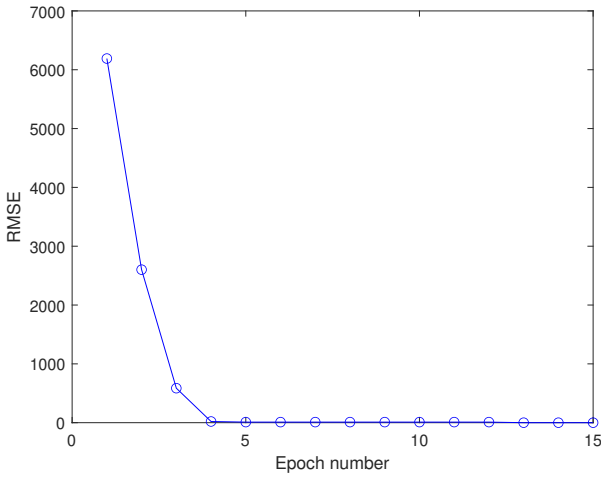

Figure 4.3: Convergence of ILS approximation

(4.102) with $V_m = 30\text{m/s}$, $P(1,1) = 2500$, and $P(3,3) = 2500$.

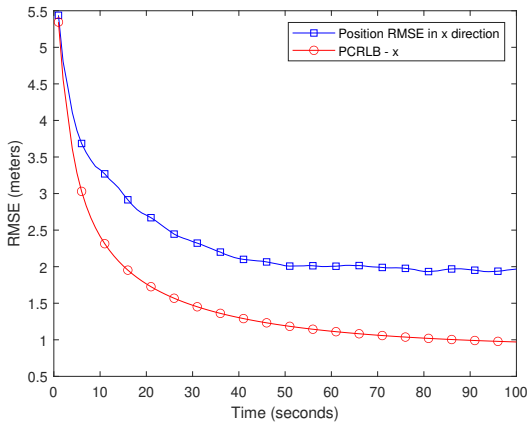

(a) PRMSE of LFM and QAM waveforms in X-direction

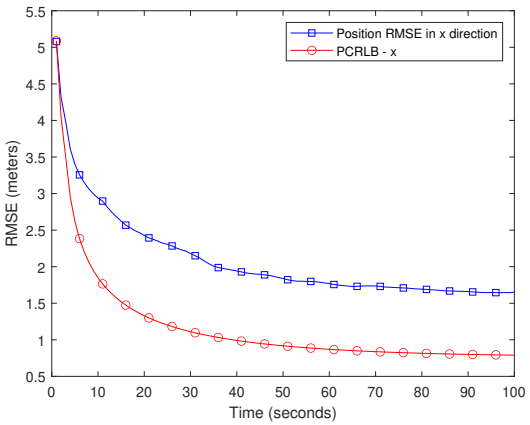

(b) PRMSE of NLFM and QAM waveforms in X-direction

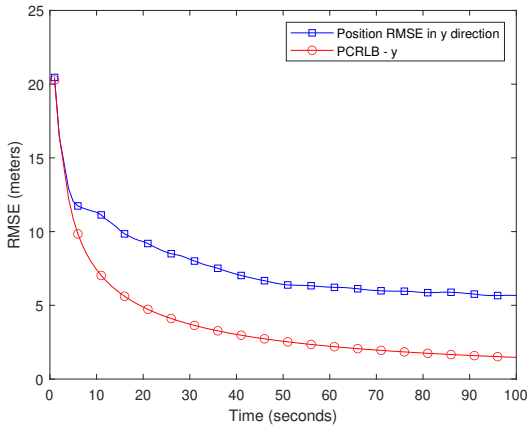

(c) PRMSE of LFM and QAM waveforms in Y-direction

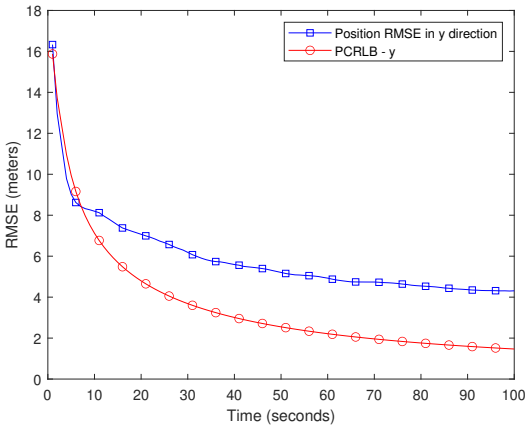

(d) PRMSE of NLFM and QAM waveforms in Y-direction

Figure 4.4: Comparison of PRMSE with the PCRLB for both the waveform combinations in a CRCS framework

In Figure 4.4, the positional estimation error of a target for the two designated combinations i.e., 1) LFM radar waveform, QAM communication waveform, and 2) NLFM radar waveform, QAM communication waveform is analyzed in terms of Root Mean Square Error (RMSE). It is observed that the position-estimated RMSE values are gradually decreasing with time along X and Y directions respectively. In addition, the positionally estimated RMSE values are validated with the Posterior Cramer-Rao Lower Bound (PCRLB) for both the designated waveform combinations. Moreover, it is evident that the combination of NLFM radar waveform and QAM communication waveform positional errors are minimal and they are approaching the PCRLB (especially along the y-direction) compared to the other combination.

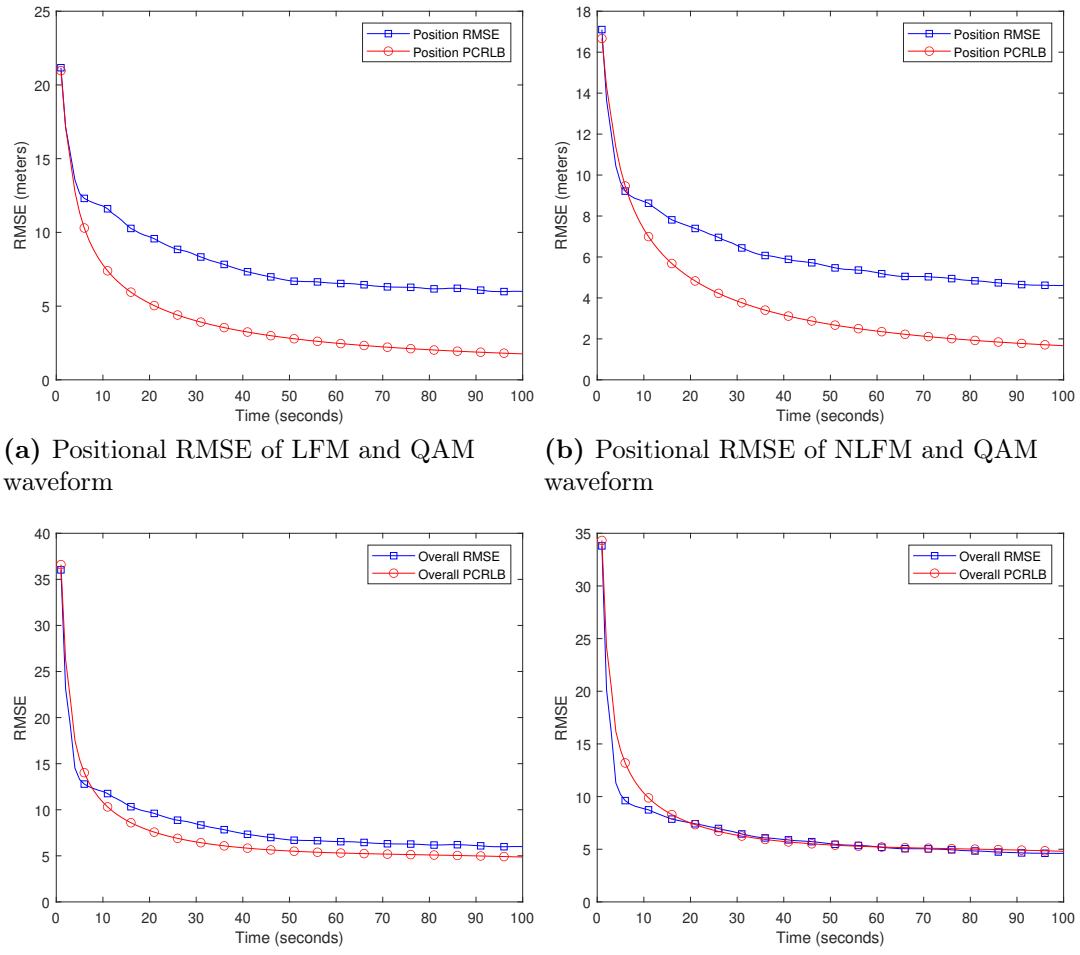

(a) Positional RMSE of LFM and QAM waveform

(b) Positional RMSE of NLFM and QAM waveform

(c) Overall RMSE of LFM and QAM waveform

(d) Overall RMSE of NLFM and QAM waveform

Figure 4.5: Comparison of Resultant PRMSE and RMSE for both the waveform combinations in a CRCS framework

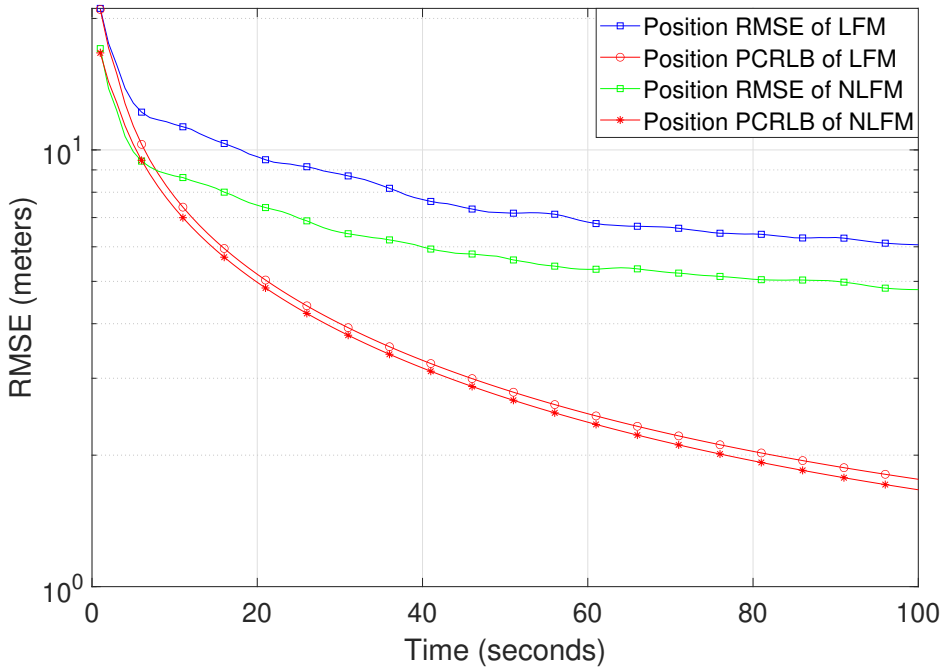

Figure 4.6: Comparison between LFM and NLFM radar waveforms in terms of positional RMSE in a CRCS environment

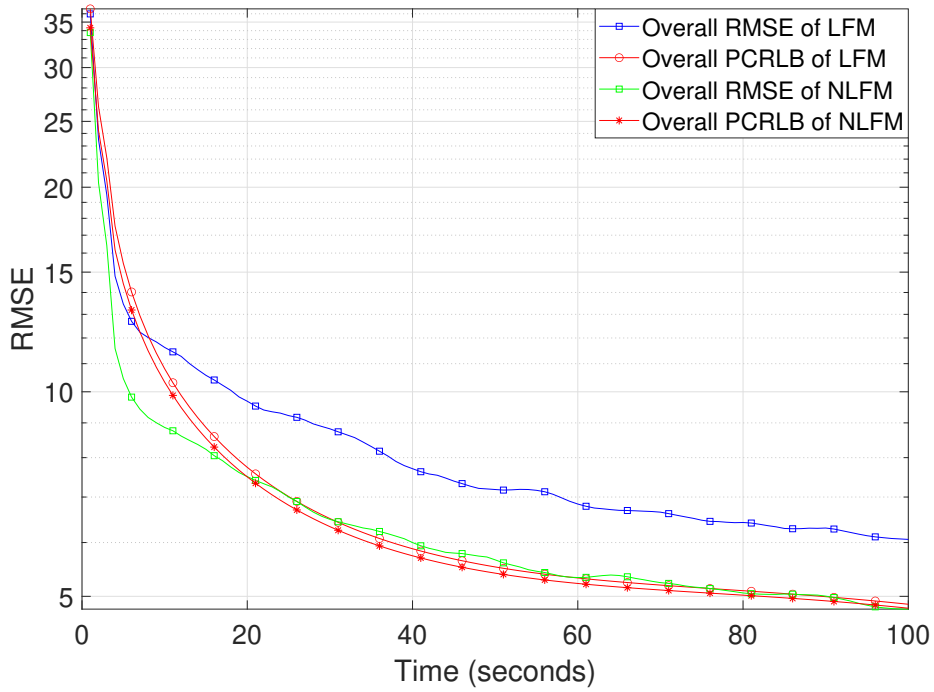

Figure 4.7: Comparison between LFM and NLFM radar waveforms in terms of overall RMSE in a CRCS environment

Subsequently, the resultant positional RMSE values are analyzed for both the designated waveform combinations in Figure 4.5. It is noticed that, as the time increases the positional estimated RMSE values are gradually decreasing for both the waveform combinations. Further, all the position-estimated RMSE values are validated with the PCRLB. It is also perceived that the optimized NLFM radar waveform with the assistance of the QAM waveform performs better compared to the other combination. In addition, the overall RMSE of both the designated combinations is also analyzed in Figure 4.5. It is perceived that the overall RMSE values are gradually decreasing as time goes on. Further, in both the waveform combinations the RMSE values are validated with the PCRLB. Furthermore, the combination of NLFM radar waveform and QAM communication waveform performs better compared to the other combination. Moreover, the overall RMSE of NLFM and QAM combination almost coincides with the PCRLB.

To give more clarity, the positional RMSE values of both the designated waveform combinations are plotted on a log-Y scale. From Figure 4.6, it is evident that the combination of NLFM radar waveform and QAM communication waveform performed better compared to other combinations (LFM radar waveform, QAM communication waveform). Whereas in Figure 4.7, the overall RMSE of both the designated waveform combinations are also plotted on a log-Y scale. It is noticed that the combination of NLFM radar waveform and QAM communication waveform minimizes the state estimation error compared to the other one. In addition, the state estimation error values corresponding to NLFM and QAM combination coincide with the PCRLB value. Hence it is recommended to have an NLFM radar waveform and a QAM communication waveform to achieve improved state estimation performance in a CRCS.

4.5 Summary

This chapter proposed a communication-aided novel measurement model to analyze the radar target tracking performance for radar and communication waveform combinations in a CRCS. Further, the NLFM radar waveform and QAM communication waveform combination performed better compared to other waveform combinations

i.e., LFM radar waveform and QAM communication waveform. The upcoming chapter provides the concluding remarks and future research directions.

Chapter 5

Conclusions and Future Research Directions

5.1 Conclusions

This thesis dealt with constrained radar waveform optimization, optimum waveform selection for target state estimation, and communication-aided target state estimation in a cooperative radar-communication system. The research work presented in this thesis has added significant domain knowledge in the area of radar signal processing.

The primary focus of this research is on proposing an SBnB global optimization-based waveform design approach, which optimizes the NLFM waveform to simultaneously enhance the performance of both radar and communication systems in the CRCS framework. We observed that the proposed SBnB approach achieved improved performance in terms of spectral characteristics compared to the existing PRC-CRLB and MEEV waveform design approaches. Further, a comprehensive analysis is carried out on the auto-correlation characteristics (the PSLR and ISLR values are calculated) to compare both the proposed and existing waveform design approaches. The proposed waveform design approaches reduce the range-domain ambiguities compared to the existing approaches. Further, the SBnB waveform design approach outperforms the MEEV, PRC-CRLB, and M-PRC-CRLB waveform design approaches in terms of PSLR and ISLR values. The proposed SBnB waveform design approach enhances the radar estimation rate compared to the MEEV, PRC-CRLB, and M-PRC-CRLB waveform design approaches. Moreover, it also accomplishes a comparable communication data rate as that of the MEEV approach. The convergence of the SBnB algorithm depends on the complexity of the objective function. However, this al-

gorithm attains only an approximated globally optimized solution for the proposed optimized framework due to its non-convexity.

The secondary focus of our research work is to develop a novel measurement model with a communication residual component to investigate the performance of a radar system in the CRCS framework. The proposed technique derived a Fisher Information Matrix (FIM), which helped in characterizing a radar sensor for the selected waveforms in the cooperative spectrum-sharing scenario. Further, the Kalman filter is deployed to estimate the target kinematics in terms of range and range rate. Among all the designated waveforms, it is apparent that the NLFM-pulse waveform provided superior performance both in terms of range and range rate RMSE values. Because the optimized NLFM-pulse waveform exhibits reduced side-lobes in the matched filter output and achieves maximum signal-to-residual noise ratio even in the absence of a side-lobe filter. It is noticed that the frequency-modulated waveforms (LFM-pulse, LFM-Gaussian pulse, and NLFM-pulse) accomplished improved performance compared to the amplitude-modulated waveforms (rectangular pulse, triangular pulse, Gaussian-pulse) in terms of range and range rate RMSE. Hence, the selection of waveform and its tunable parameters like optimal signal bandwidth, sweep rate, and signal-to-residual noise ratio plays a prominent role in achieving improved target tracking performance in the CRCS configuration.

The final work has concentrated on a communication-assisted radar measurement model as a function of the transmitted waveforms in a CRCS environment. The proposed approach derived a Fisher Information Matrix (FIM) for the two designated waveform combinations, i.e., 1) LFM radar waveform and QAM communication waveform 2)NLFM radar waveform and QAM communication waveform. Further, the measurement noise covariance matrix is evaluated for all the aforementioned waveforms for two different cases of strong radar return and strong communication return corresponding to the SIC receiver model in a CRCS. Furthermore, based on the target measurement, the target position is estimated by considering the ILS framework. By considering the ILS position estimation, the Kalman filter estimated the target trajectory. In addition, the position-estimated errors are quantified in terms of RMSE for both the designated waveform combinations. Subsequently, position-estimated RMSE values are validated with the PCRLB. The superiority of the NLFM radar waveform

and QAM communication waveform combination is noticed in the simulated results compared to the other combinations. Hence it is desirous to have an NLFM radar waveform and a QAM communication waveform to accomplish improved target state estimation in a CRCS configuration.

5.2 Future Research Directions

1. The constraint-based multi-objective optimization problems are suffering from computational complexity or high convergence time. To reduce the convergence time, there is a lot of scope for the development of optimum waveform design approaches based on recurrent neural networks and advanced machine learning algorithms.

2. In a CRCS, it is always a tedious task for the joint receiver to separate the target echo and wireless communication signal from the users in the existence of noise, interference, and clutter. To overcome this problem, one can think about considering some learning approaches like Independent Component Analysis (ICA) and machine learning algorithms for signal classification at the joint radar-communication receiver.

3. One can perform constrained-based radar waveform optimization by considering various radar waveforms for improving the performance of a CRCS.

4. The CRCS models considered in this research work can be extended for some intricate scenarios like Intelligent transportation systems, and autonomous vehicles where there is a need for convergence of radar-sensing and communication functionalities.

5. The optimal waveform selection for target state estimation can be extended by considering the non-linear motion of the target in a CRCS environment.

6. The target state estimation is carried out with a single target without clutter and Electronic Countermeasures (ECM) in a CRCS. Hence, with the proposed measurement model, one can carry out future research in the direction of single-target tracking and multiple-target tracking in the presence of clutter or ECM.

7. In addition, another research direction would be to incorporate clutter and/or intentional interference to the measurement model along with the communication residual component to perform the radar target state estimation in a CRCS.

8. One can carry out optimal waveform selection for target state estimation by considering the various CRCS configurations.

9. The communication-aided target state estimation for a CRCS can be extended by considering the different radar and communication waveforms.

10. The communication-aided target state estimation can be extended by choosing multiple targets in the presence of clutter or Electronic countermeasures (ECM) in a CRCS environment.

Bibliography

Augusto Aubry, Antonio De Maio, Marco Piezzo, and Alfonso Farina. Radar waveform design in a spectrally crowded environment via nonconvex quadratic optimization. *IEEE Transactions on Aerospace and Electronic Systems*, 50(2):1138–1152, 2014.

Augusto Aubry, Antonio De Maio, Yongwei Huang, Marco Piezzo, and Alfonso Farina. A new radar waveform design algorithm with improved feasibility for spectral coexistence. *IEEE Transactions on Aerospace and Electronic Systems*, 51(2):1029–1038, 2015.

Augusto Aubry, Vincenzo Carotenuto, Antonio De Maio, Alfonso Farina, and Luca Pallotta. Optimization theory-based radar waveform design for spectrally dense environments. *IEEE Aerospace and Electronic Systems Magazine*, 31(12):14–25, 2016a. doi: 10.1109/MAES.2016.150216.

Augusto Aubry, Vincenzo Carotenuto, Antonio De Maio, Alfonso Farina, and Luca Pallotta. Optimization theory-based radar waveform design for spectrally dense environments. *IEEE Aerospace and Electronic Systems Magazine*, 31(12):14–25, 2016b.

Babaei, Tranter, and Bose. A nullspace-based precoder with subspace expansion for radar/communications coexistence. In *2013 IEEE Global Communications Conference (GLOBECOM)*, pages 3487–3492, 2013.

Bar-Shalom and Fortmann. *Tracking and Data Association*. Boston: Academic Press, 1988. ISBN 0120797607.

Bar-Shalom, Li, and Kirubarajan. *Estimation With Applications to Tracking and Navigation: Theory Algorithms and Software*. Wiley, 2004. ISBN 9780471221272.

Bar-Shalom, Daum, and Huang. The probabilistic data association filter. *IEEE Control Systems Magazine*, 29(6):82–100, 2009. doi: 10.1109/MCS.2009.934469.

Bar-Shalom, Willet, and Tian. *Tracking Data Fusion*, volume 11 of *1st ed.* YBS Publishing, 2010. ISBN 978-93-80381-29-9.

Alessio Bellè, Mariano Falcitelli, Matteo Petracca, and Paolo Pagano. Development of ieee802. 15.7 based its services using low cost embedded systems. In *2013 13th International Conference on ITS Telecommunications (ITST)*, pages 419–425. IEEE, 2013.

Marian Bică and Visa Koivunen. Radar waveform optimization for target parameter estimation in cooperative radar-communications systems. *IEEE Transactions on Aerospace and Electronic Systems*, 55(5):2314–2326, 2018.

Blair, Watson, Kirubarajan, and Bar-Shalom. Benchmark for radar allocation and tracking in ECM. *IEEE Transactions on Aerospace and Electronic Systems*, 34(4): 1097–1114, 1998.

Bliss. Cooperative radar and communications signaling: The estimation and information theory odd couple. In *2014 IEEE Radar Conference*, pages 0050–0055, 2014. doi: 10.1109/RADAR.2014.6875553.

Bliss and Govindasamy. *Adaptive Wireless Communications: MIMO Channels and Networks*. Cambridge Univ.Press, 2013. ISBN 978-1-107-03320-7.

Blunt and Perrins. *Radar and Communication Spectrum Sharing*, chapter Radar waveform design for spectral coexistence. Scitech and an imprint of the IET, 2019.

Zbigniew R Bogdanowicz. Flying swarm of drones over circulant digraph. *IEEE Transactions on Aerospace and Electronic Systems*, 53(6):2662–2670, 2017.

John C Brock and Samuel J Purkis. The emerging role of lidar remote sensing in coastal research and resource management. *Journal of Coastal Research*, (10053): 1–5, 2009.

Chiriyath. *Fundamental Limits on Performance for Cooperative Radar-Communications Coexistence*. PhD thesis, Arizona State University, 2018.

Chiriyath, Paul, and Bliss. Joint radar-communications information bounds with clutter: The phase noise menace. In *2016 IEEE Radar Conference (RadarConf)*, pages 1–6, 2016a. doi: 10.1109/RADAR.2016.7485311.

Chiriyath, Paul, and Bliss. Joint radar-communications information bounds with clutter: The phase noise menace. In *2016 IEEE Radar Conference (RadarConf)*, pages 1–6. IEEE, 2016b.

Chiriyath, Paul, Jacyna, and Bliss. Inner bounds on performance of radar and communications co-existence. *IEEE Transactions on Signal Processing*, 64(2):464–474, 2016c. doi: 10.1109/TSP.2015.2483485.

Chiriyath, Paul, and Bliss. Radar-communications convergence: Coexistence, cooperation, and co-design. *IEEE Transactions on Cognitive Communications and Networking*, 3(1):1–12, 2017. doi: 10.1109/TCCN.2017.2666266.

Chiriyath, Ragi, Mittelmann, and Bliss. Novel radar waveform optimization for a cooperative radar-communications system. *IEEE Transactions on Aerospace and Electronic Systems*, 55(3):1160–1173, 2019. doi: 10.1109/TAES.2019.2908739.

Junil Choi, Vutha Va, Nuria Gonzalez-Prelcic, Robert Daniels, Chandra R Bhat, and Robert W Heath. Millimeter-wave vehicular communication to support massive automotive sensing. *IEEE Communications Magazine*, 54(12):160–167, 2016.

Cohen, Tsiper, and Eldar. Analog-to-digital cognitive radio: Sampling, detection, and hardware. *IEEE Signal Processing Magazine*, 35(1):137–166, 2018.

Cover and Thomas. *Elements of Information Theory.* 2nd ed. Wiley, 2006.

Nicolo Decarli, Francesco Guidi, and Davide Dardari. A novel joint rfid and radar sensor network for passive localization: Design and performance bounds. *IEEE Journal of Selected Topics in Signal Processing*, 8(1):80–95, 2013.

Feng Ding and Tongwen Chen. Hierarchical identification of lifted state-space models for general dual-rate systems. *IEEE Transactions on Circuits and Systems I: Regular Papers*, 52(6):1179–1187, 2005.

Feng Ding, Peter X Liu, and Jie Ding. Iterative solutions of the generalized sylvester matrix equations by using the hierarchical identification principle. *Applied Mathematics and Computation*, 197(1):41–50, 2008.

Hany Elgala, Raed Mesleh, and Harald Haas. Indoor optical wireless communication: potential and state-of-the-art. *IEEE Communications Magazine*, 49(9):56–62, 2011.

John Ellen Zhuang. Spatial branch and bound method. URL `https://optimization.mccormick.northwestern.edu/`.

Evans. Shared spectrum access for radar and communications (ssparc), darpa , press release.[online]. available:, 2016a. URL `http://www.darpa.mil/program/shared-spectrum-access-for-radar-and-communications`.

Evans. Shared spectrum access for radar and communications (ssparc). *DARPA, Press Release.[Online]. Available: http://www. darpa. mil/program/shared-spectrum-access-for-radar-and-communications*, 2016b.

Ivan Farris, Antonio Iera, Leonardo Militano, and Silverio C Spinella. Performance evaluation of rfid tag-based "virtual" communication channels. In *2014 IEEE International Conference on Communications (ICC)*, pages 2897–2902. IEEE, 2014.

Giancarlo Fortino and Mukaddim Pathan. Integration of cloud computing and body sensor networks, 2014.

Gallager. *Information Theory and Reliable Communication*. 2nd ed. Wiley, 1968.

Mark A Govoni. Enhancing spectrum coexistence using radar waveform diversity. In *2016 IEEE Radar Conference (RadarConf)*, pages 1–5. IEEE, 2016.

Hugh Griffiths, Lawrence Cohen, Simon Watts, Eric Mokole, Chris Baker, Mike Wicks, and Shannon Blunt. Radar spectrum engineering and management: Technical and regulatory issues. *Proceedings of the IEEE*, 103(1):85–102, 2015. doi: 10.1109/JPROC.2014.2365517.

Changzhan Gu, Zhengyu Peng, and Changzhi Li. High-precision motion detection using low-complexity doppler radar with digital post-distortion technique. *IEEE*

Transactions on Microwave Theory and Techniques, 64(3):961–971, 2016. doi: 10.1109/TMTT.2016.2519881.

Srinath Gunnery, Pardhasaradhi Bethi, Prashantha H Kumar, and Srihari Pathipati. Target estimation performance improvement in cooperative radar and communication system spectrum sharing. In *2021 12th International Conference on Computing Communication and Networking Technologies (ICCCNT)*, pages 1–6, 2021. doi: 10.1109/ICCCNT51525.2021.9580023.

Mitsuhiro Hakozaki and Hiroyuki Shinoda. Digital tactile sensing elements communicating through conductive skin layers. In *Proceedings 2002 IEEE International Conference on Robotics and Automation (Cat. No. 02CH37292)*, volume 4, pages 3813–3817. IEEE, 2002.

Hassanien, Amin, Zhang, and Himed. A dual-function mimo radar-communications system using PSK modulation. In *2016 24th European Signal Processing Conference (EUSIPCO)*, pages 1613–1617, 2016. doi: 10.1109/EUSIPCO.2016.7760521.

Helstrom. *Statistical Theory of Signal Detection*. 2nd ed. 1966.

Farzad Hessar and Sumit Roy. Spectrum sharing between a surveillance radar and secondary wi-fi networks. *IEEE Transactions on Aerospace and Electronic Systems*, 52(3):1434–1448, 2016.

Qianyi Huang, Huangxun Chen, and Qian Zhang. Joint design of sensing and communication systems for smart homes. *IEEE Network*, 34(6):191–197, 2020.

Yongwei Huang, Marco Piezzo, Vincenzo Carotenuto, and Antonio De Maio. Radar waveform design under similarity, bandwidth priority, and spectral coexistence constraints. In *2017 IEEE Radar Conference (RadarConf)*, pages 1142–1147. IEEE, 2017.

Jiang, Harishan, Tharmarasa, Kirubarajan, and Thayaparan. Integrated track initialization and maintenance in heavy clutter using probabilistic data association. *Signal Processing*, 94:241–250, 2014. ISSN 0165-1684. doi: https://doi.org/10.1016/j.sigpro.2013.06.026. URL `https://www.sciencedirect.com/science/article/pii/S0165168413002442`.

Kay. *Fundamentals of statistical signal processing: Estimation Theory.* 1st ed. Prentice-Hall, 1993.

John B Kenney. Dedicated short-range communications (dsrc) standards in the united states. *Proceedings of the IEEE*, 99(7):1162–1182, 2011.

Kershaw and Evans. Optimal waveform selection for tracking systems. *IEEE Transactions on Information Theory*, 40(5):1536–1550, 1994. doi: 10.1109/18.333866.

Kershaw and Evans. Waveform selective probabilistic data association. *IEEE Transactions on Aerospace and Electronic Systems*, 33(4):1180–1188, 1997. doi: 10.1109/7.625110.

Khawar, Abdel-Hadi, and Clancy. MIMO radar waveform design for coexistence with cellular systems. In *2014 IEEE International Symposium on Dynamic Spectrum Access Networks (DYSPAN)*, pages 20–26. IEEE, 2014.

Khawar, Abdelhadi, and Clancy. Target detection performance of spectrum sharing MIMO radars. *IEEE Sensors Journal*, 15(9):4928–4940, 2015a.

Khawar, Abdelhadi, and Clancy. Coexistence analysis between radar and cellular system in LoS channel. *IEEE Antennas and Wireless Propagation Letters*, 15: 972–975, 2015b.

M Lang, G McCarty, B Wilen, and J Awl. Light detection and ranging: New information for improved wetland mapping and monitoring. *National Wetlands Newsletter*, 32(5):10–13, 2010.

Klaus-Dieter Langer and Jelena Grubor. Recent developments in optical wireless communications using infrared and visible light. In *2007 9th International Conference on Transparent Optical Networks*, volume 3, pages 146–151. IEEE, 2007.

Nadav Levanon. Creating sidelobe-free range zone around detected radar target. In *2014 IEEE 28th Convention of Electrical Electronics Engineers in Israel (IEEEI)*, pages 1–5, 2014. doi: 10.1109/EEEI.2014.7005837.

Li and Petropulu. Joint transmit designs for coexistence of MIMO wireless communications and sparse sensing radars in clutter. *IEEE Transactions on Aerospace and Electronic Systems*, 53(6):2846–2864, 2017.

Liberti, Leo. Introduction to global optimization. URL `https://www.lix.polytechnique.fr/~liberti/teaching/globalopt-lima.pdf/`. Accessed Feb. 15, 2008.

Fan Liu, Christos Masouros, Athina P. Petropulu, Hugh Griffiths, and Lajos Hanzo. Joint radar and communication design: Applications, state-of-the-art, and the road ahead. *IEEE Transactions on Communications*, 68(6):3834–3862, 2020. doi: 10.1109/TCOMM.2020.2973976.

Dingyou Ma, Nir Shlezinger, Tianyao Huang, Yimin Liu, and Yonina C Eldar. Joint radar-communication strategies for autonomous vehicles: Combining two key automotive technologies. *IEEE signal processing magazine*, 37(4):85–97, 2020.

Mahal, Khawar, Abdelhadi, and Clancy. Spectral coexistence of MIMO radar and MIMO cellular system. *IEEE Transactions on Aerospace and Electronic Systems*, 53(2):655–668, 2017. doi: 10.1109/TAES.2017.2651698.

Ashoka Chakravarthi Mahipathi, Srinath Gunnery, Srihari Pathipati, John D'Souza, and Paramananda Jena. Nonlinear frequency modulated waveform optimization for a cooperative radar-communication system. In *2021 IEEE International Conference on Electronics, Computing and Communication Technologies (CONECCT)*, pages 1–6, 2021. doi: 10.1109/CONECCT52877.2021.9622544.

Ashoka Chakravarthi Mahipathi, Srinath Gunnery, Pathipati Srihari, John D'Souza, and Paramananda Jena. Constrained radar waveform optimization for a cooperative radar-communication system. *Physical Communication*, pages 1–18, 2023.

Mishali and Eldar. From theory to practice: Sub-nyquist sampling of sparse wideband analog signals. *IEEE Journal of Selected Topics in Signal Processing*, 4(2):375–391, 2010.

Musicki and Song. Track initialization: Prior target velocity and acceleration moments. *IEEE Transactions on Aerospace and Electronic Systems*, 49(1):665–670, 2013. doi: 10.1109/TAES.2013.6404131.

Patton, Rigling, and Brian. Autocorrelation constraints in radar waveform optimization for detection. *IEEE Transactions on Aerospace and Electronic Systems*, 48(2): 951–968, 2012. doi: 10.1109/TAES.2012.6178041.

Paul, Chiriyath, and Bliss. Survey of rf communications and sensing convergence research. *IEEE Access*, 5:252–270, 2016.

Bryan Paul, Alex R. Chiriyath, and Daniel W. Bliss. Joint communications and radar performance bounds under continuous waveform optimization: The waveform awakens. In *2016 IEEE Radar Conference (RadarConf)*, pages 1–6, 2016. doi: 10.1109/RADAR.2016.7485103.

Carlos Pozo, Gonzalo Guillen-Gosaalbez, Albert Sorribas, and Laureano Jimenez. A spatial branch-and-bound framework for the global optimization of kinetic models of metabolic networks. *Industrial and Engineering Chemistry Research*, 50(9):5225–5238, 2011.

Junhui Qian, Marco Lops, Le Zheng, Xiaodong Wang, and Zishu He. Joint system design for the coexistence of MIMO radar and MIMO communication. *IEEE Transactions on Signal Processing*, 66(13):3504–3519, 2018.

Vasanthan Raghavan, Tao Luo, Ozge H. Koymen, and Junyi Li. Antenna selection for upper MILLIMETER wave and THz bands. In *2020 54th Asilomar Conference on Signals, Systems, and Computers*, pages 450–454, 2020. doi: 10.1109/IEEECONF51394.2020.9443286.

Rago, Willett, and Bar-Shalom. Detection-tracking performance with combined waveforms. *IEEE Transactions on Aerospace and Electronic Systems*, 34(2):612–624, 1998. doi: 10.1109/7.670395.

Theodore S Rappaport, James N Murdock, and Felix Gutierrez. State of the art in 60-GHz integrated circuits and systems for wireless communications. *Proceedings of the IEEE*, 99(8):1390–1436, 2011.

Yuwei Ren, Jiuyuan Lu, Andrian Beletchi, Yin Huang, Ilia Karmanov, Daniel Fontijne, Chirag Patel, and Hao Xu. Hand gesture recognition using 802.11 ad mmwave sensor in the mobile device. In *2021 IEEE Wireless Communications and Networking Conference Workshops (WCNCW)*, pages 1–6. IEEE, 2021.

Richards, Sheer, and Raleigh. *Principles of Modern Radar: Basic Principles*. 1st ed. SciTech Publishing, 2010. ISBN 978-93-80381-29-9.

Richmond. Mean-squared error and threshold snr prediction of maximum-likelihood signal parameter estimation with estimated colored noise covariances. *IEEE Transactions on Information Theory*, 52(5):2146–2164, 2006. doi: 10.1109/TIT.2006.872975.

Saruthirathanaworakun, Peha, and Correia. Opportunistic sharing between rotating radar and cellular. *IEEE Journal on Selected Areas in Communications*, 30(10): 1900–1910, 2012.

Gnane Swarnadh Satapathi and Srihari Pathipati. Waveform agile sensing approach for tracking benchmark in the presence of ECM using IMMPDAF. *Radioengineering*, 26(1):227, 2017.

Rob Schneiderman. Unmanned drones are flying high in the military/aerospace sector [special reports]. *IEEE Signal Processing Magazine*, 29(1):8–11, 2011.

Rohit Singh, Deepak Saluja, and Suman Kumar. R-comm: A traffic based approach for joint vehicular radar-communication. *IEEE Transactions on Intelligent Vehicles*, pages 1–1, 2021. doi: 10.1109/TIV.2021.3074389.

Sinha, Ding, Kirubarajan, and Farooq. Track quality based multitarget tracking approach for global nearest-neighbour association. *IEEE Transactions on Aerospace and Electronic Systems*, 48(2):1179–1191, 2012. doi: 10.1109/TAES.2012.6178056.

Sira, Morrell, and Papandreou. Waveform design and scheduling for agile sensors for target tracking. In *Conference Record of the Thirty-Eighth Asilomar Conference on Signals, Systems and Computers, 2004.*, volume 1, pages 820–824 Vol.1, 2004. doi: 10.1109/ACSSC.2004.1399251.

Sira, Papandreou, and Morrell. Dynamic configuration of time-varying waveforms for agile sensing and tracking in clutter. *IEEE Transactions on Signal Processing*, 55 (7):3207–3217, 2007. doi: 10.1109/TSP.2007.894418.

Sira, Papandreou, and Morrell. Advances in waveform-agile sensing for tracking. *Synthesis Lectures on Algorithms and Software in Engineering*, 1(1):1–83, 2008. doi: 10.2200/S00168ED1V01Y200812ASE002. URL `https://doi.org/10.2200/S00168ED1V01Y200812ASE002`.

Sira, Li, Papandreou, Morrell, Cochran, and Rangaswamy. Waveform-agile sensing for tracking. *IEEE Signal Processing Magazine*, 26(1):53–64, 2009. doi: 10.1109/MSP.2008.930418.

Sodagari, Khawar, Clancy, and McGwier. A projection based approach for radar and telecommunication systems coexistence. In *2012 IEEE Global Communications Conference (GLOBECOM)*, pages 5010–5014, 2012.

Gunnery Srinath, Bethi Pardhasaradhi, Prashantha Kumar H., and Pathipati Srihari. Tracking of radar targets with in-band wireless communication interference in radcomm spectrum sharing. *IEEE Access*, 10:31955–31969, 2022. doi: 10.1109/ACCESS.2022.3159623.

Stein, Oliver, Peter Kirst, and Paul Steuermann. An enhanced spatial branch-and-bound method in globaloptimization with nonconvex constraints. URL `http://www.optimization-online.org/DB_FILE/2013/04/3810.pdf/`. Accessed 2013.

Christian Sturm and Werner Wiesbeck. Waveform design and signal processing aspects for fusion of wireless communications and radar sensing. *Proceedings of the IEEE*, 99(7):1236–1259, 2011. doi: 10.1109/JPROC.2011.2131110.

Bo Tang, Jun Liu, Hai Wang, and Yihua Hu. Constrained radar waveform design for range profiling. *IEEE Transactions on Signal Processing*, 69:1924–1937, 2021. doi: 10.1109/TSP.2021.3065830.

Tichavsky, Muravchik, and Nehorai. Posterior cramer-rao bounds for discrete-time nonlinear filtering. *IEEE Transactions on Signal Processing*, 46(5):1386–1396, 1998. doi: 10.1109/78.668800.

Van Trees. *Detection, Estimation and Modulation Theory, PartIII*. Wiley, 1971. ISBN 0-471-10793-X.

Sadayuki Tsugawa and Shin Kato. Energy its: another application of vehicular communications. *IEEE Communications Magazine*, 48(11):120–126, 2010.

Panchapakesan Venkataraman. *Applied optimization with MATLAB programming*. John Wiley & Sons, 2009.

Aloysius Wehr and Uwe Lohr. Airborne laser scanning—an introduction and overview. *ISPRS Journal of photogrammetry and remote sensing*, 54(2-3):68–82, 1999.

Jingrui Xie, Tao Hong, Thomas Laing, and Chongqing Kang. On normality assumption in residual simulation for probabilistic load forecasting. *IEEE Transactions on Smart Grid*, 8(3):1046–1053, 2017. doi: 10.1109/TSG.2015.2447007.

Chih-Chuan Yen, Alfonso E Gutierrez, Dharmaraj Veeramani, and Daniel Van Der Weide. Radar cross-section analysis of backscattering RFID tags. *IEEE Antennas and Wireless Propagation Letters*, 6:279–281, 2007.

Andrew Zhang, Md Lushanur Rahman, Xiaojing Huang, Yingjie Jay Guo, Shanzhi Chen, and Robert W Heath. Perceptive mobile networks: Cellular networks with radio vision via joint communication and radar sensing. *IEEE Vehicular Technology Magazine*, 16(2):20–30, 2020.

Le Zheng, Marco Lops, Yonina C. Eldar, and Xiaodong Wang. Radar and communication coexistence: An overview: A review of recent methods. *IEEE Signal Processing Magazine*, 36(5):85–99, 2019. doi: 10.1109/MSP.2019.2907329.

Wenxing Zhou, Ruoyu Zhang, Guangyi Chen, and Wen Wu. Integrated sensing and communication waveform design: A survey. *IEEE Open Journal of the Communications Society*, 3:1930–1949, 2022. doi: 10.1109/OJCOMS.2022.3215683.

List of Publications

Journal Publications

1. Ashoka Chakravarthi Mahipathi, Srinath Gunnery, Pathipati Srihari, John D'Souza, and Paramananda Jena. "**Constrained radar waveform optimization for a cooperative radar-communication system.**" Physical Communication, Volume 57, 2023, 101984, ISSN 1874-4907, https://doi.org/10.1016/j.phycom.2022.101984.

2. A. C. Mahipathi, B. P. Saradhi, S. Gunnery, P. Srihari, J. D'souza and P. Jena. "**Optimum Waveform Selection for Target State Estimation in the Joint Radar-Communication System.**" IEEE Open Journal of Signal Processing, Volume 5, pp. 459-477, 2024, doi: 10.1109/OJSP.2024.3359997.

3. Ashoka Chakravarthi Mahipathi, Bethi Pardhasaradhi, Pathipati Srihari, John D'Souza, Paramananda Jena, Jing Zhou, and Lingareddy Cenkeramaddi. "**Communication-aided Target State Estimation in a Cooperative Radar-Communication System.**" IEEE Sensors Journal (Under review).

4. Ashoka Chakravarthi Mahipathi, Bethi Pardhasaradhi, Purushottama T L, Pathipati Srihari, John D'Souza, and Lingareddy Cenkeramaddi. "**A Survey on Waveform Design for Radar-Communication Convergence.**" IEEE Access Journal (Under review).

Conference Publications

1. A. C. Mahipathi, S. Gunnery, S. Pathipati, J. D'Souza and P. Jena, "**Nonlinear Frequency Modulated Waveform Optimization for a Cooperative Radar-Communication System.**" 2021 IEEE International Conference on Electronics, Computing and Communication Technologies (CONECCT), Bangalore, India, 2021, pp. 1-6, doi: 10.1109/CONECCT52877.2021.9622544.

2. A. C. Mahipathi, B. Pardhasaradhi, S. Pathipati, J. D'Souza and P. Jena, "**LPI-Based NLFM Radar Waveform Design for a Cooperative Radar-Communication System.**" 2023 IEEE International Conference on Electronics, Computing and Communication Technologies (CONECCT), Bangalore, India, 2023, pp. 1-5, doi: 10.1109/CONECCT57959.2023.10234785.